NICOLAUS COPERNICUS ASTRONOMICAL CENTER
POLISH ACADEMY OF SCIENCES

Constraining the geometry of the accretion flow in black hole X-ray binaries

Marta Aleksandra Dziełak

Ph.D thesis

Supervisors: Dr. Barbara De Marco and Prof. Andrzej Zdziarski

Warsaw, September 2021

ABSTRACT

The project has focused on constraining the geometry of the accretion flow in the hard state of black hole X-ray binaries using both standard spectral and combined spectral-timing techniques. I performed spectral modelling of X-ray spectra to constrain the parameters of the reflection of hard X-ray photons from the cold accretion disc. I also used spectral-timing analysis techniques to describe the spatial structure of the accretion flow, by studying the *rms* (root-mean-square) variability spectra – namely, the energy spectra of the different variability components. The variability power of these components peaks at different time scales, therefore they are likely related to different distances from the accreting object. I used both these approaches to investigate the geometry (e.g. the position of the inner edge of the cold accretion disc) and spectral stratification of the inner accretion flow (e.g. the inhomogeneities of the Comptonization zone).

In my work on GX 339-4, I tested different models of reflection and I found that the inferred physical quantities (e.g. disc truncation, iron abundance) strongly depend on the reflection model used and assumptions made. Analysing another source - MAXI J1820+070 - also using reflection fitting, we found that there are two statistically similar results: one corresponding to an untruncated disc, but having non-realistic inclination, and another where the disc is truncated and the inclination is in agreement with that of the binary system and of the jet. This shows the need for using different techniques to break model degeneracies. In addition, the spectral analysis of MAXI J1820+070 revealed the possible presence of a spectrally stratified Comptonization region, which emission is reflected by two different zones of the cold disc in the hard state. Therefore, I used spectral-timing techniques to test a scenario of a spectrally stratified inner Comptonization zone, surrounded by a truncated cold accretion disc in MAXI J1820+070. This study showed that different variability components (likely originating at different distances from the black hole) have very different energy spectra. I found that these spectra can be modelled self-consistently, as combined emission from an outer Comptonization region fueled by the photons from the cold disc, and an inner Comptonization region fueled by the photons from the outer Comptonization region.

The main result of my project is that the hot flow responsible for the primary X-ray

emission in the hard state of BH X-ray binaries is consistent with being a spectrally stratified medium rather than a point-like compact source. Physically, this is likely due to a dependence of the optical depth and/or temperature of seed photons on the radial distance from the BH. The hot flow fills the inner regions of a cold accretion disc truncated at tens of gravitational radii away from the BH in the hard state.

STRESZCZENIE

Praca skupia się na badaniu małomasywnych rentgenowskich układów podwójnych zawierających czarną dziurę, a w szczególności geometrii przepływu akrecyjnego w stanie twardym, przy użyciu analizy widmowej i widmowo-czasowej. Wykonałam modelowanie widm rentgenowskich w celu określenia parametrów odbicia twardego promieniowania rentgenowskiego od chłodnego dysku akrecyjnego. Użyłam również technik widmowo-czasowych aby opisać przestrzenną strukturę przepływu akrecyjnego (korzystając z *rms* - root-mean-square - widm zmienności, które ukazują widma różnych składowych zmienności. Składowe zmienności widoczne w widmach mocy, które mają maksimum na różnych skalach czasowych, są najprawdopodobniej powiązane z różnymi odległościami od akreującego obiektu. Użyłam obu tych podejść aby określić geometrię (np. położenie wewnętrznej krawędzi chłodnego dysku akrecyjnego) oraz widmową niejednorodność wewnętrznego przepływu akrecyjnego (np. niejednorodności obszaru Comptonizacji).

W mojej pracy nad źródłem GX 339-4 porównywałam modele odbicia twardego promieniowania rentgenowskiego. Znalazłam zależność otrzymanych parametrów fizycznych (np. wewnętrznego promienia dysku, zawartości żelaza) od zastosowanych modeli (kodów i założeń). Następnie w analizie innego źródła - MAXI J1820+070 - również przy dopasowywaniu modeli odbicia, znaleźliśmy dwa bardzo podobne statystycznie wyniki: jeden odpowiadający nieodciętemu dyskowi, ale przy nierealistycznej inklinacji, oraz drugi w którym dysk jest odcięty, a inklinacja jest zgodna z nachyleniem orbity układu i dżetu. Te wyniki wskazują na konieczność użycia innych metod do rozstrzygnięcia pomiędzy badanymi scenariuszami. W pracy nad MAXI J1820+070 zauważyliśmy również, że do opisu badanego obiektu potrzebna jest widmowa niejednorodność obszaru Comptonizacji oraz obecność dwóch regionów dysku odbijających twarde fotony. Do dalszego badania niejednorodności obszaru Comptonizacji, zastosowałam technikę widmowo-czasową. Te badania pokazały, że różne składowe zmienności (czyli prawdopodobnie pochodzące z obszarów umiejscowionych na różnych dystansach od czarnej dziury) mają bardzo różne widma. Odkryłam, że ta sytuacja może być opisana w konsekwentny sposób przy użyciu zewnętrznej Comptonizacji zasilanej przez fotony z dysku, oraz wewnętrznej Comptonizacji, gdzie źródłem fotonów jest emisja zewnętrznego obszaru Comptoniza-

cji. Pokazuje to, że gorący przepływ akrecyjny jest niejednorodny pod względem głębokości optycznej i temperatury zasilających go fotonów.

Głównym wynikiem mojej pracy jest określenie, że gorący przepływ akrecyjny, który odpowiada za emisję twardych fotonów rentgenowskich, w stanie twardym rentgenowskich układów podwójnych, jest niejednorodnym widmowo, rozciągłym obszarem. Fizycznie, pokazuje to zależność głębokości optycznej i/lub temperatury zasilających to medium fotonów od odległości od czarnej dziury. W stanie twardym rentgenowskich układów podwójnych, gorący przepływ wypełnia wewnętrzną część, a chłodny dysk akrecyjny jest odcięty na dziesiątkach promieni grawitacyjnych.

Contents

Chapter 1

Overview

This thesis contains a brief overview of the topic and three published articles:

I. Comparison of spectral models for disc truncation in the hard state of GX 339-4, Dziełak, M. A.; Zdziarski, A. A.; Szanecki, M.; De Marco, B.; Niedźwiecki, A.; Markowitz A.; 2019, MNRAS, 485, 3845; **[1]**
In this work on GX 339-4 in the bright hard state, I tested different models of reflection (codes and assumptions) and I found the dependence of the results (e.g. disc truncation, iron abundance) on them. This shows the need of using different techniques to distinguish between the models. Still, all of the fitted models prefer the inner edge of the disc to be much larger than R_{ISCO} at their best-fit values.

II. Accretion Geometry in the Hard State of the Black-Hole X-Ray Binary MAXI J1820+070, Zdziarski, A. A.; Dziełak, M. A.; De Marco, B.; Szanecki, M.; Niedźwiecki, A.; 2021, ApJL, 909, L9; **[2]**
Analysing MAXI J1820+070 in the hard state using reflection fitting, we found that there are two statistically similar results: one corresponding to an untruncated disc, but having non-realistic inclination, and another where the disc is truncated and inclination is in agreement with that of the binary system. We concluded that the latter is preferable. This work also showed the presence of a spectrally stratified Comptonization region, which emission is reflected by two different zones of the cold disc.

III. A spectrally stratified hot accretion flow in the hard state of MAXI J1820+070, Dziełak, M. A.; De Marco, B.; Zdziarski, A. A.; 2021, MNRAS, 506, 2020; **[3]**
I tested the radial dependence of the spectral structure of MAXI J1820+070 in the hard state using spectral-timing techniques. The main result of this work is that different variability components (likely originating at the different distances from the black hole) have very different energy spectra. I modelled this in a self-consistent way with an outer Comptonization region fueled by photons from the cold disc, and an inner Comptonization region fueled by the photons from the outer Comptonization region. According to this finding, the hot flow is stratified in the optical depth and temperature of seed photons.

Chapter 2

Introduction

2.1 Black holes

Black holes (BHs) are some of the most intriguing astrophysical objects known. Their existence was proved in the second half of the 20th century, but the mathematical idea behind this kind of objects was proposed earlier. The existence of these exotic objects was first hypothesized by John Michell in 1783, who referred to a black hole as "dark star" [4]. In 1916 Karl Schwarzschild solved Einstein's equation for a non-rotating star and found the existence of a limit radius at which the velocity needed to escape the gravitational pull of the BH equals the speed of light.

The first observation of BH candidates (Cyg X-1 and Sagittarius A*) was done with X-ray instruments performing Aerobee surveys in 1964 [5]. Since this discovery, both these objects were confirmed to be BHs based on the estimates of their masses [6, 7]. The most recent studies used a global very long baseline interferometry array to image the shadow of a BH (caused by gravitational light bending and photon capture at the event horizon), successfully achieving event-horizon-scale images of the BH in the centre M87 galaxy [8].

To fully describe a BH we need to know its mass (M), angular momentum and electric charge. Astrophysical BHs are expected to be electrically neutral, so that they can be described by only two parameters.

There is no way to investigate the interior of a BH, therefore all studies have to stop at the, so-called, event horizon. For a non-rotating BH (called also Schwarzschild

BH) the event horizon is located at $R = 2GM/c^2$ (where G is the gravitational constant and c is the speed of light), also called the Schwarzschild radius. In general, the event horizon is located at $R_h = 1 + \sqrt{1 - a^2}$, where R_h is expressed in units of gravitational radii ($R_g = GM/c^2$), and a is the spin parameter, which spans values ranging from 0 for a non-rotating BH to almost 1 for a maximally spinning BH [9].

General relativity tells us that in addition to the event horizon, there is another important radius below which stable circular orbits can not exist. This radius marks the innermost stable circular orbit (R_{ISCO}) and depends on the BH spin ($R_{ISCO} = 1.23\ R_g$ for maximum spin, $R_{ISCO} = 6\ R_g$ for Schwarzschild BH, and $R_{ISCO} = 9\ R_g$ for maximum retrograde spin - i.e. opposite to the BH spin).

Some of the most energetic phenomena in the Universe are caused by the process of matter falling (accreting) onto a BH. This process can release up to 30% of the matter's rest mass energy (mc^2), greatly exceeding energies that can be achieved in any thermonuclear reaction or the most efficient chemical reactions [10].

Among the main types of astrophysical sources containing a BH are active galactic nuclei (with a BH of $10^6 - 10^9 M_\odot$) and BH X-ray binaries (with a BH of $\sim 10 M_\odot$). These sources show many flavours of accretion, which can be broadly classified into different accretion states (Sect. 2.4). Understanding BH accretion is among the major goals of modern astrophysics, and holds the key to unveiling the link among the different physical components observed to exist in the close vicinity of a BH (such as the accretion disc, the hot inner plasma, winds, and jets).

2.1.1 X-ray binaries

X-ray binaries are often bright sources of X-ray emission. They contain a compact object (accretor; BH or neutron star) that is accreting matter from a companion star (donor). Depending on the mass of the donor we can define two types of sources: low and high mass X-ray binaries. Usually, the former present outbursts of activity (Fig. 2.5, see Sect. 2.4), while the latter are persistent sources of X-ray photons. In low mass X-ray binaries, the donor fills its Roche lobe and a transfer of matter happens through the Lagrangian point (L1). In high mass X-ray binaries, the stellar wind from the donor represents the main channel of accretion. The gravitational energy of the accreting matter is radiated away, producing copious X-ray emission. This

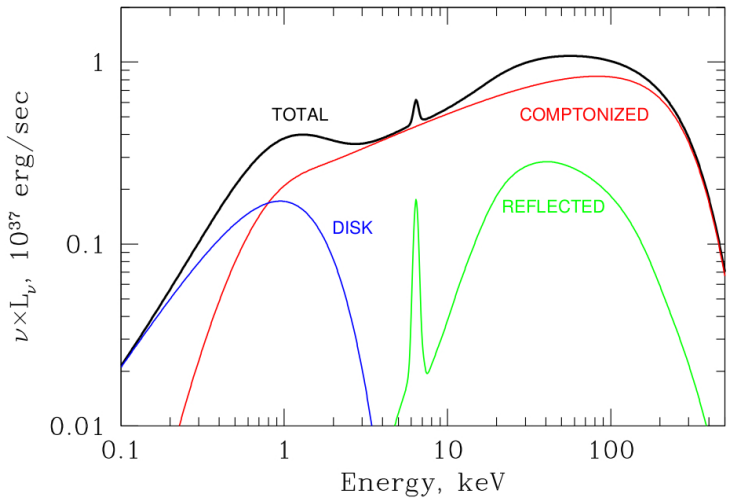

Figure 2.1: The typical X-ray spectrum of a BH X-ray binary, showing the main spectral components. The disc blackbody (Sect. 2.2.1) in blue, the Comptonization continuum (Sect. 2.2.2) in red and, the reflection component (Sect. 2.2.3) in green. [11]

emission provides information about the environment around the compact object and represents a powerful diagnostic of the behaviour of matter in the strong gravity field of the compact object.

In this thesis, I will focus on binary systems having a BH as an accretor (BH X-ray binaries). These systems present a complex phenomenology. In particular, the hard state (Sect. 2.4), characteristic of the first and last phases of an outburst, shows some of the most complex spectral and timing phenomenology. In this thesis I will be using a combination of spectral and timing techniques (Sect. 2.6) in order to investigate the physical conditions of the accreting gas in the hard state.

2.2 The X-ray spectrum of BH X-ray binaries

The energy spectrum shows the distribution of the emitted flux as a function of photon's energy. X-ray binaries can emit radiation over the entire electromagnetic spectrum (from radio to gamma-rays). In particular, the X-ray spectrum is produced in the closest regions to the BH, thus providing a powerful diagnostic to study BH accre-

tion. In the following sections I will describe in detail the main spectral components contributing to the X-ray spectrum.

2.2.1 Disc emission

The accreting matter has some angular momentum, therefore the infall onto the BH is not direct and an accretion disc is formed. In the standard accretion disc model [12] thermal emission is produce by an optically thick and geometrically thin disc that extends down to $R_{\rm ISCO}$. Matter orbiting the BH with Keplerian motion loses its angular momentum via viscosity (a process likely related to magneto-rotational instability [13]). The locally emitted energy of each ring of matter (at each radius) has a blackbody spectrum. Therefore the total disc emission can be described as a sum of blackbody components (with the different temperatures depending on the distance from the BH) - such a spectrum is usually referred to as a disc blackbody spectrum (Fig. 2.1 in blue) [14]. The disc blackbody spectrum peaks at the temperature that corresponds to the innermost parts of the optically thick disc. The observed value depends on the BH mass, spin and accretion rate and changes as a function of the accretion state (see Sect. 2.4), ranging between $kT_{\rm in} \lesssim 0.2$ keV at the beginning and at the end of the outburst, and $kT_{\rm in} \sim 1$ keV when the source reaches the highest luminosities.

2.2.2 Comptonization continuum

The X-ray spectrum extends up to very high energies. Disc emission ($\lesssim 1$ keV) alone can not explain this hard X-ray emission (~ 100 keV), thus another component is needed. This component is best described by inverse-Compton scattering. In this process, soft X-ray photons emitted from the cold disc are scattered in a hot, optically thin ($\tau \sim 1$ plasma), gaining energy in the process. Therefore, the existence of a hot plasma in the inner regions of the accretion flow was postulated in order to explain this hard X-ray spectral component. The population of hot electrons have a semi-relativistic distribution, which means that a fraction of these electrons (that appear to be predominantly thermal) move at velocities close to the speed of light ($T \sim 10^9 K$) [15, 16, 17]. Depending on the temperature of the electrons and if their distribution is thermal, the photons' energy can be amplified by a large factor, reaching the hard X-rays energy band and higher. The shape of the thermal Comptonization continuum

can be approximated - between the seed photon spectrum and the cutoff - by a power-law ($F(E) \sim E^{-\Gamma}$, where $E = h\nu/m_e c^2$, h is the Planck constant, ν is the frequency of the photons and m_e is the mass of the electron) and its slope (Γ) depends on the optical depth of the plasma and the temperature of the electrons (Fig. 2.1 in red). In this process the maximum energy that photons can reach is limited by the temperature of the electrons (the normalized electron temperature is $\Theta = kT_e/m_e c^2$, where k is the Boltzmann constant and T_e is the temperature of the electrons), forming a high energy cut-off in the power-law like spectrum (e.g. exponential $F(E) \sim E^{-\Gamma} e^{-E/3\Theta}$ or more correctly, a sharper cut-off, as calculated in self-consistent comptonization models [18]). The observation of a high energy tail (up to $\sim$ 1 MeV), on the other hand, can be explained in terms of a hybrid distribution (thermal - Maxwellian and non-thermal - when plasma is not in thermodynamic equilibrium) of electrons [19, 20, 21, 22].

2.2.3 Reflection

Some fraction of the high energy X-ray photons leaving the hot plasma is emitted back in the direction of the cold accretion disc. This fraction depends on the geometry of the gas, and can lead to substantial irradiation of the accretion disc. The photons that illuminate the cold disc can be photoelectrically absorbed or Compton back-scattered. This process produces a so-called "reflection" component [24, 25] which includes contribution from re-emission of the absorbed photons including fluorescence, and Compton scattering. The strongest emission line of the reflection spectrum is the Fe Kα line (at 6.7 keV for neutral medium, with increasing energy for higher ionization states). Another characteristic feature is the Compton hump peaking at $\sim$ 30 keV, with a cutoff between tens and a few hundreds of keV (Fig. 2.1 in green). The Compton hump is due to reflection but the presence of the lines is due to reprocessing that contributes at low energies including soft X-rays. The fluorescent Fe Kα line is created when a photon with energy >7.1 keV strips an electron from the iron's K shell. This is followed by the transition of an electron from the L-shell ($n = 2$) to the K-shell ($n = 1$), causing the emission of a quantum of energy. Hard X-ray irradiation of the cold disc can cause the production of other fluorescent lines as well, but the iron line is the most prominent due to the high iron abundance (compared to the other elements) and the relatively low probability of Auger de-excitation [26].

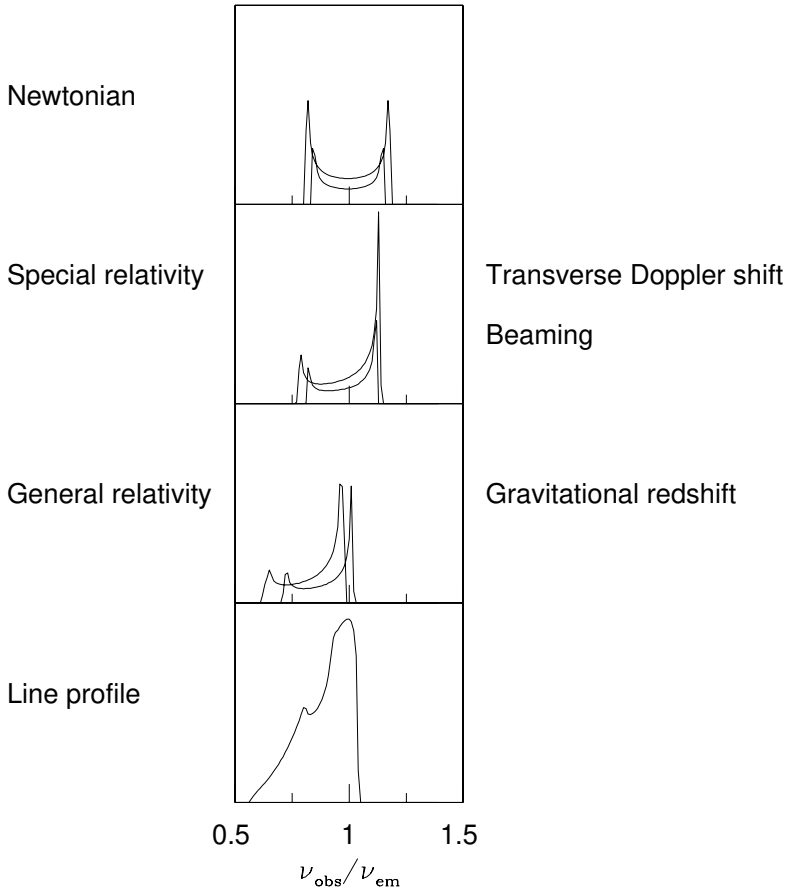

Figure 2.2: The expected distortions of the profile of the Fe Kα line as a consequence of different effects. From top to bottom: line emitted from a Keplerian disc; line modified by special relativity effects (transverse Doppler shift and beaming); line modified by general relativity effects (gravitational redshift); the final line profile, including all the above-mentioned effects. [23]

The shape of reflection features greatly depends on the physical properties (the distance from the BH, iron abundance, ionization state and inclination) of the cold accretion disc. For instance, the iron line is intrinsically narrow and its observed broadening is due to the motion and location of the matter producing it. The profile of the line emitted from the Keplerian disc is broadened by the Doppler effect resulting in a symmetrical double-horned shape. The relativistic effects as transverse Doppler shift and boosting (due to special relativity) and gravitational redshift and light bending (due to general relativity) [27] are important close to the BH. These effects modify

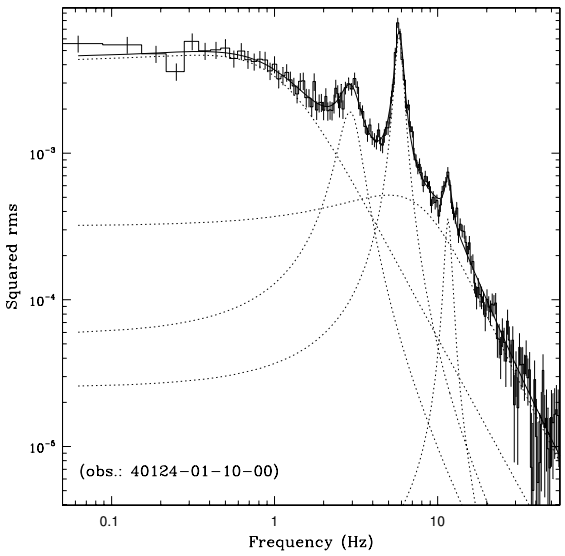

Figure 2.3: The PSD of BH X-ray binary in the hard state with broad-band continuum and type C QPOs. The solid line shows the best fit with five Lorentzians (dotted lines). [28]

the line profile and result in a redshifted, skewed and broadened line, with enhanced emission in the blue peak [23] - see Fig. 2.2.

2.3 X-ray spectral-timing properties

The emitted X-ray flux can show extreme variability on a wide range of time scales (from years to some fraction of a second). This variability can be used to extract information about the accretion process and the conditions of the accreting gas. In particular, the observed time scales are likely connected to characteristic time scales of the accretion flow (e.g. the viscous time scale [29]). These time scales depend on the properties of the disc, but also on the distance from the BH. Therefore, the study of this fast variability can be used to gain information about the spatial distribution of matter around a BH - additional to the information gained from disc properties that also depend on the distance from a BH. In the following I will describe some of the main tools used to study this variability, and the corresponding spectral-timing properties characterising BH X-ray binaries.

2.3.1 Power spectral density and frequency-resolved spectra

We can extract light curves ($x(t,E)$) in a given energy band, to monitor the flux variations as a function of time. Each light curve can be approximately described as a sum of Fourier components in the frequency domain ($X_j = \frac{1}{N}\sum_{N}^{k=1} x_k e^{i2\pi\nu_j/k}$, where N is the number of time bins and ν_j is the j-th Fourier frequency). This decomposition can be used to easily study the distribution of variability power as a function of Fourier frequency (i.e. the inverse of the time scale). To do so we extract the power spectral density (PSD, defined as $P_j = X_j X_j^*$).

The PSD of a BH X-ray binary can be quite complex, and is observed to change as a function of the accretion state. In general, it is phenomenologically described as a sum of Lorentzians. These Lorentzians are likely associated with different variability components, produced in different regions of the accretion flow, and thus peaking at different time scales [30, 31, 3]. Extracting the PSD in different energy bands, and integrating each Lorentzian over frequency we can reconstruct the energy spectra of the different variability components (so-called root-mean-square, *rms*, variability spectra), to infer the physical properties of the accretion flow as a function of the distance from the BH [32, 33, 3] (See more in Sect. 2.6).

The PSD of BH X-ray binaries is usually dominated by broad-frequency-band variability components (that can be described as broad Lorentzian components). However, during some accretion states, narrow features emerge on top of the broad-band noise (Fig. 2.3). These features are quasi-periodic oscillations (QPOs) produced in the innermost regions of the accretion flow [34]. Different types of QPOs have been identified based on their shape and intensity (type A, B, and C, [28, 35, 36, 37]). These different types are likely related to different production mechanisms [38, 39].

2.3.2 X-ray lags

The application of Fourier techniques also allows us to study correlations between light curves in different energy bands ($x(t)$ and $y(t)$), by measuring the cross-spectrum ($C_j = X_j Y_j^*$). The cross-spectrum describes the phase difference of the signals and can be translated into the time lags (delay between flux variations in the two energy bands).

Both types of lags are commonly observed in BH X-ray binaries. The hard lags

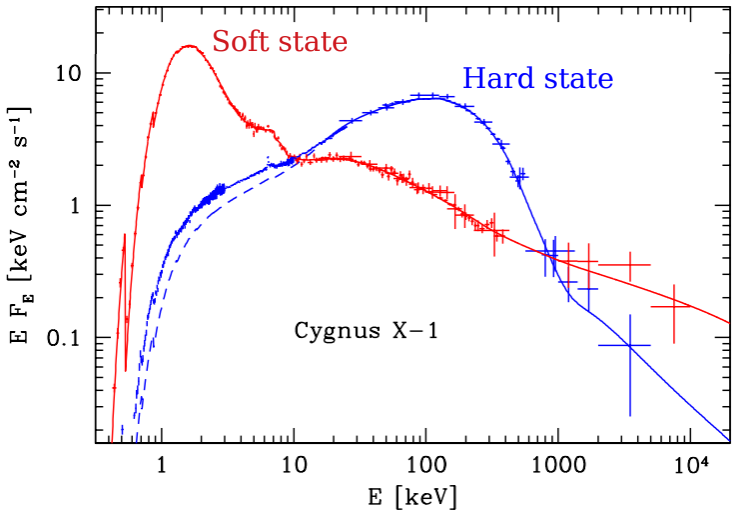

Figure 2.4: The soft (red) and hard (blue) state spectra of Cyg X-1. [47]

(when variable hard X-ray photons lag behind variable soft X-ray photons) and the soft lags (when variable soft X-ray photons lag behind variable hard X-ray photons). The currently most accepted paradigm to explain hard lags (which are observed over a broad range of frequencies, but get suppressed at high frequencies) is inward propagation of mass accretion rate fluctuations in the accretion flow [40, 41]. The soft X-ray lags (observed at high frequencies) are ascribed to thermal reverberation, namely thermal reprocessing of irradiating hard X-ray photons in the cold disc [42, 43]. Since the light crossing time between the hard X-ray source and the reprocessing region in the disc is thought to contribute the most to these delays, soft lags can be used to determine the distances between the hot plasma and the cold disc [44, 45, 46].

2.4 Accretion states

Transient low mass BH X-ray binaries display strong and complex X-ray activity [48]. They spend most of the time in a quiescent state when the matter from the companion is accumulating in the disc and the X-ray luminosity is very low ($L_x/L_{\rm Edd} < 10^{-5}$, where $L_{\rm Edd} = 1.26 \times 10^{38}(M/M_\odot)$erg s^{-1} is the Eddington luminosity, which is the maximum luminosity for a steady, spherical accretion flow [49, 50]). In this state the

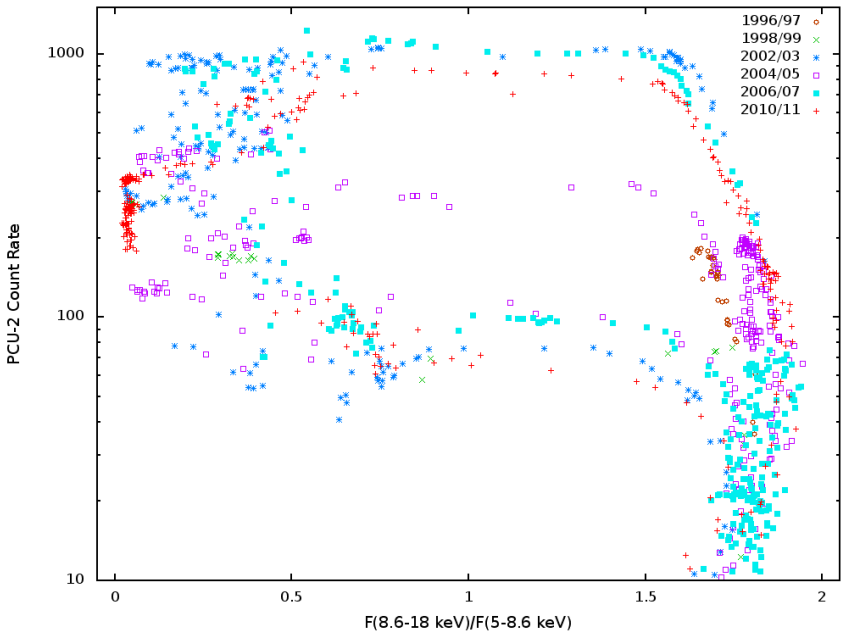

Figure 2.5: The hardness-intensity diagram of the X-ray binary GX 339-4's observations made by PCA on board of RXTE. The plot reports the spectral evolution of the source through 6 different outbursts identified by different symbols and colours. [1]

accretion disc is truncated at large radii [51, 52] and the distance between its inner edge and the BH continuously decreases [52, 53].

At some point, a critical temperature is reached, and an outburst of X-ray activity is triggered by hydrogen ionization disc instability [29]. During the outburst, the source undergoes substantial and continuous changes of its spectral and timing properties, likely as a consequence of the physical properties of the accretion flow changing quickly.

From the point of view of its spectral properties the source changes its X-ray brightness and X-ray spectral hardness (defined as the ratio between the high-energy flux, e.g. 4-10 keV, to the low-energy flux, e.g. 2-4 keV) - see Fig. 2.5. The evolution of hardness is due to the fact that the relative contribution of the different spectral components of the X-ray spectrum changes (see Sect. 2.2).

We can identify two main states: the hard state (Fig. 2.4 - in blue, Fig. 2.5 - hardness above ~ 1.5) and the soft state (Fig. 2.4 - in red, Fig. 2.5 - hardness below ~ 0.7). Fig. 2.4 presents a persistent high mass X-ray binary. These sources have similar hard and soft

states.

The X-ray spectrum in the hard state appears dominated by the thermal Comptonization component. The standard, cold accretion disc is visible, but much less prominent, with a peak at energies ~0.2-0.3 keV (e.g. a review by [29]). An additional high energy tail (ascribed to Comptonization by non-thermal electrons) is also observed in some sources.

The soft state spectrum differs significantly from the one observed in the hard state (Fig. 2.4). The main component is the standard cold accretion disc (peaking at ~ 1 keV). The Comptonization produced by non-thermal photons results in a high energy tail, and for some cases relativistically broadened reflection is observed.

Prominent spectral and timing changes characterize the transition between these two main states. In this phase several intermediate states have been identified and characterized by different combinations of thermal and Comptonization components.

From the point of view of the X-ray variability properties, similar evolutionary patterns have been recognized. In particular, the hard state is characterized by strong variability (with fractional *rms* ~ 20 - 40%), likely due to perturbations arising in the accretion flow. On the other hand the soft state is characterized by very low levels of X-ray variability, suggesting the presence of a more stable accretion flow (the fractional *rms* ~ 1 - 5%) [35, 28, 36, 37]. During the hard state and at the transition to the soft state, type C QPOs are observed. Their frequency is observed to increase with increasing brightness and decreasing hardness [34]. Type B QPOs are seen to quickly appear and disappear right at the transition to the soft state, and the rarely observed type A QPOs appear in the soft state [54, 55, 56].

2.5 Constraining the geometry of the inner accretion flow

The spectral-timing properties (Sect. 2.4) observed during an outburst of X-ray activity are thought to be associated with changes in the geometry of the accretion flow [58, 59].

A standard accretion disc reaching down to $R_{\rm ISCO}$ can successfully explain the soft state of BH X-ray binaries. However, as explained in Sect 2.4, this model cannot describe the hard state. Nonetheless, the geometry of the inner accretion disc and of the X-ray source in the hard state is highly debated.

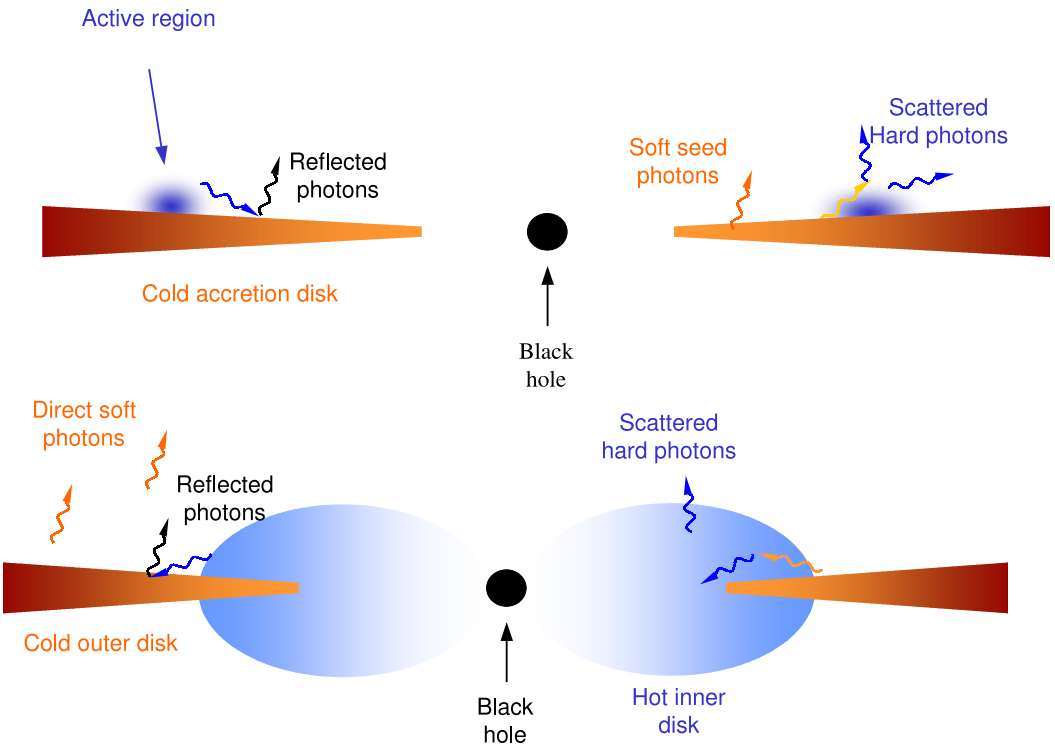

Figure 2.6: Cartoons presenting proposed geometries of the inner accretion flow for the soft (top) and hard (bottom) states [57]

Several studies have been yielding contradictory results (Fig. 2.7). One of the most used techniques in these studies is the fit of the X-ray spectrum with state-of-the-art reflection models. Some authors reported the presence of a cold disc reaching the immediate vicinity of the $R_{\rm ISCO}$ already at relatively low luminosities in the hard state. Other groups, using the same technique, presented results supporting the presence of a cold disc truncated at large radii (a few tens of $R_{\rm g}$) even in the bright hard state ([61], and references therein). The discrepancies between these two kinds of solutions have been explained by invoking, e.g. the presence of instrumental artifacts (such as pile up), or the limitations/assumptions of the models [1]. The controversy is still not solved, but most of the studies agree on the presence of a general trend of decreasing inner disc truncation radius as the source softens. Nonetheless, the reported values for the inner radius differ by up to two orders of magnitude (Fig. 2.7).

One of the geometries used to explain observed hard state energy spectra is the

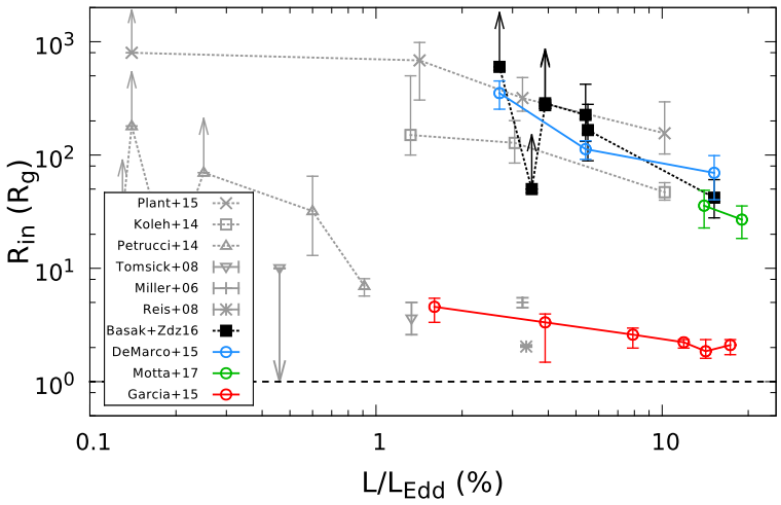

Figure 2.7: Determinations for the inner radius of the cold accretion disc in the hard state of GX 339–4 using reflection spectroscopy, but also including the reverberation estimates by [44]. [60]

lamppost [62]. In this geometry the Comptonization medium is located on the axis of BH rotation and approximated as a point-like source (so-called lamppost) - Fig. 2.8. Physically, this hard X-ray emitting region might be somehow connected to the jet. This scenario was proposed in order to allow for a substantial simplification of computations. Nonetheless, it is broadly used to describe the data, sometimes with modifications aimed at approximating more complex physical configurations (such as two lampposts at different heights above the horizon in order to reproduce a vertically extended X-ray source). This modelization often leads to measuring very low or no disc truncation in the hard state of BH X-ray binaries. However, some of the proposed solutions are questioned based on the extreme physical implications (e.g. a small height of the lamppost giving extreme physical parameters [63]) and origin and behaviour of magnetic field needed to create jets [64, 65, 66, 67, 68, 69, 70, 71, 72].

On the other hand, many observed properties of BH X-ray binaries in the hard state can be explained by the truncated disc model where the inner regions of the accretion flow are filled with a hot plasma responsible for inverse Comptonization of soft photons emitted from the disc. In this scenario, the optically thick, geometrically thick disc is truncated at some radius - see Fig. 2.6 (bottom panel) [73, 74, 75]. The

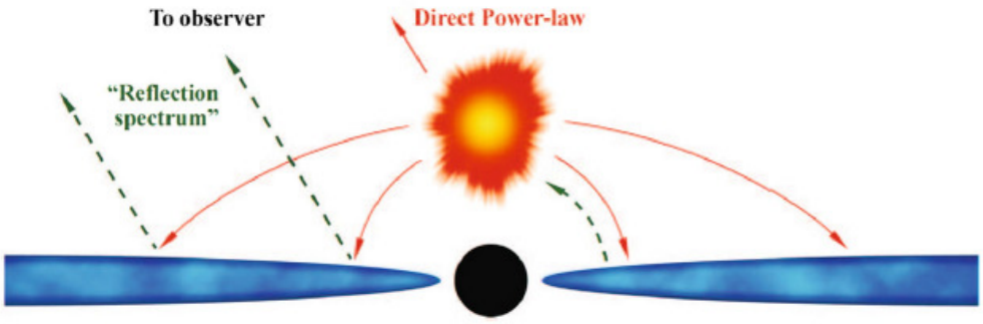

Figure 2.8: The lamppost model geometry. [43]

truncated disc model agrees with the theoretical predictions of evaporation of the inner disc [76, 77, 78, 79, 80]. It can also explain several observational properties, e.g. correlations of the relative strength of reflection with the slope of Comptonization continuum, and changes in temporal properties of the accretion discs with luminosity and spectral hardness e.g. evolution of the QPOs, observed changes of time scales in PSD [29, 11, 33, 45, 81] and long reverberation lags [44]. In the context of truncated disc models, the evolution of the source throughout an outburst is explained in terms of variations of the inner edge of the disc. This is postulated to gradually move inward as the source evolves from quiescence to the soft state. This model explains the transition from the hard to the soft state as due to the disc finally reaching R_{ISCO} (Fig. 2.6, top panel).

The main challenge of truncated disc models is represented by the observation of broad broad Fe Kα in the hard state energy spectra of these sources [82]. Extremely broadened reflection features should indeed arise from a cold accretion disc located very close to BH. This implies that the cold disc extends down to to the R_{ISCO} even in the hard state, at odds with the main assumptions of the model.

For truncated disc models to explain the observed broad Fe line a complex Comptonization continuum is usually needed, which implies a spectrally inhomogeneous (in temperature and/or optical depth) emitting region [83, 84, 85, 86, 87, 88, 2, 3].

The cold accretion disc emission that provides seed photons for the hot accretion flow is responsible for its cooling. So we can expect that in the truncated disc model the outer (closer to the truncation radius) Comptonization regions have a softer

spectrum than their inner parts, so multiple Comptonization zones are expected in this geometry. Nonetheless, an observational confirmation is still needed, as well as spectral models that can reproduce these complexities.

2.6 Motivations of the presented study

In the first part of the thesis we investigated the origin of the degeneracies obtained from the fit of reflection models, and the limitations of current spectral models [1].

In the second part we used reflection fitting on the hard state spectra, and we found that there are two statistically similar results: one corresponding to an untruncated disc, but having non-realistic inclination, and another where the disc is truncated and inclination is in agreement with that of the binary system [2].

To deal with the limitations found in the first part of the thesis we need to include additional information about the accretion flow to investigate its physics and geometry. To this aim, in the third part of the thesis we considered also the X-ray timing information.

Analyzing the variability of the observed photons allows us to see how emission is distributed as the function of the distance from the BH. Creating energy spectra of different variability components enables performing a tomography of the accretion flow [32, 33, 89, 90, 3].

This approach is based on a combined spectral-timing approach, which ultimately allows us to use all available information and disentangling different spectral components.

Bibliography

[1] Marta A. Dziełak, Andrzej A. Zdziarski, Michał Szanecki, Barbara De Marco, Andrzej Niedźwiecki, and Alex Markowitz. Comparison of spectral models for disc truncation in the hard state of GX 339-4. *MNRAS*, 485(3):3845–3856, May 2019.

[2] Andrzej A. Zdziarski, Marta A. Dziełak, Barbara De Marco, Michał Szanecki, and Andrzej Niedźwiecki. Accretion Geometry in the Hard State of the Black Hole X-Ray Binary MAXI J1820+070. *ApJ*, 909(1):L9, March 2021.

[3] Marta A. Dziełak, Barbara De Marco, and Andrzej A. Zdziarski. A spectrally stratified hot accretion flow in the hard state of MAXI J1820+070. *MNRAS*, 506(2):2020–2029, September 2021.

[4] Colin Montgomery, Wayne Orchiston, and Ian Whittingham. Michell, Laplace and the origin of the black hole concept. *Journal of Astronomical History and Heritage*, 12(2):90–96, July 2009.

[5] S. Bowyer, E. T. Byram, T. A. Chubb, and H. Friedman. Cosmic X-ray Sources. *Science*, 147(3656):394–398, January 1965.

[6] Harding E. Smith, Bruce Margon, and Peter S. Conti. Spectroscopic Observations of the Cygnus X-1 Optical Candidate. *ApJ*, 179:L125, February 1973.

[7] R. Genzel, N. Thatte, A. Krabbe, H. Kroker, and L. E. Tacconi-Garman. The Dark Mass Concentration in the Central Parsec of the Milky Way. *ApJ*, 472:153, November 1996.

[8] Event Horizon Telescope Collaboration, Kazunori Akiyama, Antxon Alberdi, Walter Alef, Keiichi Asada, Rebecca Azulay, Anne-Kathrin Baczko, David Ball, Mislav Baloković, John Barrett, Dan Bintley, Lindy Blackburn, Wilfred Boland, Katherine L. Bouman, Geoffrey C. Bower, Michael Bremer, Christiaan D. Brinkerink, Roger Brissenden, Silke Britzen, Avery E. Broderick, Dominique Broguiere, Thomas Bronzwaer, Do-Young Byun, John E. Carlstrom, Andrew Chael, Chi-kwan Chan, Shami Chatterjee, Koushik Chatterjee, Ming-Tang Chen, Yongjun Chen, Ilje Cho, Pierre Christian, John E. Conway, James M. Cordes, Geoffrey B. Crew, Yuzhu Cui, Jordy Davelaar, Mariafelicia De Laurentis, Roger Deane, Jessica Dempsey, Gregory Desvignes, Jason Dexter, Sheperd S. Doeleman, Ralph P. Eatough, Heino

Falcke, Vincent L. Fish, Ed Fomalont, Raquel Fraga-Encinas, William T. Freeman, Per Friberg, Christian M. Fromm, José L. Gómez, Peter Galison, Charles F. Gammie, Roberto García, Olivier Gentaz, Boris Georgiev, Ciriaco Goddi, Roman Gold, Minfeng Gu, Mark Gurwell, Kazuhiro Hada, Michael H. Hecht, Ronald Hesper, Luis C. Ho, Paul Ho, Mareki Honma, Chih-Wei L. Huang, Lei Huang, David H. Hughes, Shiro Ikeda, Makoto Inoue, Sara Issaoun, David J. James, Buell T. Jannuzi, Michael Janssen, Britton Jeter, Wu Jiang, Michael D. Johnson, Svetlana Jorstad, Taehyun Jung, Mansour Karami, Ramesh Karuppusamy, Tomohisa Kawashima, Garrett K. Keating, Mark Kettenis, Jae-Young Kim, Junhan Kim, Jongsoo Kim, Motoki Kino, Jun Yi Koay, Patrick M. Koch, Shoko Koyama, Michael Kramer, Carsten Kramer, Thomas P. Krichbaum, Cheng-Yu Kuo, Tod R. Lauer, Sang-Sung Lee, Yan-Rong Li, Zhiyuan Li, Michael Lindqvist, Kuo Liu, Elisabetta Liuzzo, Wen-Ping Lo, Andrei P. Lobanov, Laurent Loinard, Colin Lonsdale, Ru-Sen Lu, Nicholas R. MacDonald, Jirong Mao, Sera Markoff, Daniel P. Marrone, Alan P. Marscher, Iván Martí-Vidal, Satoki Matsushita, Lynn D. Matthews, Lia Medeiros, Karl M. Menten, Yosuke Mizuno, Izumi Mizuno, James M. Moran, Kotaro Moriyama, Monika Moscibrodzka, Cornelia Müller, Hiroshi Nagai, Neil M. Nagar, Masanori Nakamura, Ramesh Narayan, Gopal Narayanan, Iniyan Natarajan, Roberto Neri, Chunchong Ni, Aristeidis Noutsos, Hiroki Okino, Héctor Olivares, Gisela N. Ortiz-León, Tomoaki Oyama, Feryal Özel, Daniel C. M. Palumbo, Nimesh Patel, Ue-Li Pen, Dominic W. Pesce, Vincent Piétu, Richard Plambeck, Aleksandar PopStefanija, Oliver Porth, Ben Prather, Jorge A. Preciado-López, Dimitrios Psaltis, Hung-Yi Pu, Venkatessh Ramakrishnan, Ramprasad Rao, Mark G. Rawlings, Alexander W. Raymond, Luciano Rezzolla, Bart Ripperda, Freek Roelofs, Alan Rogers, Eduardo Ros, Mel Rose, Arash Roshanineshat, Helge Rottmann, Alan L. Roy, Chet Ruszczyk, Benjamin R. Ryan, Kazi L. J. Rygl, Salvador Sánchez, David Sánchez-Arguelles, Mahito Sasada, Tuomas Savolainen, F. Peter Schloerb, Karl-Friedrich Schuster, Lijing Shao, Zhiqiang Shen, Des Small, Bong Won Sohn, Jason SooHoo, Fumie Tazaki, Paul Tiede, Remo P. J. Tilanus, Michael Titus, Kenji Toma, Pablo Torne, Tyler Trent, Sascha Trippe, Shuichiro Tsuda, Ilse van Bemmel, Huib Jan van Langevelde, Daniel R. van Rossum, Jan Wagner, John Wardle, Jonathan Weintroub, Norbert Wex, Robert Wharton, Maciek Wielgus, George N. Wong, Qingwen Wu, Ken Young, André Young, Ziri Younsi, Feng Yuan, Ye-Fei Yuan, J. Anton Zensus, Guangyao Zhao, Shan-Shan Zhao, Ziyan Zhu, Juan-Carlos Algaba, Alexander Allardi, Rodrigo Amestica, Jadyn Anczarski, Uwe Bach, Frederick K. Baganoff, Christopher Beaudoin, Bradford A. Benson, Ryan Berthold, Jay M. Blanchard, Ray Blundell, Sandra Bustamente, Roger Cappallo, Edgar Castillo-Domínguez, Chih-Cheng Chang, Shu-Hao Chang, Song-Chu Chang, Chung-Chen Chen, Ryan Chilson, Tim C. Chuter, Rodrigo Córdova Rosado, Iain M. Coulson, Thomas M. Crawford, Joseph Crowley, John David, Mark Derome, Matthew Dexter, sSven Dornbusch, Kevin A. Dudevoir, Sergio A. Dzib, Andreas Eckart, Chris Eckert, Neal R. Erickson, Wendeline B. Everett, Aaron Faber, Joseph R. Farah, Vernon Fath, Thomas W. Folkers, David C. Forbes, Robert Freund, Arturo I. Gómez-Ruiz, David M. Gale, Feng Gao, Gertie Geertsema, David A. Graham, Christopher H. Greer, Ronald Grosslein, Frédéric Gueth, Daryl Haggard, Nils W. Halverson, Chih-

Chiang Han, Kuo-Chang Han, Jinchi Hao, Yutaka Hasegawa, Jason W. Henning, Antonio Hernández-Gómez, Rubén Herrero-Illana, Stefan Heyminck, Akihiko Hirota, James Hoge, Yau-De Huang, C. M. Violette Impellizzeri, Homin Jiang, Atish Kamble, Ryan Keisler, Kimihiro Kimura, Yusuke Kono, Derek Kubo, John Kuroda, Richard Lacasse, Robert A. Laing, Erik M. Leitch, Chao-Te Li, Lupin C. C. Lin, Ching-Tang Liu, Kuan-Yu Liu, Li-Ming Lu, Ralph G. Marson, Pierre L. Martin-Cocher, Kyle D. Massingill, Callie Matulonis, Martin P. McColl, Stephen R. McWhirter, Hugo Messias, Zheng Meyer-Zhao, Daniel Michalik, Alfredo Montaña, William Montgomerie, Matias Mora-Klein, Dirk Muders, Andrew Nadolski, Santiago Navarro, Joseph Neilsen, Chi H. Nguyen, Hiroaki Nishioka, Timothy Norton, Michael A. Nowak, George Nystrom, Hideo Ogawa, Peter Oshiro, Tomoaki Oyama, Harriet Parsons, Scott N. Paine, Juan Peñalver, Neil M. Phillips, Michael Poirier, Nicolas Pradel, Rurik A. Primiani, Philippe A. Raffin, Alexandra S. Rahlin, George Reiland, Christopher Risacher, Ignacio Ruiz, Alejandro F. Sáez-Madaín, Remi Sassella, Pim Schellart, Paul Shaw, Kevin M. Silva, Hotaka Shiokawa, David R. Smith, William Snow, Kamal Souccar, Don Sousa, T. K. Sridharan, Ranjani Srinivasan, William Stahm, Anthony A. Stark, Kyle Story, Sjoerd T. Timmer, Laura Vertatschitsch, Craig Walther, Ta-Shun Wei, Nathan Whitehorn, Alan R. Whitney, David P. Woody, Jan G. A. Wouterloot, Melvin Wright, Paul Yamaguchi, Chen-Yu Yu, Milagros Zeballos, Shuo Zhang, and Lucy Ziurys. First M87 Event Horizon Telescope Results. I. The Shadow of the Supermassive Black Hole. *ApJ*, 875(1):L1, April 2019.

[9] Kip S. Thorne. Disk-Accretion onto a Black Hole. II. Evolution of the Hole. *ApJ*, 191:507–520, July 1974.

[10] *Accretion Processes in Astrophysics*. Canary Islands Winter School of Astrophysics. Cambridge University Press, 2014.

[11] M. Gilfanov. *X-Ray Emission from Black-Hole Binaries*, volume 794, page 17. 2010.

[12] N. I. Shakura and R. A. Sunyaev. Reprint of 1973A&A....24..337S. Black holes in binary systems. Observational appearance. *A&A*, 500:33–51, June 1973.

[13] Steven A. Balbus and John F. Hawley. A Powerful Local Shear Instability in Weakly Magnetized Disks. I. Linear Analysis. *ApJ*, 376:214, July 1991.

[14] Toshiya Shimura and Fumio Takahara. On the Spectral Hardening Factor of the X-Ray Emission from Accretion Disks in Black Hole Candidates. *ApJ*, 445:780, June 1995.

[15] Ramesh Narayan and Insu Yi. Advection-dominated Accretion: A Self-similar Solution. *ApJ*, 428:L13, June 1994.

[16] Marek A. Abramowicz, Xingming Chen, and Ronald E. Taam. The Evolution of Accretion Disks with Coronae: A Model for the Low-Frequency Quasi-periodic Oscillations in X-Ray Binaries. *ApJ*, 452:379, October 1995.

[17] Feng Yuan and Ramesh Narayan. Hot Accretion Flows Around Black Holes. *ARA&A*, 52:529–588, August 2014.

[18] A. A. Zdziarski, W. N. Johnson, and P. Magdziarz. Broad-band γ-ray and X-ray spectra of NGC 4151 and their implications for physical processes and geometry. *MNRAS*, 283(1):193–206, November 1996.

[19] Grzegorz Wardziński and Andrzej A. Zdziarski. Effects of non-thermal tails in Maxwellian electron distributions on synchrotron and Compton processes. *MNRAS*, 325(3):963–971, August 2001.

[20] Michael A. Nowak and Robert V. Wagoner. Accretion disc turbulence and the X-ray power spectra of black hole high states. *MNRAS*, 274(1):37–47, May 1995.

[21] Marek Gierliński and Chris Done. Black hole accretion discs: reality confronts theory. *MNRAS*, 347(3):885–894, January 2004.

[22] Andrzej A. Zdziarski, Elisabeth Jourdain, Piotr Lubiński, Michał Szanecki, Andrzej Niedźwiecki, Alexandra Veledina, Juri Poutanen, Marta A. Dziełak, and Jean-Pierre Roques. Hybrid Comptonization and Electron-Positron Pair Production in the Black-hole X-Ray Binary MAXI J1820+070. *ApJ*, 914(1):L5, June 2021.

[23] A. C. Fabian, K. Iwasawa, C. S. Reynolds, and A. J. Young. Broad Iron Lines in Active Galactic Nuclei. *PASP*, 112(775):1145–1161, September 2000.

[24] I. M. George and A. C. Fabian. X-ray reflection from cold matter in Active Galactic Nuclei and X-ray binaries. *MNRAS*, 249:352, March 1991.

[25] G. Matt, G. C. Perola, and L. Piro. The iron line and high energy bump as X-ray signatures of cold matter in Seyfert 1 galaxies. *A&A*, 247:25, July 1991.

[26] K. Makishima. *Iron Lines from Galactic and Extragalactic X-ray Sources*, volume 266, page 249. 1986.

[27] G. Matt. General Relativity effects and line emission. *Astronomische Nachrichten*, 327(10):949, December 2006.

[28] P. Casella, T. Belloni, J. Homan, and L. Stella. A study of the low-frequency quasi-periodic oscillations in the X-ray light curves of the black hole candidate <ASTROBJ>XTE J1859+226</ASTROBJ>. *A&A*, 426:587–600, November 2004.

[29] Chris Done, Marek Gierliński, and Aya Kubota. Modelling the behaviour of accretion flows in X-ray binaries. Everything you always wanted to know about accretion but were afraid to ask. *A&ARv*, 15(1):1–66, December 2007.

[30] T. Belloni, M. van der Klis, W. H. G. Lewin, J. van Paradijs, T. Dotani, K. Mitsuda, and S. Miyamoto. Energy dependence in the quasi-periodic oscillations and noise of black hole candidates in the very high state. *A&A*, 322:857–867, June 1997.

[31] M. A. Nowak. Are there three peaks in the power spectra of GX 339-4 and Cyg X-1? *MNRAS*, 318(2):361–367, October 2000.

[32] Magnus Axelsson, Linnea Hjalmarsdotter, and Chris Done. Fast variability as a probe of the smallest regions around accreting black holes. *MNRAS*, 431(2):1987–1994, May 2013.

[33] Magnus Axelsson and Chris Done. Breaking the spectral degeneracies in black hole binaries with fast timing data: the hard state of Cygnus X-1. *MNRAS*, 480(1):751–758, October 2018.

[34] Adam R. Ingram and Sara E. Motta. A review of quasi-periodic oscillations from black hole X-ray binaries: Observation and theory. *New Astron. Rev.*, 85:101524, September 2019.

[35] T. Belloni, J. Homan, P. Casella, M. van der Klis, E. Nespoli, W. H. G. Lewin, J. M. Miller, and M. Méndez. The evolution of the timing properties of the black-hole transient GX 339-4 during its 2002/2003 outburst. *A&A*, 440(1):207–222, September 2005.

[36] S. Motta, T. Muñoz-Darias, P. Casella, T. Belloni, and J. Homan. Low-frequency oscillations in black holes: a spectral-timing approach to the case of GX 339-4. *MNRAS*, 418(4):2292–2307, December 2011.

[37] T. M. Belloni, S. E. Motta, and T. Muñoz-Darias. Black hole transients. *Bulletin of the Astronomical Society of India*, 39(3):409–428, September 2011.

[38] Adam Ingram, Chris Done, and P. Chris Fragile. Low-frequency quasi-periodic oscillations spectra and Lense-Thirring precession. *MNRAS*, 397(1):L101–L105, July 2009.

[39] A. L. Stevens, P. Uttley, D. Altamirano, Z. Arzoumanian, P. Bult, E. M. Cackett, A. C. Fabian, K. C. Gendreau, K. Q. Ha, J. Homan, A. R. Ingram, E. Kara, J. Kellogg, R. M. Ludlam, J. M. Miller, J. Neilsen, D. R. Pasham, R. A. Remillard, J. F. Steiner, and J. van den Eijnden. A NICER Discovery of a Low-frequency Quasi-periodic Oscillation in the Soft-intermediate State of MAXI J1535-571. *ApJ*, 865(2):L15, October 2018.

[40] Yu. E. Lyubarskii. Flicker noise in accretion discs. *MNRAS*, 292(3):679–685, December 1997.

[41] P. Arévalo and P. Uttley. Investigating a fluctuating-accretion model for the spectral-timing properties of accreting black hole systems. *MNRAS*, 367(2):801–814, April 2006.

[42] P. Uttley, T. Wilkinson, P. Cassatella, J. Wilms, K. Pottschmidt, M. Hanke, and M. Böck. The causal connection between disc and power-law variability in hard state black hole X-ray binaries. *MNRAS*, 414(1):L60–L64, June 2011.

[43] P. Uttley, E. M. Cackett, A. C. Fabian, E. Kara, and D. R. Wilkins. X-ray reverberation around accreting black holes. *A&ARv*, 22:72, August 2014.

[44] B. De Marco, G. Ponti, T. Muñoz-Darias, and K. Nandra. The evolution of the disc variability along the hard state of the black hole transient gx 339-4. *Monthly Notices of the Royal Astronomical Society*, 454(3):2360–2371, Oct 2015.

[45] Ra'ad D. Mahmoud and Chris Done. A physical model for the spectral-timing properties of accreting black holes. *MNRAS*, 480(3):4040–4059, November 2018.

[46] B. De Marco, G. Ponti, P. O. Petrucci, M. Clavel, S. Corbel, R. Belmont, S. Chakravorty, M. Coriat, S. Drappeau, J. Ferreira, G. Henri, J. Malzac, J. Rodriguez, J. A. Tomsick, F. Ursini, and A. A. Zdziarski. Evolution of the reverberation lag in GX 339-4 at the end of an outburst. *MNRAS*, 471(2):1475–1487, October 2017.

[47] M. L. McConnell, A. A. Zdziarski, K. Bennett, H. Bloemen, W. Collmar, W. Hermsen, L. Kuiper, W. Paciesas, B. F. Phlips, J. Poutanen, J. M. Ryan, V. Schönfelder, H. Steinle, and A. W. Strong. The Soft Gamma-Ray Spectral Variability of Cygnus X-1. *ApJ*, 572(2):984–995, June 2002.

[48] M. Coriat, R. P. Fender, and G. Dubus. Revisiting a fundamental test of the disc instability model for X-ray binaries. *MNRAS*, 424(3):1991–2001, August 2012.

[49] Elena Gallo, Simone Migliari, Sera Markoff, John A. Tomsick, Charles D. Bailyn, Stefano Berta, Rob Fender, and James C. A. Miller-Jones. The Spectral Energy Distribution of Quiescent Black Hole X-Ray Binaries: New Constraints from Spitzer. *ApJ*, 670(1):600–609, November 2007.

[50] Richard M. Plotkin, Elena Gallo, Sera Markoff, Jeroen Homan, Peter G. Jonker, James C. A. Miller-Jones, David M. Russell, and Samia Drappeau. Constraints on relativistic jets in quiescent black hole X-ray binaries from broad-band spectral modelling. *MNRAS*, 446(4):4098–4111, February 2015.

[51] J. P. Lasota, R. Narayan, and I. Yi. Mechanisms for the outbursts of soft X-ray transients. *A&A*, 314:813–820, October 1996.

[52] F. Bernardini, D. M. Russell, K. I. I. Kolojonen, L. Stella, R. I. Hynes, and S. Corbel. On the Optical-X-Ray Correlation from Outburst to Quiescence in Low-mass X-Ray Binaries: The Representative Cases of V404 Cyg and Cen X-4. *ApJ*, 826(2):149, August 2016.

[53] G. Dubus, J. M. Hameury, and J. P. Lasota. The disc instability model for X-ray transients: Evidence for truncation and irradiation. *A&A*, 373:251–271, July 2001.

[54] Rudy Wijnands and Michiel van der Klis. The Broadband Power Spectra of X-Ray Binaries. *ApJ*, 514(2):939–944, April 1999.

[55] Gregory J. Sobczak, Jeffrey E. McClintock, Ronald A. Remillard, Wei Cui, Alan M. Levine, Edward H. Morgan, Jerome A. Orosz, and Charles D. Bailyn. Correlations between Low-Frequency Quasi-periodic Oscillations and Spectral Parameters in XTE J1550-564 and GRO J1655-40. *ApJ*, 531(1):537–545, March 2000.

[56] P. Casella, T. Belloni, and L. Stella. The ABC of Low-Frequency Quasi-periodic Oscillations in Black Hole Candidates: Analogies with Z Sources. *ApJ*, 629(1):403–407, August 2005.

[57] Andrzej A. Zdziarski, Juri Poutanen, William S. Paciesas, and Linqing Wen. Understanding the Long-Term Spectral Variability of Cygnus X-1 with Burst and Transient Source Experiment and All-Sky Monitor Observations. *ApJ*, 578(1):357–373, October 2002.

[58] Ronald A. Remillard and Jeffrey E. McClintock. X-Ray Properties of Black-Hole Binaries. *ARA&A*, 44(1):49–92, September 2006.

[59] Tomaso M. Belloni and Sara Motta. Black-hole Binaries: Life Begins at 40 keV. In Jérôme Rodriguez and Phillippe Ferrando, editors, *SIMBOL-X: Focusing on the Hard X-ray Universe*, volume 1126 of *American Institute of Physics Conference Series*, pages 185–188, May 2009.

[60] Javier A. García, James F. Steiner, Jeffrey E. McClintock, Ronald A. Remillard, Victoria Grinberg, and Thomas Dauser. X-Ray Reflection Spectroscopy of the Black Hole GX 339–4: Exploring the Hard State with Unprecedented Sensitivity. *ApJ*, 813(2):84, November 2015.

[61] Cosimo Bambi, Laura W. Brenneman, Thomas Dauser, Javier A. Garcia, Victoria Grinberg, Adam Ingram, Jiachen Jiang, Erin Kara, Honghui Liu, Anne M. Lohfink, Andrea Marinucci, Guglielmo Mastroserio, Riccardo Middei, Sourabh Nampalliwar, Andrzej Niedzwiecki, James F. Steiner, Ashutosh Tripathi, and Andrzej A. Zdziarski. Towards precision measurements of accreting black holes using X-ray reflection spectroscopy. *Space Sci. Rev.*, page arXiv:2011.04792, November 2021.

[62] Andrea Martocchia and Giorgio Matt. Iron Kalpha line intensity from accretion discs around rotating black holes. *MNRAS*, 282(4):L53–L57, October 1996.

[63] Andrzej Niedźwiecki, Andrzej A. Zdziarski, and Michał Szanecki. On the Lamp-post Model of Accreting Black Holes. *ApJ*, 821(1):L1, April 2016.

[64] Y. F. Yuan and J. L. Zhang. The Effects of Interior Magnetic Fields on the Properties of Neutron Stars in the Relativistic Mean-Field Theory. *ApJ*, 525(2):950–958, November 1999.

[65] R. D. Blandford and R. L. Znajek. Electromagnetic extraction of energy from Kerr black holes. *MNRAS*, 179:433–456, May 1977.

[66] R. D. Blandford and D. G. Payne. Hydromagnetic flows from accretion disks and the production of radio jets. *MNRAS*, 199:883–903, June 1982.

[67] M. Liska, A. Tchekhovskoy, and E. Quataert. Large-scale poloidal magnetic field dynamo leads to powerful jets in GRMHD simulations of black hole accretion with toroidal field. *MNRAS*, 494(3):3656–3662, May 2020.

[68] G. S. Bisnovatyi-Kogan and A. A. Ruzmaikin. The Accretion of Matter by a Collapsing Star in the Presence of a Magnetic Field. *Ap&SS*, 28(1):45–59, May 1974.

[69] Ramesh Narayan, Igor V. Igumenshchev, and Marek A. Abramowicz. Magnetically Arrested Disk: an Energetically Efficient Accretion Flow. *PASJ*, 55:L69–L72, December 2003.

[70] Jonathan C. McKinney, Alexander Tchekhovskoy, and Roger D. Blandford. General relativistic magnetohydrodynamic simulations of magnetically choked accretion flows around black holes. *MNRAS*, 423(4):3083–3117, July 2012.

[71] Xinwu Cao and Hendrik C. Spruit. The Large-scale Magnetic Fields of Thin Accretion Disks. *ApJ*, 765(2):149, March 2013.

[72] Greg Salvesen, Jacob B. Simon, Philip J. Armitage, and Mitchell C. Begelman. Accretion disc dynamo activity in local simulations spanning weak-to-strong net vertical magnetic flux regimes. *MNRAS*, 457(1):857–874, March 2016.

[73] B. F. Liu, W. Yuan, F. Meyer, E. Meyer-Hofmeister, and G. Z. Xie. Evaporation of Accretion Disks around Black Holes: The Disk-Corona Transition and the Connection to the Advection-dominated Accretion Flow. *ApJ*, 527(1):L17–L20, December 1999.

[74] A. Różańska and B. Czerny. Two-phase radiative/conductive equilibrium in active galactic nuclei and galactic black holes. *MNRAS*, 316(3):473–478, August 2000.

[75] M. Mayer and J. E. Pringle. Time-dependent models of two-phase accretion discs around black holes. *MNRAS*, 376(1):435–456, March 2007.

[76] F. Meyer, B. F. Liu, and E. Meyer-Hofmeister. Evaporation: The change from accretion via a thin disk to a coronal flow. *A&A*, 361:175–188, September 2000.

[77] Pierre-Olivier Petrucci, Jonathan Ferreira, Gilles Henri, and Guy Pelletier. The role of the disc magnetization on the hysteresis behaviour of X-ray binaries. *MNRAS*, 385(1):L88–L92, March 2008.

[78] Mitchell C. Begelman and Philip J. Armitage. A Mechanism for Hysteresis in Black Hole Binary State Transitions. *ApJ*, 782(2):L18, February 2014.

[79] N. D. Kylafis and T. M. Belloni. Accretion and ejection in black-hole X-ray transients. *A&A*, 574:A133, February 2015.

[80] Xinwu Cao. An Accretion Disk-outflow Model for Hysteretic State Transition in X-Ray Binaries. *ApJ*, 817(1):71, January 2016.

[81] B. De Marco, A. A. Zdziarski, G. Ponti, G. Migliori, T. M. Belloni, A. Segovia Otero, M. Dziełak, and E. V. Lai. The inner flow geometry in MAXI J1820+070 during hard and hard-intermediate states. *arXiv e-prints*, page arXiv:2102.07811, February 2021.

[82] A. C. Fabian, M. L. Parker, D. R. Wilkins, J. M. Miller, E. Kara, C. S. Reynolds, and T. Dauser. On the determination of the spin and disc truncation of accreting black holes using X-ray reflection. *MNRAS*, 439(3):2307–2313, April 2014.

[83] Michael A. Nowak, Manfred Hanke, Sarah N. Trowbridge, Sera B. Markoff, Jörn Wilms, Katja Pottschmidt, Paolo Coppi, Dipankar Maitra, John E. Davis, and Frank Tramper. Corona, Jet, and Relativistic Line Models for Suzaku/RXTE/Chandra-HETG Observations of the Cygnus X-1 Hard State. *ApJ*, 728(1):13, February 2011.

[84] T. Di Salvo, C. Done, P. T. Życki, L. Burderi, and N. R. Robba. Probing the Inner Region of Cygnus X-1 in the Low/Hard State through Its X-Ray Broadband Spectrum. *ApJ*, 547(2):1024–1033, February 2001.

[85] Askar Ibragimov, Juri Poutanen, Marat Gilfanov, Andrzej A. Zdziarski, and Chris R. Shrader. Broad-band spectra of Cygnus X-1 and correlations between spectral characteristics. *MNRAS*, 362(4):1435–1450, October 2005.

[86] Kazuo Makishima, Hiromitsu Takahashi, Shin'ya Yamada, Chris Done, Aya Kubota, Tadayasu Dotani, Ken Ebisawa, Takeshi Itoh, Shunji Kitamoto, Hitoshi Negoro, Yoshihiro Ueda, and Kazutaka Yamaoka. Suzaku Results on Cygnus X-1 in the Low/Hard State. *PASJ*, 60:585, June 2008.

[87] Shin'ya Yamada, Kazuo Makishima, Chris Done, Shunsuke Torii, Hirofumi Noda, and Soki Sakurai. Evidence for a Cool Disk and Inhomogeneous Coronae from Wide-Band Temporal Spectroscopy of Cygnus X-1 with Suzaku. *PASJ*, 65:80, August 2013.

[88] Rupal Basak, Andrzej A. Zdziarski, Michael Parker, and Nazma Islam. Analysis of NuSTAR and Suzaku observations of Cyg X-1 in the hard state: evidence for a truncated disc geometry. *MNRAS*, 472(4):4220–4232, December 2017.

[89] M. Revnivtsev, M. Gilfanov, and E. Churazov. The frequency resolved spectroscopy of CYG X-1: fast variability of the Fe K_α line. *A&A*, 347:L23–L26, July 1999.

[90] M. Gilfanov, E. Churazov, and M. Revnivtsev. Reflection and noise in Cygnus X-1. *A&A*, 352:182–188, December 1999.

Chapter 3

Paper I

Monthly Notices of the ROYAL ASTRONOMICAL SOCIETY

MNRAS **485,** 3845–3856 (2019) doi:10.1093/mnras/stz668
Advance Access publication 2019 March 8

Comparison of spectral models for disc truncation in the hard state of GX 339–4

Marta A. Dziełak,[1★] Andrzej A. Zdziarski,[1★] Michał Szanecki,[1★] Barbara De Marco,[1] Andrzej Niedźwiecki[2] and Alex Markowitz[1,3]

[1]*Nicolaus Copernicus Astronomical Center, Polish Academy of Sciences, Bartycka 18, PL-00-716 Warszawa, Poland*
[2]*Department of Astrophysics, Łódź University, Pomorska 149/153, PL-90-236 Łódź, Poland*
[3]*Center for Astrophysics and Space Sciences, University of California, San Diego, 9500 Gilman Dr, La Jolla, CA 92093-0424, USA*

Accepted 2019 March 4. Received 2019 March 4; in original form 2018 November 21

ABSTRACT

We probe models of disc truncation in the hard spectral state of an outburst of the well-known X-ray transient GX 339–4. We test a large number of different models of disc reflection and its relativistic broadening, using two independent sets of codes, and apply it to a *Rossi X-ray Timing Explorer* spectrum in the rising part of the hard state of the 2010/11 outburst. We find our results to be significantly model dependent. While all of the models tested show best fits consistent with truncation, some models allow the disc to extend close to the innermost stable circular orbit (ISCO) and some require substantial disc truncation. The different models yield a wide range in best-fitting values for the disc inclination. Our statistically best model has a physical thermal Comptonization primary continuum, requires the disc to be truncated at a radius larger than or equal to about two ISCO radii for the maximum dimensionless spin of 0.998, and predicts a disc inclination in agreement with that of the binary. Our preferred models have moderate Fe abundance, $\gtrsim$2 times solar. We have also tested the effect of increasing the density of the reflecting medium. We find it leads to an increase in the truncation radius, but also to an increase in the Fe abundance, opposite to a previous finding.

Key words: accretion, accretion discs – black hole physics – stars: individual: GX 339–4 – X-rays: binaries – X-rays: individual: GX 339–4.

1 INTRODUCTION

The standard model (Novikov & Thorne 1973; Shakura & Sunyaev 1973) of accretion on to black holes (BHs) predicts formation of a viscously dissipating optically thick disc extending down to the radius of the innermost stable circular orbit (ISCO), $R_{\rm ISCO}$. This model explains well soft states of accreting systems, e.g. the soft spectral state of BH X-ray binaries. However, it cannot explain states in which BH binaries and active galactic nuclei emit predominantly hard X-ray radiation (see e.g. a review by Done et al. 2007). That radiation has to be instead emitted by some hot plasma. The location of this plasma remains poorly understood.

Among accreting BH sources, low-mass BH X-ray binaries represent an important class. They are transient in most of the known cases (Coriat, Fender & Dubus 2012), and spend most of the time in a quiescent state. In that state, the optically thick disc is predicted by the disc instability model to have a large inner truncation radius, $R_{\rm in} \sim 10^4 R_{\rm g}$ (Lasota, Narayan & Yi 1996; Dubus, Hameury & Lasota 2001), where $R_{\rm g} \equiv GM/c^2$ and $M \sim 10{\rm M}_\odot$ is the BH mass. The quiescence truncation radius has been measured in the case of the low-mass BH X-ray binary V404 Cyg to be $R_{\rm in} \gtrsim 3.4 \times 10^4 R_{\rm g}$ (Bernardini et al. 2016; see Narayan, Barret & McClintock 1997 for an earlier estimate). During quiescence, matter transferred from the companion accumulates in the disc and its inner radius continuously decreases (see e.g. fig. 13 of Dubus et al. 2001). Confirming the prediction of the decrease in $R_{\rm in}$, an upper limit of $R_{\rm in} \lesssim 1.2 \times 10^4 R_{\rm g}$ in V404 Cyg was obtained 13 h before the onset of the 2015 X-ray outburst (Bernardini et al. 2016).

For the parameters of Dubus et al. (2001), the hydrogen-ionization instability triggering the outburst starts at a radius of $\sim 10^{10}$ cm ($\sim 10^3 R_{\rm g}$), a radius slightly larger than $R_{\rm in}$ at that point of time, $\approx 6 \times 10^9$ cm. These radii are much lower than the typical outer disc radius of $\sim 10^{11}$ cm, and this type of outburst is called 'inside-out'. The truncation radius at the onset of an outburst can be estimated using observed time delays between the onsets of optical and X-ray flux rises as compared to the difference of the viscous time-scales, $t_{\rm vis} = R^2/\nu$ (where ν is the kinematic viscosity), at the inner disc radius at the optical flux rise, $R_{\rm in}(V)$, and the X-ray one, $R_{\rm in}(X)$, with the latter assumed by Dubus et al. (2001) to be

★ E-mail: mdzielak@camk.edu.pl (MAD); aaz@camk.edu.pl (AAZ); mitsza@camk.edu.pl (MS)

5×10^8 cm ($\sim 300 R_g$). In V404 Cyg, a ~7-d lag has been observed by Bernardini et al. (2016), from which they derived $R_{in}(V) \approx 0.9$–2.2×10^9 cm ($\sim 10^3 R_g$), somewhat lower than the value of Dubus et al. (2001) and much lower than the observational upper limit obtained 13 h before the outburst (see above). An almost identical optical-to-X-ray delay, $\approx 7 \pm 1$ d, was found in a new BH transient, ASASSN-18ey, by Tucker et al. (2018), who found $R_{in}(V) \approx 0.8$–2.5×10^9 cm.

Since the viscous time-scale decreases with decreasing radius (as $\propto R^{1/2} T_c^{-1}$, where T_c is the mid-plane disc temperature, increasing with decreasing R), the assumption of the onset of X-ray outburst at $R_{in} \approx 5 \times 10^8$ cm has only a minor effect on the derived value of $R_{in}(V)$. On the other hand, if the viscous build-up of the disc continued after the onset of the X-rays, the disc should have reached R_{ISCO} ($\sim 10^6$–10^7 cm) within a couple more days, i.e. at the beginning of the hard spectral state. We note, however, that our understanding of the mechanisms of truncation, both in quiescence and in outburst, remains very limited. The quiescence truncation radius in Dubus et al. (2001) is determined by their equation (14), from Menou et al. (2000), which, as they note, is both phenomenological and uncertain. The uncertainty is caused by our poor understanding of disc evaporation mechanisms. In the hard state, a number of different mechanisms to keep the disc truncated and change R_{in} with changing luminosity and source history (including a hysteretic behaviour of state transitions) have been proposed, e.g. Meyer-Hofmeister, Liu & Meyer (2005), Petrucci et al. (2008), Begelman & Armitage (2014), Kylafis & Belloni (2015), and Cao (2016). We conclude that the correct theoretical dependence of R_{in} on the time and luminosity after the onset of an outburst in the hard and intermediate states remains unknown.

Indeed, there is abundant evidence for the disc not reaching the ISCO at the beginning of the hard state. For example, McClintock et al. (2001) and Esin et al. (2001) found strong evidence for $R_{in} \gtrsim 50 R_g$ 3 weeks after the beginning of the 2000 outburst of the BH binary XTE J1118+480, at a luminosity of $\sim 10^{-3}$ of the Eddington luminosity, L_E. On the other hand, R_{in} certainly equals R_{ISCO} (or it is very close to it) during the soft spectral states (Ebisawa, Mitsuda & Hanawa 1991; Ebisawa et al. 1993; Gierliński & Done 2004; Steiner et al. 2011). Thus, we know that R_{in} has to decrease from some hundreds or $\sim 10^3 R_g$ at the onset of the disc instability to R_{ISCO} at the onset of the soft state.

In the case of GX 339–4, a well-studied transient low-mass BH X-ray binary, a number of authors found the presence of an optically thick disc already extending very close to the ISCO in the hard spectral state at luminosities $\gtrsim 0.01 L_E$ (Miller et al. 2006, 2008; Reis et al. 2008; Tomsick et al. 2008; Reis, Fabian & Miller 2010; Petrucci et al. 2014; Fürst et al. 2015; García et al. 2015, hereafter G15; Wang-Ji et al. 2018b). The method used was X-ray reflection spectroscopy, in which theoretical reflection spectra are fitted to data. On the other hand, other authors found highly truncated discs in the same state using the same method, and, in some cases, using the same observations (Done & Díaz Trigo 2010; Kolehmainen, Done & Díaz Trigo 2014; Plant et al. 2015; Basak & Zdziarski 2016). A truncated disc can also explain the relatively long reverberation lags measured in the soft X-ray response of the inner disc to variability of hard X-rays (De Marco et al. 2015, 2017; Mahmoud, Done & De Marco 2018).

Some of the findings of the disc extending close to the ISCO in the luminous hard state of GX 339–4 were attributed to the effect of instrumental pile-up, present in some of the *XMM–Newton* fitted spectra (as discussed by Done & Díaz Trigo 2010; Kolehmainen et al. 2014; Basak & Zdziarski 2016). This effect, present in CCD detectors, is absent in the data from *NuSTAR*, analysed by Fürst et al. (2015) and Wang-Ji et al. (2018b). However, while Fürst et al. (2015) advocated a low truncation radius, a fraction of their best-fitting models had large truncation radii, and thus their results cannot be considered as conclusive. Then, while Wang-Ji et al. (2018b) found $R_{in} \sim R_{ISCO}$ in their models, their observations were taken in a low-luminosity state of GX 339–4, which limited the statistical significance of those results. The pile-up effect was also absent in the analysis of G15, who used data from the Proportional Counter Array (PCA) on board the *Rossi X-ray Timing Explorer* (*RXTE*). G15 used the correction to the spectral response of the PCA of García et al. (2014b) and combined hard-state PCA observations with similar X-ray fluxes, which resulted in well-calibrated spectra with very large number of counts. Then, in spite of the limited spectral resolution of the PCA (typical for proportional counters), detailed reflection spectra could be fitted. The reflection model used by G15 was then extended by Steiner et al. (2017, hereafter S17), who included the effect of scattering of the reflection photons in the hot plasma emitting the X-rays irradiating the disc. The works of G15 and S17 appear to represent some of the best documented cases for low truncation radii in the hard state of GX 339–4. However, motivated by the wealth of existing controversial results, we have embarked on an independent analysis of the PCA spectra in the hard state of GX 339–4.

GX 339–4 was discovered in 1972 (Markert et al. 1973). It has since then been the most often outbursting transient BH binary. The distance to the source, D, is relatively uncertain. Zdziarski et al. (2004) obtained 7 kpc $\lesssim D \lesssim$ 9 kpc. Heida et al. (2017) found $D \gtrsim 5$ kpc and their preferred value was $D \approx 9$ kpc. Its mass function is $1.91 \pm 0.08 M_\odot$ and the mass ratio is 0.18 ± 0.05, which, with a constraint on the donor mass, give $M \lesssim 9.5 M_\odot$ (Heida et al. 2017). On the other hand, Parker et al. (2016) found $D \approx 8$–10 kpc and $M \approx (8$–$12) M_\odot$ (including both the statistical and systematic errors) based on their X-ray spectral fits. In our estimates of the luminosity and the Eddington ratio, we assume $D = 8$ kpc and $M = 8 M_\odot$ (as well as we assume the hydrogen fraction of 0.7 in the value of the Eddington luminosity). The binary inclination, i_b, of GX 339–4 has been constrained by Heida et al. (2017) to be $37^\circ \leq i_b \leq 78^\circ$. We note that an inner part of the disc can be aligned with the BH rotation axis, which, in turn, can be misaligned with the binary axis. Thus, the inclination derived from X-ray fits, i, does not have to necessarily equal i_b if the disc extends close to the ISCO.

2 THE DATA REDUCTION

RXTE was an X-ray observatory launched in 1996 and operational until 2012. The PCA (Jahoda et al. 2006) was one of the two pointed detectors on board *RXTE*. The PCA operated in the nominal energy range of 2–60 keV, and it conducted about 1400 pointed observations of GX 339–4.

We have analysed the PCA observations of GX 339–4 and extracted PCA spectra.[1] We used only the Proportional Counter Unit (PCU) 2, since it was consistently operational during *RXTE*'s entire lifetime, as well as the best-calibrated unit. We used all of the layers of the detector. We have applied the standard dead-time correction, using the commands PCADEADCALC2 and PCADEADSPECT2. For each observation, we used the PCA background model for

[1] As described in the *RXTE* data reduction cookbook: http://heasarc.nasa.gov/docs/xte/recipes/cook_book.html.

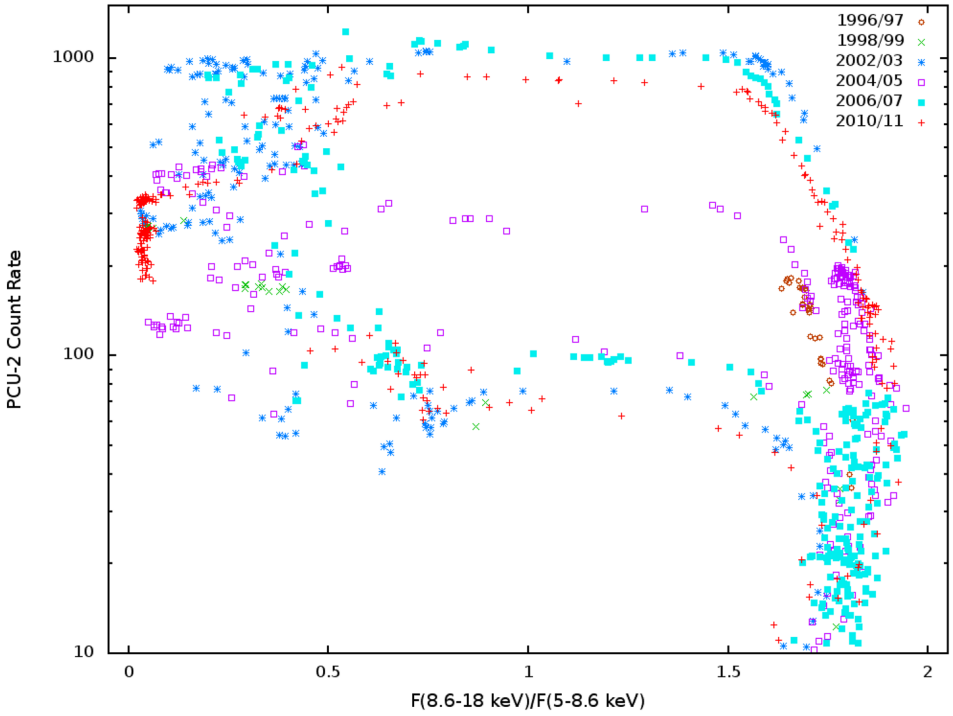

Figure 1. The diagram of the 3–45 keV count rate versus hardness for 1107 PCA observations of GX 339–4 during its six major outbursts, identified by different symbols and colours. The hardness is defined as the energy flux ratio of the 8.6–18 to 5–8.6 keV bands.

bright sources. Using the X-Ray Spectral Fitting Package (XSPEC) v. 12.10.0c (Arnaud 1996), we have fitted absorbed power-law models to all the spectra, and defined the spectral hardness as the ratio of the energy fluxes (from the model) between the 8.6–18 and 5–8.6 keV photon energy ranges. We show the PCA count rate as a function of that hardness in Fig. 1, where we also identify the six major outbursts of GX 339–4 observed by *RXTE*.

Then, in order to increase the statistical precision of spectral fits, we have combined spectra with similar flux and hardness. We have chosen the 2010/11 outburst, since it has the coverage of the rising part of the hard state with the highest dynamic range among all of the observed outbursts. The analysed observations are shown in Fig. 2. We started from the bottom, and included observations with increasing fluxes until a minimum of 10^7 counts was accumulated. In this way, we have obtained 10 sets of spectra in the hard state. We then added together observations within a set in two ways. In one, we followed the method proposed by G15. Every observation in an averaged set was fitted by an absorbed power law. The best-fitting parameters within each set were averaged and used as input parameters in FAKEIT command of XSPEC, in order to simulate an average spectrum for the continuum. The residuals were summed together, and the result added to the average absorbed power-law spectrum. For the response file, we used one of the original responses for each combined set, and we have tested that a given choice has no effect on the results. We ended up with 10 spectra at different luminosities in the hard state, which we denote using the letter G. In the second method, we obtained an summed spectrum for each set using the standard routine ADDSPEC included in the FTOOLS package, which routine also generates the appropriate response file. The resulting spectra are denoted with the letter A. In both cases, we applied the correction to the PCA effective area of García et al. (2014b), `pcacorr`, and, following the recommendation of that work, added a 0.1 per cent systematic

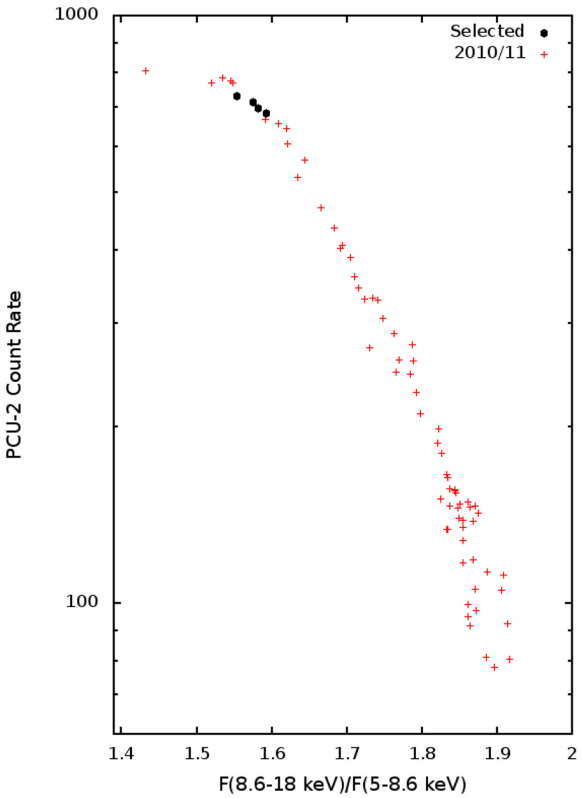

Figure 2. The 3–45 keV count rate versus hardness for the PCA observations of GX 339–4 during the rise of the 2010/11 outburst (which is a subset of the data shown in Fig. 1). The black circles mark the observations forming the average spectrum fitted in this work.

error. As shown in Section 3.3, the two procedures yield similar spectra and fitting results.

We have performed extensive spectral fitting with more than 10 different models for most of the spectral groups and for each of the averaging methods. We have generally found a strong model dependence of the results, and our full set of results has therefore become very complex. We have therefore decided to focus this work on showing and discussing results obtained from the analysis of only one spectrum, and defer the analysis of all the others as well as of the evolution of spectral parameters during the outburst to a follow-up paper. The chosen spectrum includes four among the brightest observations of the rising part of the outburst (see the black points in Fig. 2). The next brighter average spectrum is already located on an approximately horizontal part of the hardness-count rate diagram (together with ∼10 later observations of that outburst, see Fig. 1) and thus is likely to have different spectral properties than those characterizing the rising part. We have also checked that all of the four individual observations in the chosen average spectrum, taken on 2010 April 2, 3, 4, and 5 (Obsid 95409-01-13-03, 95409-01-13-00, 95409-01-13-04, 95409-01-13-02), have similar residuals with respect to the power-law fits. This is, e.g. not the case for the previous, fainter, spectrum, where one long observation shows much stronger residuals with respect to the fitted power-law than the remaining observations (possibly a consequence of calibration issues). Our selected spectrum has 1.01×10^7 counts. Its average count rate is 705.6 s^{-1}. It is similar in flux and hardness to spectrum B of G15 (note that the count rates given in G15 have been adjusted for the detector gain change over the lifetime of *RXTE* and thus cannot be directly compared with our count rate). Our spectrum has also relatively similar flux and hardness to *XMM–Newton*/EPIC-pn spectrum 7, taken during the same outburst on 2010 March 28 (Basak & Zdziarski 2016).

3 SPECTRAL ANALYSIS

3.1 Methodology

After preliminary spectral fitting with XSPEC, we used the command STEPPAR to scan the parameter space and find the model with the overall lowest χ^2. After that, we determine the 90 per cent confidence range for a single parameter, $\Delta\chi^2 = +2.71$, corresponding to the value farthest away from the best fit, also using STEPPAR. Note that occasionally this procedure gives a limit within a local minimum separated from the best fit by a parameter range with $\Delta\chi^2 > 2.71$.

We then check for degeneracy between parameters of our models and further explore their parameter spaces using a Markov Chain Monte Carlo (MCMC) algorithm. We use the `xspec_emcee` implementation (by Jeremy Sanders based on Foreman-Mackey et al. 2013 and Goodman & Weare 2010). Also, we have used the standard XSPEC tools, for which we have tested both types of algorithms implemented, Metropolis-Hastings and Goodman-Weare, and two assumed error distributions, Gaussian and Cauchy. We have applied the MCMC method to all models in this paper, but present results graphically only for model 6, which is as presented in Section 3.6. For that, we used `xspec_emcee` with 50 so-called walkers with 240 000 iterations each, discarding the first 5000. The autocorrelation length calculated for each free fit parameter is approximately 80 times smaller than chain length. We note that with the MCMC we have not found any better fits than those found using STEPPAR. We also note that the confidence ranges determined with the MCMC method in XSPEC usually correspond to the global minima only, and do not include possible local minima away from the global one (which we find using STEPPAR).

Most of our models are not nested. Thus, we need a criterion to compare models different from the *F*-test. We use the Akaike information criterion (AIC; Akaike 1973; Sugiura 1978), which has been relatively widely used in astrophysics (e.g. Koen 2006; Liddle 2007; Natalucci et al. 2014; Lubiński et al. 2016; Tang 2018). We use a formula with a correction for the finite size of sample,

$$\mathrm{AIC}_i = 2\,m - 2C_\mathrm{L} + \chi^2 + \frac{2\,m(m+1)}{n-m-1}, \quad (1)$$

where C_L is a likelihood function of the true model (which depends only on the data set), m is the number of free parameters of a model, n is the number of channels in the fitted spectrum, and i is the model number. The lower the AIC value, the better the model. Since the models are compared through a difference in their AIC values, the likelihood C_L cancels out. The relative likelihood for a model with a larger value of AIC_i compared to the best one with the minimum AIC, which we denote as AIC_0, is $\exp[(\mathrm{AIC}_0 - \mathrm{AIC}_i)/2]$, which is unity for $\mathrm{AIC}_i = \mathrm{AIC}_0$ and ≈0 for $\mathrm{AIC}_i \gg \mathrm{AIC}_0$. Instead of normalizing to the best model, we can also normalize the likelihood to unity for the sum of all considered I models (Akaike 1978),

$$p_k = \frac{\exp(-\mathrm{AIC}_k/2)}{\sum_{i=1}^{I}\exp(-\mathrm{AIC}_i/2)}, \quad (2)$$

with $\sum p_k = 1$. We give the values of p_k for our models in Table 1.

3.2 The ISM absorption column towards GX 339–4

In all our models, the ISM absorption is taken into account by the model `tbabs` (Wilms, Allen & McCray 2000). The description of that model[2] recommends the use of the cosmic abundances of Wilms et al. (2000). However, the actual ISM abundances in the direction to GX 339–4 remain uncertain, and G15 used instead the abundances of Anders & Grevesse (1989). In our models, we have tested the effects of changing the abundances on the fits, and found it to be relatively minor, except for the fitted value of the absorption column density, which was substantially higher for the abundances of Wilms et al. (2000). Therefore, from this point onwards, we follow G15 and use the abundances of Anders & Grevesse (1989).

The actual value of the absorption column towards GX 339–4, N_H, also remains somewhat uncertain. Since the data we use are for $E > 3$ keV only, we need to constrain the allowed range of N_H. Zdziarski et al. (1998) listed a number of previous determinations of it, and found it to be in the approximate range of (5–7) × 10^{21} cm^{-2}. The best-fitting models of Fürst et al. (2015) yield ≈8 × 10^{21} cm^{-2}. Basak & Zdziarski (2016) obtained (7.0 ± 0.1) × 10^{21} cm^{-2} for the abundances of Anders & Grevesse (1989) when fitting a set of seven *XMM–Newton*/EPIC-pn observations. Based on the results listed above, we hereafter assume N_H to be in the range of (4–8) × 10^{21} cm^{-2}. We stress that since X-ray absorption depends mostly on the column densities of metals, the true value of the ISM N_H depends strongly on the abundances of heavy elements.

[2] http://pulsar.sternwarte.uni-erlangen.de/wilms/research/tbabs

Table 1. The spectral fitting results for our models applied to data set G. Model 0 follows the original assumptions of G15, which appear unphysical, and model 6 is our best model, with a physical primary continuum from thermal Comptonization. All models have the ISM absorption term `tbabs`. Model 0: [`relxill`(free Z_{Fe})+`xillver`(Z_{Fe}=1)]`gabs`; Models 1 and 2: `relxill+xillver`; Model 3: `relxillD+xillverD`; Models 4 and 5: `reflkerrExp+hreflectExp`; Model 6: `reflkerr+hreflect`. Models 0, 1, 3, 4, and 6 have high and low ionization values for the close and distant reflectors, respectively, while models 2 and 5 have the ionization structure reversed. The effect of scattering of the reflection component is taken into account in separate models with `simplcut` (see Section 3), for which we give here the values of the scattering fraction, f_{sc}, in the last row of the table.

Parameter/model	0	1	2	3	4	5	6
$N_H/10^{21}$ cm^{-2}	$5.2^{+1.8}_{-1.2}$	$4.7^{+1.5}_{-0.3}$	$6.5^{+1.3}_{-1.7}$	$6.1^{+0.7}_{-0.6}$	$4.4^{+1.9}_{-0.4}$	$6.4^{+0.8}_{-1.1}$	$4.3^{+0.5}_{-0.3}$
Γ	$1.70^{+0.07}_{-0.04}$	$1.66^{+0.03}_{-0.04}$	$1.72^{+0.02}_{-0.03}$	$1.70^{+0.01}_{-0.05}$	$1.66^{+0.06}_{-0.02}$	$1.72^{+0.03}_{-0.01}$	–
y	–	–	–	–	–	–	$1.19^{+0.05}_{-0.08}$
E_{cut}/keV	200^{+130}_{-50}	250^{+50}_{-20}	300^{+80}_{-50}	300f	240^{+50}_{-50}	280^{+50}_{-20}	–
$kT_e/1$ keV	–	–	–	–	–	–	20^{+3}_{-2}
R_{in}/R_{ISCO}	11^{+10}_{-10}	19^{+33}_{-6}	$53^{+\infty}_{-26}$	$55^{+\infty}_{-34}$	15^{+31}_{-12}	$58^{+\infty}_{-28}$	$47^{+\infty}_{-45}$
Z_{Fe}	$8.1^{+1.9}_{-5.5}$	$3.1^{+2.0}_{-0.3}$	$2.4^{+0.3}_{-0.2}$	$4.9^{+4.1}_{-0.9}$	$3.9^{+0.8}_{-1.4}$	$2.6^{+0.6}_{-0.4}$	$3.3^{+1.7}_{-1.0}$
i [°]	29^{+31}_{-29}	3^{+33}_{-3}	43^{+17}_{-23}	3^{+43}_{-3}	9^{+32}_{-9}	43^{+21}_{-19}	49^{+34}_{-26}
$\mathcal{R}$ (inner)	$0.059^{+0.001}_{-0.001}$	$0.170^{+0.004}_{-0.005}$	$0.144^{+0.004}_{-0.003}$	$0.059^{+0.033}_{-0.006}$	$0.25^{+0.04}_{-0.19}$	$0.35^{+0.06}_{-0.12}$	$0.42^{+0.36}_{-0.12}$
$\log_{10}\xi$ (inner)	$3.7^{+0.2}_{-0.5}$	$3.9^{+0.1}_{-0.1}$	$0.0^{+2.3}$	$3.7^{+0.1}_{-0.1}$	$3.9^{+0.1}_{-0.1}$	$1.7^{+0.7}_{-1.7}$	$3.9^{+0.1}_{-0.3}$
$\log_{10}\xi$ (outer)	0f	$1.7^{+0.5}_{-1.7}$	$3.8^{+0.2}_{-0.3}$	$0.7^{+1.0}_{-0.3}$	$2.0^{+0.3}_{-0.4}$	$3.7^{+0.1}_{-0.3}$	0f
$n_e/1$ cm^{-3}	10^{15}f	10^{15}f	10^{15}f	10^{19}f	10^{15}f	10^{15}f	10^{15}f
$\delta(gabs)$	$0.011^{+0.011}_{-0.009}$	–	–	–	–	–	–
$kT_{bb}/1$ keV	–	–	–	–	–	–	$0.34^{+0.04}_{-0.09}$
χ^2_ν	65.6/61	68.7/61	68.3/61	72.4/62	69.1/61	69.2/61	62.1/61
p_i (AIC)	0.136	0.007	0.008	0.018	0.024	0.023	0.784
f_{sc}	$0^{+0.27}$	$0^{+0.29}$	$0^{+0.31}$	$0^{+0.12}$	$0^{+0.26}$	$0^{+0.79}$	$0.30^{+0.15}_{-0.30}$

Notes. We assume the dimensionless spin $a_* = 0.998$, for which $R_{ISCO} \approx 1.237R_g$. $\delta(gabs)$ is the energy-integrated depth of the 7.2 keV line. We use the symbol ∞ to denote that the upper limit of R_{in} approaching $R_{out} = 10^3R_g$, which is the maximum radius for which relativistic broadening is calculated in `relxill` and `reflkerr`. The Compton parameter is defined as $y \equiv 4(kT_e/m_ec^2)\tau_T$, where τ_T is the Thomson optical depth of the slab (approximating the corona). 'f' denotes a fixed parameter. The fitted ranges of $N_H/10^{21}$ cm^{-2}, Z_{Fe} and $\log_{10}\xi$ are constrained to [4, 8], $\leq$10 and $\geq$0, respectively. The reflection fraction, $\mathcal{R}$, is the ratio of photons emitted towards the disc to those escaping to infinity in `relxill` (Dauser et al. 2016), and is the fraction of locally emitted photons in the direction of the disc in `reflkerr` (Niedźwiecki, Szanecki & Zdziarski 2019).

3.3 Models with relxill and two Fe abundances

G15 assumed a reflection emissivity profile of $\propto R^{-3}$ down to $R_{in} \geq R_{ISCO}$. This corresponds either to a corona sandwiching a standard disc (except for the neglect of the zero-stress inner boundary condition) or a central hot flow irradiating an outer disc. In either case, the assumed profile implies the reflection profile to be moderately centrally dominated. The reflected spectra are relativistically broadened. G15 used version 0.2g of the model `relxill`[3] (García et al. 2014a). That model combines the `xillver` model (Dauser et al. 2010; García & Kallman 2010), which describes rest-frame angle-dependent reflected spectra (under the assumption of the constant electron density of the reflecting medium at $n_e = 10^{15}$ cm^{-3}), with the relativistic blurring model of `relline` (Dauser et al. 2010). The incident photons have an e-folded power-law photon spectrum, $\propto E^{-\Gamma}\exp(-E/E_{cut})$, where Γ is the photon index and E_{cut} is the e-folding energy. In addition to the relativistically blurred reflection, it contains a static-reflection component `xillver`, which accounts for reflection from remote parts of the accretion disc. Also, they found it necessary to include an additional narrow absorption line at $\approx$7.2 keV. Thus, their model has the form of `tbabs(relxill+xillver)gabs`. Furthermore, G15 found that in order to achieve a good fit with this model, they had to fix that abundance for the static-reflection component (`xillver`) at the solar value while they allowed a free Fe abundance of the relativistically blurred component. In addition, they assumed that the reflecting surface for the static component is close to neutral, with an ionization parameter $\xi = 1$ erg cm^{-2} s^{-1}, where

$$\xi \equiv \frac{4\pi F_{irr}}{n_e}, \tag{3}$$

and F_{irr} is the irradiating flux in the 13.6 eV–13.6 keV band. That value of ξ is the minimum one for which the above reflection models are defined.

We first fit our data set G with this model. However, we use the current version of the `relxill` software, 1.2.0. This version agrees relatively well with the independently developed code, `reflkerrExp`, of Niedźwiecki et al. (2019).

We found that we cannot constrain the BH spin, with no difference in χ^2 between the maximum spin of $a_* = 0.998$ and 0. Therefore, we hereafter fix $a_* = 0.998$, for which $R_{ISCO} \approx 1.237R_g$. Also, we assume the largest outer radius allowed in the `relxill` model, $R_{out} = 10^3R_g$. For the spectrum obtained with the method of G15, we find the inner radius of $R_{in} \approx 10.6^{+9.6}_{-9.3}R_{ISCO}$ (see model 0 in Table 1). Thus, while the model's best-fitting value indicates a significantly truncated disc, it is consistent with being very close to the ISCO, as found by G15. Hereafter, the full results of the spectral fitting are given in Table 1, while we also give some crucial values in the text.

In spite of the low value of $\chi^2 = 65.6$ for 61 d.o.f. (whose ratio we hereafter denote as χ^2_ν), we see the presence of significant residuals at energies $\gtrsim$25 keV, as shown in Figs 3 and 4. The origin is instrumental, due to the Xe K edge of the detector (Jahoda et al. 2006), but their presence does not affect the fit at lower

[3] http://www.sternwarte.uni-erlangen.de/dauser/research/relxill/

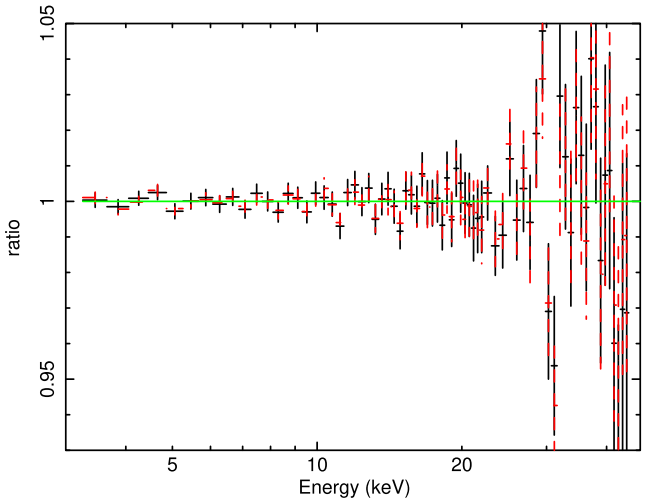

Figure 3. The data-to-model ratios of the model of G15 fitted to the data sets G (black solid crosses; model 0) and A (red dashed crosses).

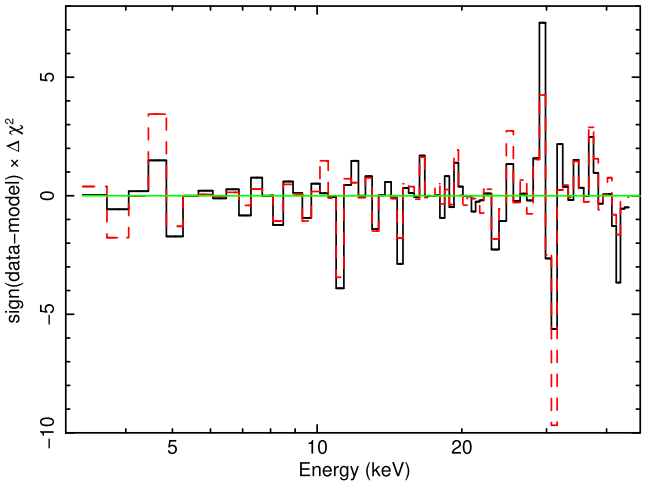

Figure 4. The contributions to χ^2 of the model of G15 fitted to the data set G (black solid histogram; model 0) and A (red dashed histogram).

energies, including the range of the Fe K complex. The required Fe abundance (with respect to the assumed cosmic one) is very high, $Z_{\rm Fe} = 8.1^{+1.9}_{-5.5}$, where the upper limit is at the highest allowed value in the `xillver` model. The reflector inclination is $i = 29^{+31^\circ}_{-29}$. The contribution of the static reflection at 30 keV is about half that of the relativistically broadened reflection. The removal of the absorption line at 7.2 keV results in $\Delta\chi^2 \approx +4.1$. Allowing a free line energy results in no improvement to the fit ($\Delta\chi^2 \approx 0.0$).

We then fit data set A, for which the results are only slightly different. We find $R_{\rm in} \approx 14^{+2}_{-3} R_{\rm ISCO}$, $i \approx 31^{+2^\circ}_{-2}$, $Z_{\rm Fe} \approx 4.1^{+5.9}_{-1.0}$, $\log_{10}\xi \approx 3.4^{+0.3}_{-0.2}$, $\chi^2_\nu \approx 64.8/61$, and other parameters similar to those found for data set G. As we can see as in Fig. 3, the model-to-data ratios for data sets G and A are very similar. The inner radius is compatible with being within $2R_{\rm ISCO}$. For this data set, removing the absorption line results in only a slight increase in χ^2, by +1.7. Given the similarity of the two spectra, we hereafter follow G15 and use only data set (G) obtained with their method. We note that our finding of similar-quality fits with both methods differs from that of G15, who found their fit to a summed spectrum to yield a much larger χ^2 than that using their method.

We then consider the effect of Comptonization of the reflection component. In the coronal geometry, some of the reflected emission will pass through the corona and be scattered in it. This effect has been considered by S17 using the model `simplcut`.[4] The main parameter of it is the scattering fraction, $f_{\rm sc}$, which is the fraction of the reflected photons that are Compton scattered in the corona, with $1 - f_{\rm sc}$ reaching the observer unmodified. Then, the scattered part of the spectrum is split between parts leaving the source and hitting the disc (where photons are removed from the model), as given by the reflection-fraction parameter of `simplcut`. In order to account for up- and down-scattering of photons out of the energy range of the PCA detector, we have extended the range of the photon energy used to calculate the models to 0.1–1000 keV with 2000 logarithmically spaced bins. In that model, there are two options for the scattering kernel. In one, photons are scattered into an e-folded power-law distribution (with the kernel given by equation 1 of S17), the same as the incident spectrum of `relxill` (see above). In the other, the Compton scattering model `nthcomp` (Zdziarski, Johnson & Magdziarz 1996) is used.

In S17, the former kernel was used for consistency with the assumption that the incident spectrum is an e-folded power law. Those authors also replaced the incident spectrum of `relxill` by `simplcut(ezdiskbb)`, where `ezdiskbb` is a multicolour disc blackbody model allowing for a disc truncation (Zimmerman et al. 2005). The resulting spectrum differs from an e-folded power law only at low energies, where the contribution of the disc blackbody is substantial. However, our data set does not show any soft excess and we have opted to keep the e-folded power law as the incident spectrum (and keep $\mathcal{R}$, Γ, and $E_{\rm cut}$ equal to those fitted in `relxill`). This is also consistent with the calculations of the reflection in `relxill`. Thus, our model has the form `tbabs[cutoffpl+simplcut(relxill)+xillver]gabs`, where the `relxill` component gives now only the spectrum reflected by the e-folded power law. We have applied this model to the data set G. We have found that the best-fitting scattering fraction is null, and $f_{\rm sc} = 0^{+0.27}$. Thus, Comptonization of reflection does not improve the fit and does not produce significant changes to the best-fitting parameters of the model of G15 as applied to the present data set and using the current version of `relxill`.

3.4 Models with relxill and a single Fe abundance

Now, we tie the Fe abundance for the static and relativistic reflection components and allow the former to be ionized. With this change, we find that the models no longer require the additional absorption line at 7.2 keV. Thus, our model has the form of `tbabs(relxill+xillver)`. We find good fits with two kinds of models. In one, the blurred reflector is strongly ionized while the distant one is close to neutral, which is similar to the original model of G15 except for their assumptions of the separate Fe abundances and the presence of the absorption line. In the other, the blurred reflector is close to neutral while the distant one is strongly ionized. We note that both models have the same form, as given above. Thus, they actually represent two local minima of the same model. However, since their physical configurations are different while the χ^2 values are similar, we consider them separately.

In the first model, we obtain a somewhat worse fit than that in Section 3.3, $\chi^2_\nu = 68.7/61$, and obtain $R_{\rm in} \approx 19^{+33}_{-6} R_{\rm ISCO}$ and $Z_{\rm Fe} \approx 3.1^{+2.0}_{-0.3}$. For the second model, $\chi^2_\nu = 68.3/61$, and $R_{\rm in} \approx$

[4] http://jfsteiner.synology.me/wordpress/simplcut/

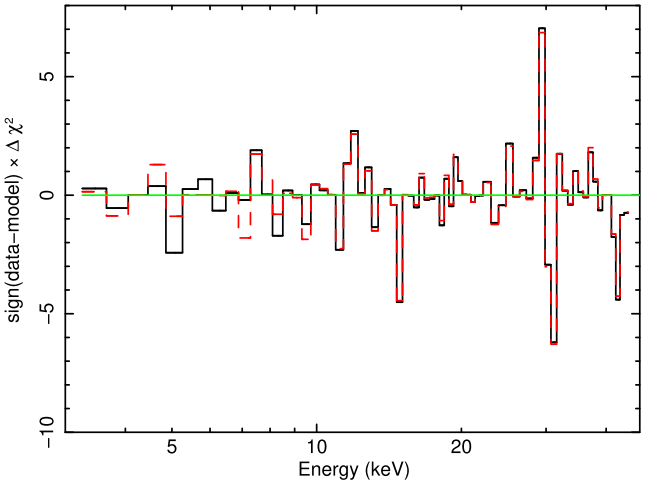

Figure 5. The contributions to χ^2 of the `relxill`-type models with exponential cut-off. The black solid and red dashed histograms correspond to the models with the high (model 1) and low (model 2) ionization, respectively, of the close, relativistically-broadened, reflector. The vertical scales are the same as in Fig. 4.

$53^{+\infty}_{-26} R_{\rm ISCO}$, $Z_{\rm Fe} \approx 2.4^{+0.3}_{-0.2}$; see models 1 and 2, respectively, in Table 1. Hereafter, we use the symbol ∞ to denote that the upper limit of $R_{\rm in}$ is approaching $R_{\rm out}$. We note that the ionization parameter of the low-ionization disc part is very weakly constrained, and allowing it to be free only marginally improves the fit. Still, here and in most of the following models, we have opted not to freeze it at $\xi = 1$ in order to show the range allowed by the data. The contributions to χ^2 from the two models are shown in Fig. 5. We see that while the values of χ^2 for these models are somewhat higher than those in Section 3.3, the differences in their contributions per energy channel are very minor. We note that now the Fe abundances have lower, and much more likely, values than in the original model of G15. Also, both of our models give large truncation radii. The two models have the parameters relatively similar to each other except for the interchanged ionization parameters. This is possible because of the large fitted truncation radii, implying that the relativistic broadening is modest. There is also some difference in the strength of the reflection components. In the first model, the distant reflection component has a flux at 30 keV of about half of the flux in the relativistic component, while in the second model both reflection components' fluxes become very similar at high energies.

We then consider the effect of the electron density of the reflector. In `xillver`, $n_{\rm e} = 10^{15}$ cm^{-3} is assumed, which is likely to be too low for accretion discs in BH binaries. The effect of the value of $n_{\rm e}$ on the reflection spectra was investigated by García et al. (2016). They pointed out an increase in thermal emission at low energies for a given value of ξ (since then the irradiating flux is then $\propto n_{\rm e}$ and the effective temperature is $\propto n_{\rm e}^{1/4}$), which should not affect our results obtained at $\geq$3 keV. Also, the reflector temperature increases, which results in a higher ionization state. Currently, there are available models with $n_{\rm e}$ up to 10^{19} cm^{-3}, namely `xillverD` and `relxillD` (García et al. 2016), while models for higher $n_{\rm e}$ are under development (García et al. 2018). Those two models assume that the e-folding energy is fixed at 300 keV, which is within the 90 per cent confidence regime of our models 1 and 2. Thus, we fit that model to the data. We consider only the case with low ionization of the remote reflector. The fit results for this model, #3, are given in Table 1. With respect to the corresponding model 1, we find a larger disc truncation radius, $R_{\rm in} \approx 55^{+\infty}_{-34} R_{\rm ISCO}$, and a higher Fe abundance, $Z_{\rm Fe} \approx 4.9^{+4.1}_{-0.9}$. The fit has a higher value of $\chi^2_\nu \approx 72.4/62$, which appears to be mostly due to the fixed value of $E_{\rm cut}$. We discuss these results in the context of other similar studies in Section 4.

We have then included Compton scattering of the reflected emission in the same way as in Section 3.3. We have found that in all three cases the best-fitting scattering fraction was zero (see Table 1).

3.5 Models with reflkerrExp (incident e-folded power law)

We now consider models of Niedźwiecki et al. (2019). The differences of these models with respect to `relxill` are described in detail in that paper. One difference is that the `relxill` assumes the incident spectra to have the high-energy cut-off (or temperature) constant with the disc radius in the observer's frame, i.e. the incident spectra in the local frames are blueshifted with respect to that given as the model cut-off by $1 + z(r)$. On the other hand, `reflkerr` (Niedźwiecki et al. 2019) assumes the incident spectrum to be constant with radius in the local frames, i.e. the observed spectrum is the sum of the local spectra redshifted by $1 + z(r)$. Also, reflection in the `reflkerr` model merges the detailed photoionization calculations of `xillver` at low energies with the relativistically correct treatment of `ireflect` (Magdziarz & Zdziarski 1995) at high energies.

We first consider models with incident power-law spectra with exponential cut-offs. The model is then `tbabs(reflkerrExp+hreflectExp)`, where `reflkerrExp` includes relativistic broadening, and `hreflectExp` is the corresponding static model. Similar to our results in Section 3.4, we find two possible models, with interchanged ionization parameter. In the model with high ionization of the blurred reflector, we obtain a fit with $\chi^2_\nu \approx 69.1/61$. We find $R_{\rm in} \approx 15^{+31}_{-12} R_{\rm ISCO}$, $Z_{\rm Fe} \approx 3.9^{+0.8}_{-1.4}$; see model 4 in Table 1. The distant reflection component contributes about half of the flux of the relativistic one at 30 keV. The bolometric flux of this model is $\approx 2.6 \times 10^{-8}$ erg cm^{-2} s^{-1}, corresponding to a luminosity of $L \approx 2.0 \times 10^{38} (D/8\,{\rm kpc})^2$ erg s^{-1}, and $L/L_{\rm E} \approx 0.17 (D/8\,{\rm kpc})^2 (M/8\,{\rm M}_\odot)^{-1}$.

For the model with low ionization of the close reflector, we find $\chi^2_\nu \approx 69.2/61$, $R_{\rm in} \approx 58^{+\infty}_{-28} R_{\rm ISCO}$, and $Z_{\rm Fe} \approx 2.6^{+0.6}_{-0.4}$ (see model 5 in Table 1). Both reflection components become almost identical at high energies. Taking into account Comptonization of the reflected radiation does not improve the fit in both cases (see the values of $f_{\rm sc}$ in Table 1).

We can see a very good agreement between the results obtained with the current version (1.2.0) of `relxill` and with `reflkerrExp`. The two sets of models have almost identical parameters and the values of χ^2; compare models 1 and 2 with models 4 and 5, respectively, in Table 1.

3.6 Models with reflkerr (incident thermal Comptonization)

We then consider models of Niedźwiecki et al. (2019) with the incident spectrum described by the thermal Comptonization, for which they use the model `compps` of Poutanen & Svensson (1996). Our present model has the form of `tbabs(reflkerr+hreflect)`. For the model with high ionization of the close reflector, we find $\chi^2_\nu \approx 62.1/61$, $R_{\rm in} \approx 47^{+\infty}_{-45} R_{\rm ISCO}$ (with the lower 90 per cent confidence limit at $R_{\rm in} \approx 1.8 R_{\rm ISCO} \approx 2.2 R_{\rm g}$) and $Z_{\rm Fe} \approx 3.3^{+1.7}_{-1.0}$ (see model 6 in Table 1). The temperature of the Comptonizing medium is $kT_{\rm e} \approx 20^{+3}_{-2}$ keV, and the temperature of blackbody seed

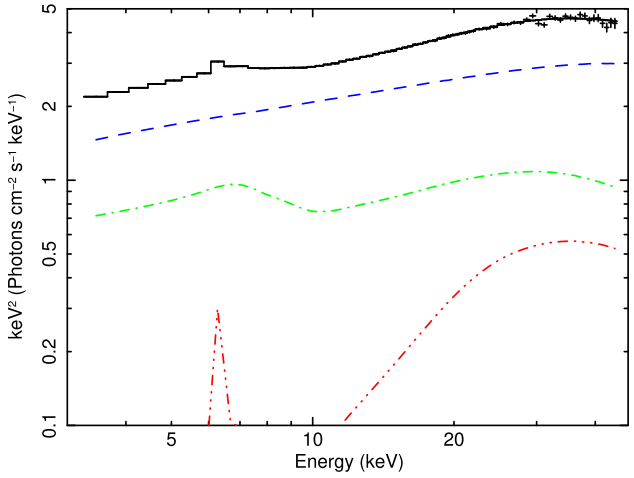

Figure 6. The histogram shows the unfolded spectrum (for model 6) as fitted by thermal Comptonization (dashed blue curve) and two reflectors, an inner highly ionized one (dot–dashed green curve), and an outer weakly ionized one (triple dot–dashed red curve). The solid curve gives the total model.

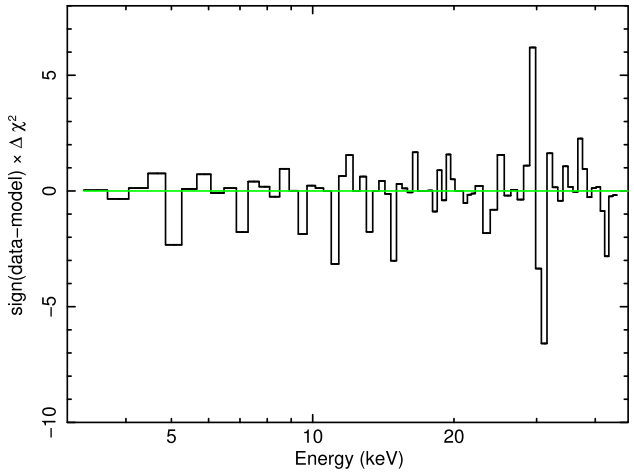

Figure 7. The contributions to χ^2 of the `reflkerr` model (#6) with the incident spectrum due to thermal Comptonization and high ionization of the relativistically broadened reflector. The vertical scales are the same as in Fig. 4.

photons is $kT_{\rm bb} \approx 0.34^{+0.04}_{-0.09}$ keV. The Compton parameter, $y \equiv 4(kT_{\rm e}/m_{\rm e}c^2)\tau_{\rm T}$, where $\tau_{\rm T}$ is the Thomson optical depth of the slab (approximating the corona), is $y \approx 1.19^{+0.05}_{-0.08}$. The distant reflection contributes about two-thirds of the flux of the relativistic one at 30 keV. In this model, in order to directly compare it to the model of G15, we have kept the ionization parameter fixed at $\xi = 1$. If we allow it to be free, $\log_{10}\xi \approx 0^{+1.9}$. The unfolded spectrum and the model are shown in Fig. 6 and the χ^2 contributions are shown in Fig. 7.

The posterior probability distributions and correlations between the parameters obtained using the MCMC technique (see Section 3.1) are shown in Fig. 8, obtained using the package of Foreman-Mackey (2016). We see here rather wide probability distributions of $R_{\rm in}$, which, however, become very small for $R_{\rm in} \lesssim 10R_{\rm ISCO}$. The strongest correlations include the positive ones between ξ(inner), $Z_{\rm Fe}$ and y. Also, there is some positive correlation between $\mathcal{R}$(inner) and the inclination. Overall, we see that this model has its parameters relatively well constrained, except for the relatively wide allowed range of $R_{\rm in}$.

Including Comptonization of reflection very slightly reduces the value of χ^2, to $\chi^2_\nu \approx 62.0/60$, at $f_{\rm sc} \approx 0.30^{+0.15}_{-0.30}$, and yields very similar other parameters. The relatively low value of $f_{\rm sc}$ can be reconciled with the relatively large $\tau_{\rm T}$ of the model in the geometry of a central hot flow surrounded by a truncated disc, in which relatively few reflected photons return into the hot flow (see e.g. Zdziarski, Lubiński & Smith 1999; Poutanen, Veledina & Zdziarski 2018).

S17 also considered models without the presence of a distant reflector. Here, we confirm their conclusion that such models give a much worse description of the data using our model 6. If we do not include the static reflection component, we obtain $\Delta\chi^2 \simeq +22$ for one less d.o.f., which corresponds to the probability of the fit improvement by adding that component being by chance of 2×10^{-5} (using the F-test).

In the case with low ionization of the close reflector, we also find a very good model, for which $\chi^2_\nu \approx 63.8/60$, $R_{\rm in} \approx 100^{+\infty}_{-62}R_{\rm ISCO}$, $Z_{\rm Fe} \approx 2.9^{+0.5}_{-0.3}$, and $i \approx 18^{+57^\circ}_{-6}$. The high-ionization, distant reflection actually dominates in this model, with its flux at 30 keV being higher by ≈1.7 than that of the close reflection. Including Comptonization of reflection (using `simplcut` with the `nthcomp` scattering kernel) improves the fit only marginally. For the sake of the simplicity of the presentation, this model is not included in Table 1.

4 DISCUSSION AND CONCLUSIONS

Our main finding is that X-ray spectra of the hard state of GX 339–4 from the PCA can be fitted with similar statistical quality with models allowing significantly different disc truncation radii, namely with $R_{\rm in}$ either close to or much larger than $R_{\rm ISCO}$. Still, all of the fitted models prefer the latter at their best-fitting values. This is the case ($R_{\rm in} \approx 11R_{\rm ISCO}$) even for the original model (#0 in Table 1) of G15 fitted to our average PCA spectrum with the current version of the `relxill` software. That model, however, requires the presence of a 7.2 keV absorption line, separate Fe abundances for the two reflectors, and a high value of the Fe abundance for the relativistic reflector.

While the presence of an absorption line at 7.2 keV is in principle possible, it has not been found in other observations of GX 339–4. In systematic studies of BH X-ray binaries, GX 339–4 shows the same properties as systems without disc-wind absorption lines. In particular, the shape of the track on the hardness-count rate diagram of GX 339–4 favours a relatively low inclination (Muñoz-Darias et al. 2013). Also, high-ionization Fe K absorption lines in the soft state, which trace disc winds, have not been detected in GX 339–4 (Ponti et al. 2012). Then, while the assumption of strongly different Fe abundances in the two reflectors can be motivated by our lack of knowledge of the true model of the accretion flow, it does not have a direct physical interpretation.

On the other hand, we have found alternative models (#1–6 in Table 1), which rule out $R_{\rm in} \approx R_{\rm ISCO}$ at 90 per cent confidence. In particular, if we impose a common Fe abundance in both reflection components and keep the assumption of the exponential cut-off of the incident spectrum (models 1–5), we find $R_{\rm in} \gtrsim 6R_{\rm ISCO}$, using either `relxill` or `reflkerrExp`. The models no longer require the 7.2 keV absorption line and their fitted Fe abundances are relatively moderate, $Z_{\rm Fe} \gtrsim 2$. Still, they have somewhat higher value of χ^2 than the model following the assumptions of G15, with $\Delta\chi^2 \approx 2$–3. Also, those models in the variant with high ionization of the

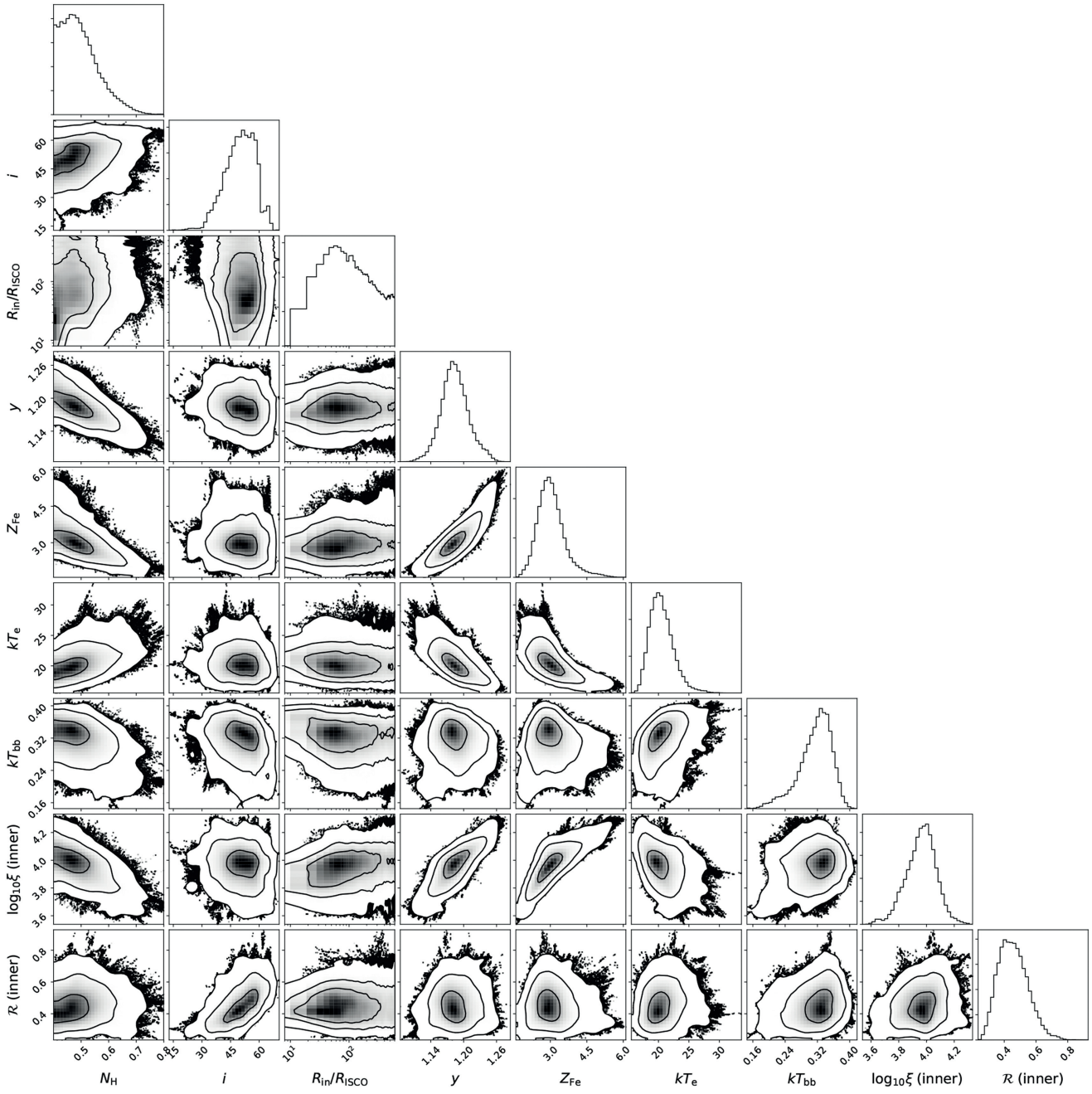

Figure 8. The posterior probability distributions (proportional to the relative frequency of the fitted models) showing correlations between pairs of the parameters of the `reflkerr` model (#6), obtained using the MCMC method. The inner, middle, and outer contours correspond to the 2D significance of $\sigma =$ 1, 2, 3, respectively, also shown by the degree of the darkness. The rightmost panels show the probability distributions for the individual parameters (with the normalization corresponding to the unity integrated probability). See Section 3.6 for discussion.

close reflector (#1, 3, 4, which appear more likely; see below) yield the disc inclinations close to face-on, which are only marginally consistent with the constraint on the binary inclination of $37^\circ \leq i_b \leq 78^\circ$ (Heida et al. 2017). Since those models imply the presence of a truncated disc with $R_{in} \gg R_{ISCO}$, the disc axis is likely to be aligned with the binary axis rather than the BH spin axis. We note that S17 argued that disc truncation in GX 339–4 requires a highly super-Eddington accretion rate. However, that argument is incorrect since it considers only the viscously generated soft seed photons but neglects the abundant soft photons from reprocessing of the hot-flow emission in the irradiated disc, as discussed in detail in Poutanen et al. (2018). Both the viscously generated photons and those due to re-emission of the irradiating flux absorbed in the disc form then a soft quasi-blackbody spectral component around the disc inner radius. This component corresponds to the blackbody seed photons in model 6.

Our overall best-fitting model (#6 in Table 1), with the lowest value of $\chi^2_\nu \approx 62/61$ and the by far highest Akaike likelihood, has a physical thermal-Comptonization primary continuum rather than a phenomenological e-folded power law. The best-fitting value of the truncation radius is several tens of R_{ISCO}, and $R_{in} \gtrsim 2R_{ISCO}$ within the 90 per cent confidence limits. The Fe abundance is the same for

both reflectors, and moderate, $Z_{\rm Fe} \approx 3$, and there is no absorption line at 7.2 keV required. This model also has the best-fitting inclination, $i \approx 49^{+34}_{-26^\circ}$, in good agreement with the constraint of Heida et al. (2017). We stress this is the only model among those considered that has a moderate Fe abundance, an inclination in agreement with that measured for the binary and the ionization of the distant reflection lower than that of the inner disc (which appears more likely; see below). On the other hand, only some, but not all, of those desired features appear in other models considered.

The primary continuum in this thermal-Comptonization model differs quite significantly from an e-folded power law at high energies. The difference between the two types of spectra is illustrated, e.g. in fig. 5(b) of Zdziarski et al. (2003). The Comptonization spectrum in that case has $kT_{\rm e} = 25$ keV, close to our best-fitting value of 20^{+3}_{-2} keV. We see in that figure that the Comptonization spectrum has an approximately single power-law shape up to ≈50 keV, and then it shows a sharp cut-off. On the other hand, an e-folded power law features a gradual attenuation, visible already at $E \ll E_{\rm cut}$. In the example shown in Zdziarski et al. (2003), an e-folded power law with $E_{\rm cut} = 150$ keV lies below the Comptonization spectrum already by $E \gtrsim 10$ keV. This effect explains the mismatch between the values of $kT_{\rm e}$ and $E_{\rm cut}$ that we found, with $E_{\rm cut} \gg kT_{\rm e}$ fitted here to the same spectrum at $E \leq 45$ keV.

For all of our models, we have also taken into account Comptonization of the reflected component. However, we have found this effect to be minor. In model 0 (which follows the assumptions of G15), the reflection fraction is $\mathcal{R} \approx 0.06$ and the fraction of the reflection photons scattered in the corona is $\lesssim 0.3$; such values rule out a corona above a disc extending to the ISCO. On the other hand, the relatively low values of $\mathcal{R}$ in our other models are consistent with truncation and the primary continuum originating partly in a corona and partly in a hot flow at $R < R_{\rm in}$ (Zdziarski et al. 1999). Our physical (and statistically best) thermal Comptonization model is also compatible with the energy balance constraint (see e.g. the recent study of Poutanen et al. 2018).

We have also investigated the effect of increasing the reflector density. Using the model of García et al. (2016) with $n_{\rm e} = 10^{19}$ cm^{-3} (#3 in Table 1), we have found an increase of both the truncation radius and the Fe abundance with respect to the corresponding model with an exponential cut-off and $n_{\rm e} = 10^{15}$ cm^{-3}. In particular, $Z_{\rm Fe}$ increased from ≈3 to ≈5 at the best fit.

The increase in $Z_{\rm Fe}$ we found is surprising, given the results of Tomsick et al. (2018). They have studied the effect of changing the reflector density for the case of a hard/intermediate spectrum of Cyg X-1 from *Suzaku* and *NuSTAR*. In the case of free Fe abundance, coronal geometry, and $n_{\rm e} = 10^{15}$ cm^{-3}, they obtained, using `relxill+xillver`, an extreme abundance of $Z_{\rm Fe} \sim 10$ and a very low disc inner radius of $R_{\rm in} = 1.33^{+0.03}_{-0.06} R_{\rm ISCO}$. Then, they used the reflection model `reflionx_hd` of Ross & Fabian (2007), which assumes $Z_{\rm Fe} = 1$ but allows for a free reflector density. The best fit in that case was obtained for $n_{\rm e} \approx 4 \times 10^{20}$ cm^{-3}, a much larger truncation radius, $R_{\rm in} \approx 7.3^{+4.6}_{-1.9} R_{\rm ISCO}$, and at a much lower value of χ^2 than in the previous case. Thus, the effects of allowing a high density in that case are an increase of the truncation radius and obtaining a good fit at the solar Fe abundance. While the former is in agreement with our finding, the latter effect is opposite. The reason for this disagreement is unclear; it may be related to a difference in the treatment of atomic processes in the reflecting/reprocessing medium between the `reflionx_hd` and `relxill` models.

We note that the actual characteristic value of $n_{\rm e}$ of the reflecting medium is uncertain. García et al. (2016) estimated it using the radiation-pressure dominated disc solution including the effect of coronal dissipation of Svensson & Zdziarski (1994). However, this density is averaged over the disc height, and it is close to that in the disc mid-plane. The corresponding Thomson optical depth of that solution is $\gg$10, and the reflecting surface layer has an optical depth of several and a much lower average density, given by the vertical hydrostatic equilibrium. Furthermore, the actual density is a function of both the radius and the depth within the disc.

A possible check on the self-consistency of an approximate solution is using the definition of ξ (equation 3). The irradiating flux in a coronal geometry can be expressed as the ratio of the luminosity to the emitting area, where the latter can be estimated as $x R_{\rm in}^2$, where the constant $x \sim 1$ expresses our (large) uncertainty about the area. In the case of Cyg X-1, $L \approx 1.8 \times 10^{37}$ erg s^{-1}, $R_{\rm in} \sim 10 R_{\rm g}$ (Tomsick et al. 2018) and $M \approx 15 {\rm M}_\odot$ (Orosz et al. 2011). The fitted ionization parameter was $\xi \approx 2000$ erg cm^{-2} s^{-1}, which implies $n_{\rm e} \approx (2/x) \times 10^{20}$ cm^{-3}, rather close to the density fitted in that work. In the case of our observation of GX 339–4 and model 3, $L \approx 2 \times 10^{38}$ erg s^{-1}, $\xi \approx 5000$ erg cm^{-2} s^{-1}, $R_{\rm in} \sim 50 R_{\rm ISCO}$, which yields $n_{\rm e} \approx (2/x) \times 10^{19}$ cm^{-3}. This implies that only model 3 can be considered as approximately self-consistent. However, given that the current version of the `xillverD` model allows for only for one option of the high-energy cut-off, we could not consider other options with it, in particular that with a thermal Comptonization primary spectrum.

In our analysis, we found that the data allow the ionization of the outer reflector to be higher than the inner one. This effect is due to the relatively modest relativistic effects in the inner reflector, which then allows for its interchange with the outer, static, one. Since $\xi \propto F_{\rm irr}/n_{\rm e}$, it is not a priori obvious that the surface layers of the outer disc are weakly ionized, given that they are irradiated by the strong X-ray emission from the central source, with the disc likely to be flared. Still, those solutions (#2, 5 in Table 1) appear less likely. We give them for the sake of the completeness of the presentation of our analysis results.

We stress that our most physically motivated case uses a one-zone thermal Comptonization model. In the case of the hard state of the BH binary Cyg X-1, Axelsson & Done (2018) found that the X-ray variability properties require the presence of three separate Comptonization components with different spectral slopes and temperatures. Yamada et al. (2013) obtained a similar conclusion from analysing the broad-band variability in Cyg X-1. Mahmoud & Done (2018a,b) modelled the spectral and timing properties of Cyg X-1, finding that rather complex models are required. In GX 339–4, observational evidence for two Comptonization zones has been recently reported from the full spectral-timing modelling of one *XMM–Newton* hard-state observation of the source (Mahmoud et al. 2018). Given that result and the overall similarity of the spectral and timing properties of Cyg X-1 and GX 339–4, our one-zone Comptonization modelling appears to be too simple to describe the actual accretion flow. However, since the *RXTE* data studied here cover the range of $\gtrsim$3 keV only, the second, soft, Comptonization component in the model of Mahmoud et al. (2018, see their fig. 4) contributes negligibly to the range fitted by us, and it does not affect the validity of our results.

We can compare our models to those that Basak & Zdziarski (2016) fitted to their EPIC-pn spectrum 7, in particular for their model 2(ii), which includes a static reflection component. That fit yields $R_{\rm in} = 19.5^{+15.0}_{-8.0} R_{\rm g}$ and $\Gamma \approx 1.67^{+0.02}_{-0.02}$, which are compatible with our results. The main differences are the high ionization of the outer static reflector, about the same as that of the inner one, and the Fe abundance, which they find to be about solar, with $Z_{\rm Fe} = 0.95^{+0.07}_{-0.06}$. Basak & Zdziarski (2016) also fitted a simultaneous PCA

spectrum, and noticed a mismatch between the EPIC-pn and PCA calibration in the Fe K region (see their fig. 8).

We note that a PCA spectrum of GX 339–4 in the hard spectral state has been used to test an alternative GR theory as well as to measure the BH spin (Wang-Ji et al. 2018a), assuming that the disc extends to the ISCO (see their table II). In light of our results, that test appears to be highly uncertain.

We stress that we have found a very good agreement between the models using the present version of `relxill` and `reflkerrExp`. They yield almost identical values of $R_{\rm in}$ and other parameters at very similar χ^2 (see Table 1).

Concluding, our spectral fitting results support the truncated disc paradigm for the hard state (Done et al. 2007), but allow the reflecting disc to extend to within about two ISCO radii within the 90 per cent confidence limit. Still, our results are based on a single spectrum (though with a very large count number of 10^7). Stronger constraints can be obtained while simultaneously fitting several data sets (as G15 did for their particular model).

ACKNOWLEDGEMENTS

We thank the referee for valuable comments, Javier García for discussions and explanations regarding the spectral analysis performed in G15, Jorge Casares and Jean-Pierre Lasota for discussions about disc inner radii in the quiescent state, Piotr Lubiński for discussion about the Akaike formalism, and Michael Parker for advice on the MCMC plotting. AGM acknowledges partial funding from NCN grant 2016/23/B/ST9/03123. This research has been supported in part by Polish National Science Centre grants 2013/10/M/ST9/00729, 2015/18/A/ST9/00746, 2016/21/B/ST9/02388, and 2016/21/P/ST9/04025.

REFERENCES

Akaike H., 1973, in Petrov B. N., Csaki F., eds, 2nd International Symposium on Information Theory. Akademiai Kiado, Budapest, p. 267
Akaike H., 1978, Ann. Inst. Stat. Math., 30, 9
Anders E., Grevesse N., 1989, Geochim. Cosmochim. Acta, 53, 197
Arnaud K. A., 1996, in Jacoby G. H., Barnes J., eds, ASP Conf. Ser. Vol. 101, Astronomical Data Analysis Software and Systems V. Astron. Soc. Pac., San Francisco, p. 17
Axelsson M., Done C., 2018, MNRAS, 480, 751
Basak R., Zdziarski A. A., 2016, MNRAS, 458, 2199
Begelman M. C., Armitage P. J., 2014, ApJ, 782, L18
Bernardini F., Russell D. M., Shaw A. W., Lewis F., Charles P. A., Koljonen K. I. I., Lasota J. P., Casares J., 2016, ApJ, 818, L5
Cao X., 2016, ApJ, 817, 71
Coriat M., Fender R. P., Dubus G., 2012, MNRAS, 424, 1991
Dauser T., Wilms J., Reynolds C. S., Brenneman L. W., 2010, MNRAS, 409, 1534
Dauser T., García J., Walton D. J., Eikmann W., Kallman T., McClintock J., Wilms J., 2016, A&A, 590, A76
De Marco B. et al., 2017, MNRAS, 471, 1475
De Marco B., Ponti G., Muñoz-Darias T., Nandra K., 2015, ApJ, 814, 50
Done C., Díaz-Trigo M., 2010, MNRAS, 407, 2287
Done C., Gierliński M., Kubota A., 2007, A&AR, 15, 1
Dubus G., Hameury J.-M., Lasota J.-P., 2001, A&A, 373, 251
Ebisawa K., Mitsuda K., Hanawa T., 1991, ApJ, 367, 213
Ebisawa K., Makino F., Mitsuda K., Belloni T., Cowley A. P., Schmidtke P. C., Treves A., 1993, ApJ, 403, 684
Esin A. A., McClintock J. E., Drake J. J., Garcia M. R., Haswell C. A., Hynes R. I., Muno M. P., 2001, ApJ, 555, 483
Foreman-Mackey D., 2016, JOSS, 1, 24
Foreman-Mackey D., Hogg D. W., Lang D., Goodman J., 2013, PASP, 125, 306
Fürst F. et al., 2015, ApJ, 808, 122
García J., Kallman T. R., 2010, ApJ, 718, 695
García J. et al., 2014a, ApJ, 782, 76
García J. A., McClintock J. E., Steiner J. F., Remillard R. A., Grinberg V., 2014b, ApJ, 794, 73
García J. A., Steiner J. F., McClintock J. E., Remillard R. A., Grinberg V., Dauser T., 2015, ApJ, 813, 84(G15)
García J. A., Fabian A. C., Kallman T. R., Dauser T., Parker M. L., McClintock J. E., Steiner J. F., Wilms J., 2016, MNRAS, 462, 751
García J. A., Kallman T. R., Bautista M., Mendoza C., Deprince J., Palmeri P., Quinet P., 2018, ASPC, 515, 282
Gierliński M., Done C., 2004, MNRAS, 347, 885
Goodman J., Weare J., 2010, CAMCS, 5, 65
Heida M., Jonker P. G., Torres M. A. P., Chiavassa A., 2017, ApJ, 846, 132
Jahoda K., Markwardt C. B., Radeva Y., Rots A. H., Stark M. J., Swank J. H., Strohmayer T. E., Zhang W., 2006, ApJS, 163, 401
Koen C., 2006, MNRAS, 365, 489
Kolehmainen M., Done C., Díaz Trigo M., 2014, MNRAS, 437, 316
Kylafis N. D., Belloni T. M., 2015, A&A, 574, A133
Lasota J.-P., Narayan R., Yi I., 1996, A&A, 314, 813
Liddle A. R., 2007, MNRAS, 377, L74
Lubiński P. et al., 2016, MNRAS, 458, 2454
Magdziarz P., Zdziarski A. A., 1995, MNRAS, 273, 837
Mahmoud R. D., Done C., 2018a, MNRAS, 473, 2084
Mahmoud R. D., Done C., 2018b, MNRAS, 480, 4040
Mahmoud R. D., Done C., De Marco B., 2018, MNRAS, preprint (arXiv: 1811.06911)
Markert T. H., Canizares C. R., Clark G. W., Lewin W. H. G., Schnopper H. W., Sprott G. F., 1973, ApJ, 184, L67
McClintock J. E. et al., 2001, ApJ, 555, 477
Menou K., Hameury J.-M., Lasota J.-P., Narayan R., 2000, MNRAS, 314, 498
Meyer-Hofmeister E., Liu B. F., Meyer F., 2005, A&A, 432, 181
Miller J. M. et al., 2008, ApJ, 679, L113
Miller J. M., Homan J., Steeghs D., Rupen M., Hunstead R. W., Wijnands R., Charles P. A., Fabian A. C., 2006, ApJ, 653, 525
Muñoz-Darias T., Coriat M., Plant D. S., Ponti G., Fender R. P., Dunn R. J. H., 2013, MNRAS, 432, 1330
Narayan R., Barret D., McClintock J. E., 1997, ApJ, 482, 448
Natalucci L. et al., 2014, ApJ, 780, 63
Niedźwiecki A., Szanecki M., Zdziarski A. A., 2019, MNRAS, 485, 2942
Novikov I. D., Thorne K. S., 1973, in DeWitt C., DeWitt B., eds, Black Holes. Gordon and Breach, Paris, p. 343
Orosz J. A., McClintock J. E., Aufdenberg J. P., Remillard R. A., Reid M. J., Narayan R., Gou L., 2011, ApJ, 742, 84
Parker M. L. et al., 2016, ApJ, 821, L6
Petrucci P.-O., Ferreira J., Henri G., Pelletier G., 2008, MNRAS, 385, L88
Petrucci P.-O., Cabanac C., Corbel S., Koerding E., Fender R., 2014, A&A, 564, A37
Plant D. S., Fender R. P., Ponti G., Muñoz-Darias T., Coriat M., 2015, A&A, 573, 120
Ponti G., Fender R. P., Begelman M. C., Dunn R. J. H., Neilsen J., Coriat M., 2012, MNRAS, 422, L11
Poutanen J., Svensson R., 1996, ApJ, 470, 249
Poutanen J., Veledina A., Zdziarski A. A., 2018, A&A, 614, 79
Reis R. C., Fabian A. C., Ross R. R., Miniutti G., Miller J. M., Reynolds C., 2008, MNRAS, 387, 1489
Reis R. C., Fabian A. C., Miller J. M., 2010, MNRAS, 402, 836
Ross R. R., Fabian A. C., 2007, MNRAS, 381, 1697
Shakura N. I., Sunyaev R. A., 1973, A&A, 24, 337
Steiner J. F. et al., 2011, MNRAS, 416, 941
Steiner J. F., García J. A., Eikmann W., McClintock J. E., Brenneman L. W., Dauser T., Fabian A. C., 2017, ApJ, 836, 119(S17)
Sugiura N., 1978, Commun. Stat. Theory Methods, 7, 13
Svensson R., Zdziarski A. A., 1994, ApJ, 436, 599

Tang Q.-W., 2018, Ap&SS, 363, 25
Tomsick J. A. et al., 2008, ApJ, 680, 593
Tomsick J. A. et al., 2018, ApJ, 855, 3
Tucker M. A. et al., 2018, ApJ, 867, L9
Wang-Ji J., Abdikamalov A. B., Ayzenberg D., Bambi C., Dauser T., Garcia J. A., Nampalliwar S., Steiner J. F., 2018a, preprint (arXiv:1806.00126)
Wang-Ji J. et al., 2018b, ApJ, 855, 61
Wilms J., Allen A., McCray R., 2000, ApJ, 542, 914
Yamada S., Makishima K., Done C., Torii S., Noda H., Sakurai S., 2013, PASJ, 65, 80
Zdziarski A. A., Johnson W. N., Magdziarz P., 1996, MNRAS, 283, 193
Zdziarski A. A., Poutanen J., Mikołajewska J., Gierliński M., Ebisawa K., Johnson W. N., 1998, MNRAS, 301, 435
Zdziarski A. A., Lubiński P., Smith D. A., 1999, MNRAS, 303, L11
Zdziarski A. A., Lubiński P., Gilfanov M., Revnivtsev M., 2003, MNRAS, 342, 355
Zdziarski A. A., Gierliński M., Mikołajewska J., Wardziński G., Smith D. M., Harmon B. A., Kitamoto S., 2004, MNRAS, 351, 791
Zimmerman E. R., Narayan R., McClintock J. E., Miller J. M., 2005, ApJ, 618, 832

This paper has been typeset from a TEX/LATEX file prepared by the author.

Chapter 4

Paper II

The Astrophysical Journal Letters, 909:L9 (9pp), 2021 March 1 https://doi.org/10.3847/2041-8213/abe7ef

Accretion Geometry in the Hard State of the Black Hole X-Ray Binary MAXI J1820+070

Andrzej A. Zdziarski[1], Marta A. Dziełak[1], Barbara De Marco[2], Michał Szanecki[3], and Andrzej Niedźwiecki[3]
[1] Nicolaus Copernicus Astronomical Center, Polish Academy of Sciences, Bartycka 18, PL-00-716 Warszawa, Poland; aaz@camk.edu.pl
[2] Departament de Física, EEBE, Universitat Politècnica de Catalunya, Av. Eduard Maristany 16, E-08019 Barcelona, Spain; barbara.de.marco@upc.edu
[3] Faculty of Physics and Applied Informatics, Łódź University, Pomorska 149/153, PL-90-236 Łódź, Poland; andrzej.niedzwiecki@uni.lodz.pl
Received 2021 January 6; revised 2021 February 16; accepted 2021 February 18; published 2021 March 3

Abstract

We study X-ray spectra from the outburst rise of the accreting black hole binary MAXI J1820+070. We find that models having the disk inclinations within those of either the binary or the jet imply significant changes of the accretion disk inner radius during the luminous part of the hard spectral state, with that radius changing from >100 to ∼10 gravitational radii. The main trend is a decrease with the decreasing spectral hardness. Our analysis requires the accretion flow to be structured, with at least two components with different spectral slopes. The harder component dominates the bolometric luminosity and produces strong, narrow, X-ray reflection features. The softer component is responsible for the underlying broader reflection features. The data are compatible with the harder component having a large scale height, located downstream the disk truncation radius, and reflecting mostly from remote parts of the disk. The softer component forms a corona above the disk up to some transition radius. Our findings can explain the changes of the characteristic variability timescales, found in other works, as being driven by the changes of the disk characteristic radii.

Unified Astronomy Thesaurus concepts: Accretion (14); Non-thermal radiation sources (1119); X-ray binary stars (1811); Low-mass x-ray binary stars (939)

1. Introduction

The standard model of accretion onto a black hole (BH) postulates the presence of a geometrically thin and optically thick disk (Shakura & Sunyaev 1973; Novikov & Thorne 1973). The disk is close to thermodynamic equilibrium and its emission can be approximated by a sum of local blackbodies with a color correction (Davis et al. 2005). In BH X-ray binaries (XRBs), this emission peaks in EF_E at $E \sim 1$ keV. On the other hand, BH XRBs in their hard spectral state have the peak of their EF_E emission at $E \sim 10^2$ keV (e.g., Done et al. 2007), which cannot be explained by that model. Observations of such spectra prompted development of models of hot accretion disks, where the electron temperature is $kT_e \sim 10^2$ keV (Shapiro et al. 1976; Narayan & Yi 1994; Abramowicz et al. 1995; Yuan & Narayan 2014). Those hot disks are postulated to exist below some radius, R_{in}, and be surrounded by standard accretion disks.

Then, alternative models explaining the hard X-ray spectra were developed. The thin disk can be covered by a hot corona (Galeev et al. 1979; Svensson & Zdziarski 1994). However, due to the cooling by the underlying disk (Haardt & Maraschi 1991; Poutanen et al. 2018), such coronae emit spectra with the photon index of $\Gamma \gtrsim 2$ (defined by $F_E \propto E^{1-\Gamma}$), which are too soft to explain the hard state, where $\Gamma < 2$ is observed. This can be resolved if the corona is outflowing (Beloborodov 1999). Another model postulates instead the presence of a static point-like source on the rotation axis of the BH, the so-called lamppost (Martocchia & Matt 1996). The lamppost, if it exists, should be in some way connected to the jet, present in the hard state, though theoretical explanations of it appear insufficient thus far (Yuan et al. 2019a, 2019b). The presence of jets in the hard state implies the presence of poloidal magnetic fields (Blandford & Znajek 1977; Blandford & Payne 1982; Liska et al. 2020), which can strongly modify the accretion solutions (e.g., Bisnovatyi-Kogan & Ruzmaikin 1974; Narayan et al. 2003; McKinney et al. 2012; Cao & Spruit 2013; Salvesen et al. 2016).

Deciding which model actually applies to the hard state requires strong observational constraints. In particular, an accurate determination of the geometry of the inner accretion flow is crucial. So far, such determinations have given conflicting results. A large number of papers claim the disk in the hard state extends to the immediate vicinity of the innermost stable circular orbit (ISCO), while other papers find the disk to be truncated (Bambi et al. 2021, and references therein). Here, we consider X-ray observations of the recent outburst of MAXI J1820+070, a bright transient BH XRB, with the goal of resolving this controversy. We use data from two very sensitive instruments, Nuclear Spectroscopic Telescope Array (NuSTAR; Harrison et al. 2013), and Neutron star Interior Composition ExploreR (NICER; Gendreau et al. 2016). We re-examine the findings by Kara et al. (2019, hereafter K19) and Buisson et al. (2019, hereafter B19) that the source evolution in the hard state is dominated by a corona vertical contraction accompanied by an approximate constancy of the surrounding disk.

MAXI J1820+070 was discovered in 2018, first in the optical range (Tucker et al. 2018), and five days later in X-rays (Kawamuro et al. 2018). It is a relatively nearby source; its most accurate distance estimate appears to be the radio-parallax determination (Atri et al. 2020), $d \approx 3.0 \pm 0.3$ kpc. This is consistent with determinations based on the Gaia Data Release 2 parallax, $d \approx 3.5^{+2.2}_{-1.0}$ kpc (Bailer-Jones et al. 2018; Gandhi et al. 2019; Atri et al. 2020). The inclination of the binary has been estimated as $66^\circ < i_b < 81^\circ$ (Torres et al. 2019, 2020), while that of the jet, as $i_j \approx 63 \pm 3^\circ$ (Atri et al. 2020). The BH mass is anticorrelated with i_b, $M \approx (5.95 \pm 0.22) M_\odot / \sin^3 i_b$ (Torres et al. 2020). The high inclination of this source is confirmed by the detection of X-ray dips (Kajava et al. 2019).

2. Observations and Data Reduction

We have chosen the spectra from the hard state during initial phases of the outburst that have contemporaneous NICER (0.3–12 keV) and NuSTAR (3–79 keV) coverage. The selected

Table 1
Observations of MAXI J1820+070 with NICER and NuSTAR in the Hard State During the Outburst Rise

Epoch	NICER Obs. ID	Start time End Time	Exposure (s)	NuSTAR Obs. ID	Start time End Time	Exposure A (s)	Exposure B (s)
1	1200120103	2018 Mar 13 T23:57:07 2018 Mar 14 T23:25:12	10691	90401309002	2018 Mar 14 T22:30:12 2018 Mar 15 T10:27:37	11769	11981
	1200120104	2018 Mar 15 T00:39:50 2018 Mar 15 T21:02:34	6652				
2	1200120106	2018 Mar 21 T09:21:01 2018 Mar 21 T23:16:08	4302	90401309006	2018 Mar 21 T07:18:35 2018 Mar 21 T16:10:13	4540	4540
3	1200120110	2018 Mar 24 T23:40:27 2018 Mar 25 T23:14:46	19083	90401309010	2018 Mar 24 T20:41:22 2018 Mar 25 T00:49:32	2660	2801
4	1200120130	2018 Apr 16 T01:54:03 2018 Apr 16 T23:50:30	6015	90401309013	2018 Apr 16 T22:51:45 2018 Apr 17 T01:23:09	1834	1934

spectral data for four epochs are detailed in Table 1. However, we present here only the results of spectral fits to the NuSTAR data. The reason for this is that NICER is primarily an instrument for timing studies, and its spectral calibration remains much less accurate than that of NuSTAR. In fact, fitting NICER data requires introducing artificial edges to account for sharp instrumental residuals (e.g., Wang et al. 2020a), which significantly affects the accuracy of the fits. In this Letter, we use the joint data to measure the bolometric flux and to show the form of the soft excess below 3 keV. We intend to perform spectral fits of the joint data with an improved NICER spectral calibration in a forthcoming paper.

We also show the count-rate versus hardness diagram for 2018 outburst using the NICER data in Figure 1. We see several phases. The initial rise in the hard state contains our epoch 1, as shown by the red circles. The rise reaches a local maximum, at which our epochs 2 and 3 are located. This was followed by a plateau, during which the count rate only slightly decreased during a decrease of the hardness, and our epoch 4 is located there. Subsequently, there was a rate decline associated with a hardening and a return along a similar path. This was followed by a transition to the soft state, after which the source returned to the hard state but at much lower fluxes. The four NuSTAR spectra considered by us were studied by B19, where they are denoted as epoch 1, the second parts of epochs 2 and 3, and the first part of epoch 5. Also, the NuSTAR data of our epoch 3 were studied in Chakraborty et al. (2020). Timing properties of the NICER observations of our epochs 2 and 4 were studied in K19. The NICER data of epoch 1 are studied in Dziełak et al. (2021). The data from two observations, one on the day preceding and one on the day following that NuSTAR observation, are added. A comprehensive study of the timing properties of all of the NICER observations from the phases of the outburst up to the transition to the soft state is given in De Marco et al. (2021).

The NuSTAR data were reduced with HEASOFT v.6.25, the `NUSTARDAS` pipeline v.1.8.0, and `CALDB` v.20200912. To filter passages through the South Atlantic Anomaly, we set `saamode=strict` and `tentacle=yes`. As recommended by the NuSTAR team, we use `STATUS==b0000xxx00xxxx000` to avoid source photons being spuriously flagged as `test`. The source region is a 60″ circle centered on the peak brightness. The background is extracted from a 60″ circle in an area with the lowest apparent contribution from sources. However, the background is negligible. We group the data to signal-to-noise ratio (S/N) $\geqslant 50$, but to less at >69 keV so to utilize the full $\leqslant$79 keV band.

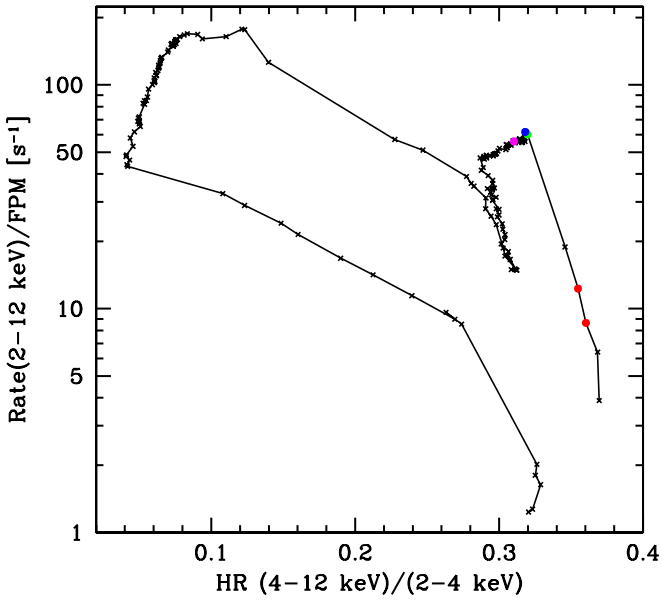

Figure 1. NICER count rate per a Focal Plane Module (FPM) in the 2–12 keV range vs. the hardness given by the count-rate ratio of 4–12 to 2–4 keV for the main part of the outburst, between 2018 March 12 T13:51:20 (MJD 58189.577; the rightmost point) and 2018 October 13 T02:37:28 (MJD 58404.109; the lowest point). The lines connect observations adjacent in time. The NuSTAR observations during our epochs 1, 2, 3, 4 are contemporaneous to the NICER observations indicated by the red, green, blue, and magenta circles, respectively.

The NICER data were reduced using the `NICERDAS` tools in HEASOFT v.6.28 and `CALDB` v.20200727. We applied the standard screening criteria (Stevens et al. 2018) and checked for periods of high particle background ($>2\,s^{-1}$) by using the 13–15 keV light curves, where the source contribution is negligible (Ludlam et al. 2018). We removed the Focal Plane Modules (FPMs) 14 and 34, which occasionally display increased noise, and screened for ones showing anomalous behavior.

3. Fits to the X-Ray Spectra of MAXI J1820+070

We study the spectra with the X-ray fitting package XSPEC (Arnaud 1996). The reported fit uncertainties are for 90% confidence, $\Delta\chi^2 \approx 2.71$. Residual differences between the calibration of the NuSTAR FPMA and FPMB detectors are accounted for by the model `jscrab` (Steiner et al. 2010), which multiplies the spectrum by a power law with an index difference, $\Delta\Gamma$ (defined by the differential photon number flux of $\propto E^{-\Gamma}$) and a normalization. We account for the interstellar

medium (ISM) absorption using the tbabs model (Wilms et al. 2000) using the elemental abundances of Anders & Grevesse (1989).

We use models with thermal Comptonization spectra incident on an accretion disk, taking into account atomic processes and relativistic effects, as implemented in two families of spectral codes, relxillCp, xillverCp (v. 1.4.0; García & Kallman 2010; Dauser et al. 2016) and reflkerr (Niedźwiecki et al. 2019). We assume a rotating BH with the dimensionless spin of $a_* = 0.998$, for which $R_{\rm ISCO} \approx 1.237 R_{\rm g}$, where $R_{\rm g} \equiv GM/c^2$. At $R \gg R_{\rm ISCO}$, the metric is virtually independent of a_*.

We begin with studying epoch 1. We first fit the NuSTAR spectra following B19, whose important conclusion was that no model with a single primary (Comptonization) component can fit the data. Their best model consists of a lamppost with two parts with the same incident spectra but at different heights, disk reflection normalized at that geometry, and a disk blackbody. The small differences of our analysis with respect to that work is that we use jscrab instead of allowing independent disk blackbody parameters for the two FPMA and FPMB. With the current calibration, $\Delta\Gamma$ of the FPMB with respect to FMBA is very small, $\approx$+0.01, and their differences at the lowest energies are similar to those typical for the entire range. Also, we include the ISM absorption, with $N_{\rm H}$ kept constant at 1.4×10^{21} cm^{-2} (Kajava et al. 2019; Dziełak et al. 2021). Thus, our model is jscrab$*$ tbabs (diskbb+relxilllpCp$_1$+relxilllpCp$_2$), where the two relxilllpCp terms give the two parts of the lamppost primary source. Finally, B19 ignored the 11–12 and 23–28 keV energy ranges, where there were some sharp instrumental features. We include those ranges since such features are no longer present.

We confirm the result of B19, with some small differences attributable to the updated NuSTAR calibration and a newer version of relxilllpCp. We find a good fit with an extremely relativistic configuration, at $R_{\rm in} \approx 2.1^{+1.3}_{-0.5} R_{\rm g}$, $H_1 \approx 3.0^{+0.9}_{-0.1} R_{\rm g}$, $H_2 \approx 70^{+40}_{-30} R_{\rm g}$, a very hard spectral index, $\Gamma \approx 1.32^{+0.02}_{-0.01}$, at $\chi^2_\nu \approx 806/744$. Similar to B19, who found $i \approx 30^{+4}_{-5}{}^\circ$, we obtain $i \approx 32^{+3}_{-5}{}^\circ$. Given the current observational evidence for a high inclination (Section 1), this represents a major problem for the applicability of this model (developed before the constraints on the inclination were published) to MAXI J1820+070. Another problem for this spectral solution is that the Fe abundance is very high, $Z_{\rm Fe} \approx 6.1^{+0.6}_{-0.2}$ ($4.0^{+0.9}_{-0.7}$ in B19), which is unlikely given the presence of a weakly-evolved low-mass donor (Torres et al. 2020).

We have thus searched for alternative solutions at higher inclinations. We have indeed found a second minimum at a high inclination, though at somewhat higher $\chi^2_\nu \approx 820/744$. The inclination is now fully consistent with the observational constraints, $i \approx 69^{+1}_{-9}{}^\circ$. On the other hand, the disk is highly truncated, $R_{\rm in} \approx 77^{+200}_{-39} R_{\rm g}$. The height of the lower lamppost is $H_1 \approx 7.2^{+1.2}_{-5.2} R_{\rm g}$, that of the upper one is very large, $H_2 \approx 500 R_{\rm g}$ (which is the largest value allowed by the adopted model), and $\Gamma \approx 1.50^{+0.01}_{-0.05}$. The observed emission is dominated by the upper lamppost. We have looked at possible degeneracies and significant correlations between the fitted parameters, but found none.

The model spectra of the two solutions are compared in Figure 2. We see that while the two curves are virtually indistinguishable in the fitted 3–78 keV range, they make very different predictions at $\gtrsim$100 keV. The high-$R_{\rm in}$ fit predicts a gradual high-energy cutoff corresponding to the fitted electron temperature of $kT_{\rm e} \approx 58^{+3}_{-25}$ keV. On the other hand, the low-$R_{\rm in}$ fit predicts a pronounced high-energy hump peaking at 0.4–0.5 MeV, due to the high fitted $kT_{\rm e} \approx 360^{+40}_{-80}$ keV (400^{+0}_{-300} keV in B19). The two spectra can be compared to the spectrum measured by the Spectrometer on INTEGRAL (SPI) about a day after the end of the NuSTAR observation, shown as the spectrum R1 in Figure 12 of Roques & Jourdain (2019). We plot that spectrum in Figure 2, multiplied by a factor of 0.52, which accounts for the flux increase during the time between the NuSTAR and SPI observations, and a calibration difference, with the SPI fluxes higher by a factor of $\approx$1.3 than those of NuSTAR for simultaneous observations. The error bars are not shown; they are of the order of the scatter among the points. We see that the SPI spectrum agrees well with that of NuSTAR in the overlapping 20–78 keV range. It also approximately agrees at higher energies with the high-$R_{\rm in}$ model, but it strongly disagrees with the low-$R_{\rm in}$ one. This provides one more argument against its physical reality. We have also compared the residuals of the two fits. We found them to be very similar, with no systematic differences (which is compatible with the close similarity of the shape of the best-fit models, shown in Figure 2).

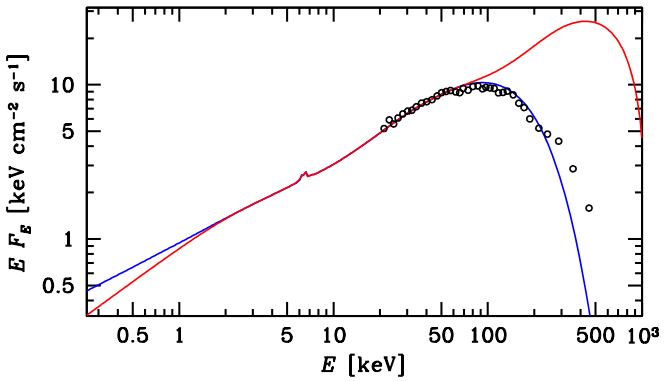

Figure 2. Comparison of the unabsorbed model spectra for the two fits of the double-lamppost + disk blackbody model to the epoch 1 data. The red and blue curves show the low and high $R_{\rm in}$ solutions, respectively. The two curves are virtually indistinguishable in the fitted 3–78 keV range. The black circles show the measurements taken by the SPI detector on board INTEGRAL a day after the end of the NuSTAR observation (Roques & Jourdain 2019), normalized to the NuSTAR spectrum. We see that while it approximately agrees with the high-$R_{\rm in}$ model spectrum at $E > 78$ keV, it strongly disagrees with the low-$R_{\rm in}$ one.

We have also found that the two solutions are separated by a very high barrier in χ^2, as shown in Figure 3. The barrier reaches $\Delta\chi^2 \approx +900$ around $R_{\rm in} \approx 17 R_{\rm g}$. This actually prevents finding the low-$R_{\rm in}$ solution when starting from the high-$R_{\rm in}$ one, using either steppar in XSPEC, or the Monte Carlo Markov Chain method. We have also looked for low-$R_{\rm in}$ counterparts of other spectral solutions presented below, and found they are generally present, but their inclinations are also at $i \sim 30^\circ$.

The analyses of the binary parameters (Torres et al. 2019, 2020) and of the jet (Atri et al. 2020), and the presence of X-ray dips (Kajava et al. 2019; see a discussion in Frank et al. 2002) all show at very high confidence that the source inclination is high. The inner disk can be aligned either with the binary plane or the normal to the BH rotation axis, but both are inclined at $\gtrsim 60^\circ$. An outer part of the disk could be warped (e.g., Pringle 1997), but not the disk in an immediate vicinity of

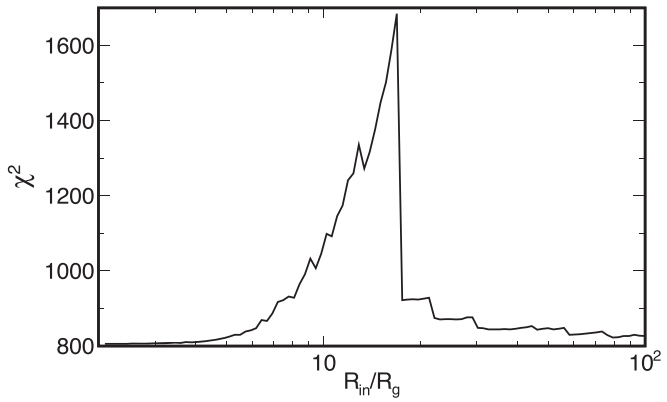

Figure 3. Dependence of χ^2 on the disk inner radius, R_{in}. We see two minima, at low and high values of R_{in}, separated by a very high barrier in χ^2, with $\Delta\chi^2 \approx +900$ around $R_{in} \approx 17R_g$.

the ISCO. Therefore, while the $i \sim 30°$ spectral solution is statistically better than the $i \sim 60$–$70°$ one, it can be considered only as a phenomenological description of the spectrum, but not as a representation of the actual geometry of the accretion flow. Therefore, in the remainder of this study, we consider only high-i solutions.

Furthermore, the disk blackbody component, included in this model in order to account for the soft excess present in the $\geqslant 3$ keV data, is also phenomenological, and its inner temperature, $kT_{in} \approx 1.4^{+0.1}_{-0.2}$ keV, is significantly higher than that seen in the NICER data, which is $kT_{in} \sim 0.2$ keV (Wang et al. 2020b; Dziełak et al. 2021), which component contributes negligibly at energies >3 keV. On the other hand, in the framework of such a composite lamppost, the two incident spectra should have different spectral indices. These spectra are most likely from the Comptonization process, which implies that the spectral slope at $E \ll kT_e$ is a sensitive function of the flux of the incident seed soft photons from the surrounding accretion disk, and of the magnetic field strength if the cyclo-synchrotron process is important. Both strongly depend on the height of the X-ray source in the assumed geometry. Furthermore, the large fitted R_{in} suggests the possibility that the region downstream of it contains a hot plasma, and the adopted lamppost model is a proxy to a more complex physical situation. Therefore, we allow the reflection strengths to be free parameters.

Thus, we consider a model with the two incident spectra having different parameters. In this case, the presence of a disk blackbody is not required. We have found a similar $\chi^2_\nu \approx 820/743$, and $R_{in} \approx 107^{+172}_{-95} R_g$, $i \approx 61^{+9}_{-1}°$, $Z_{Fe} \approx 2.0^{+0.2}_{-0.5}$. The lower lamppost component is soft, with $\Gamma_1 \approx 1.80^{+0.06}_{-0.27}$, at a low height, $H_1 \approx 2.5^{+0.1}_{-0.4} R_g$, and the part of the disk giving rise to most of the reflection is strongly ionized, $\log_{10}\xi \approx 4.3^{+0.2}_{-0.1}$ (where the ionization parameter, ξ is in units of erg cm s^{-1}). The upper lamppost has $\Gamma_2 \approx 1.44^{+0.01}_{-0.01}$, $H_2 \approx 500R_g$, and its reflecting part of the disk is weakly ionized, $\log_{10}\xi \approx 0.3^{+1.5}_{-0.3}$ (where the lower limit corresponds to the minimum allowed in the model). We find that the upper lamppost dominates both the bolometric flux and the observed, relatively narrow, Fe K complex. Given the flux dominance and the NuSTAR energy coverage limited to <78 keV, we assume kT_e to be the same for both components, and find it $\approx 47^{+8}_{-8}$ keV.

These results bring about the issue of the physical nature of the spectral components. Likely, the region at $R < R_{in}$ is filled by a hot plasma, which irradiates the truncated disk. However,

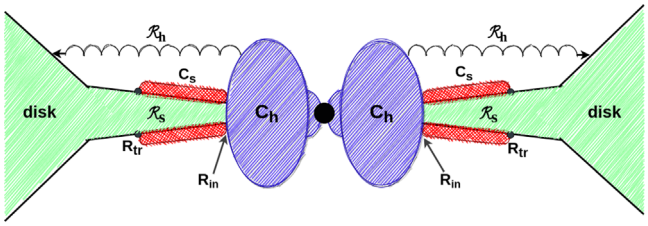

Figure 4. Schematic representation of the proposed geometry for the spectral fits shown below in Figure 5. The disk is truncated at R_{in}, and covered by a Comptonizing coronal plasma, C_s, from R_{in} to R_{tr}. Interior to R_{in}, there is a hot accretion flow with a relatively large scale height, C_h. Comptonization in C_s and C_h gives rise to the observed softer and harder, respectively, incident spectral components. The emission of C_h is reflected from the flared disk beyond R_{tr}, marked as $\mathcal{R}_h$. The emission of the coronal plasma, C_s, is reflected from the disk beneath it, marked as $\mathcal{R}_s$.

the data clearly require two separate plasma clouds. The one radiating most of the luminosity also dominates the observed reflection features, which are almost non-relativistic. The presence of such features in the data implies the reflection from remote parts of the disk, which drives the large upper lamppost height, $\sim 500R_g$. Indeed, a similar fit can be obtained when replacing the upper lamppost by a static reflection component, `xillverCp`.

Following these results, we have developed an accretion model with two hot plasma flows and an accretion disk, shown in Figure 4. The disk is truncated at R_{in}, and significantly flared at large radii (as follows from the standard accretion models, e.g., Shakura & Sunyaev 1973) and/or warped. The disk is covered by a hot Comptonizing corona, C_s, from R_{in} to R_{tr}, which is responsible for the observed softer incident spectral component. Its emission is reflected from the underlying disk, which is strongly ionized and which reflection is partly attenuated by the subsequent scattering in the plasma. (For the sake of simplicity, we assumed that this only results in a reduction of the observed reflection strength.) Interior to R_{in}, there is also a hot accretion flow, C_h, which Comptonization gives rise to the observed harder incident component. Since the disk is covered by the hot corona up to R_{tr}, this emission is reflected predominantly by the bare disk beyond it. That region is much less ionized given the large distance between the plasma and the reflector.

However, we note that the above scenario requires $R_{tr} > R_{in}$, i.e., it forces the inner radius of the hard reflection component to be larger than that for the soft one. In order to test the validity of this assumption, we also consider an alternative model allowing for an overlap of the reflection regions. This can correspond to the hot corona between R_{in} and R_{tr} being patchy. In this version, we fit two values of the inner radii of the reflecting region, $R_{in,s}$ and $R_{in,h}$, without imposing any a priori conditions on them.

We implement the two variants of this geometry using the `reflkerr` coronal reflection code of Niedźwiecki et al. (2019), which has a significantly improved treatment of Comptonization with respect to `relxill`. As in `relxill`, it approximates the reflection assuming a power-law disk irradiation profile; here we assume the standard profile of $\propto R^{-3}$, which follows the disk viscous dissipation at $R \gg R_{ISCO}$. The used XSPEC form is given in Table 2. As previously, we assume kT_e to be the same for both components; allowing them to be different results only in a tiny reduction of χ^2. The temperature of blackbody photons serving as seeds for Comptonization is

Table 2
The Results of Spectral Fitting for Our Two-component Coronal Model, `jscrab*tbabs(reflkerr_s+reflkerr_h)`, to the NuSTAR Data, and for Two Options, Separate and Overlapping Reflection Regions

Component	Parameter	Epoch 1	Epoch 2	Epoch 3	Epoch 4
ISM absorption	$N_{\rm H}$ [10^{21}] cm^{-2}		1.4f		
		Separate Reflection Regions			
Joint constraints	i [°]	63^{+2}_{-2}	66^{+1}_{-1}	59^{+7}_{-10}	71^{+1}_{-9}
	$Z_{\rm Fe}$	$1.3^{+0.1}_{-0.1}$	$1.2^{+0.2}_{-0.1}$	$1.4^{+0.2}_{-0.3}$	$1.2^{+0.2}_{-0.3}$
	$kT_{\rm e}$ [keV]	44^{+3}_{-1}	27^{+2}_{-2}	24^{+1}_{-1}	32^{+4}_{-4}
Soft Comptonization and reflection	$y_{\rm s}$	$0.98^{-0.05}_{+0.07}$	$1.11^{+0.02}_{-0.03}$	$1.17^{+0.02}_{-0.02}$	$0.81^{-0.09}_{+0.09}$
	$R_{\rm in}$ [$R_{\rm g}$]	77^{+335}_{-24}	16^{+6}_{-7}	127^{+71}_{-61}	$10.1^{+4.7}_{-3.6}$
	$\mathcal{R}_{\rm s}$	$0.61^{-0.32}_{+0.13}$	$0.57^{+0.18}_{-0.13}$	$0.37^{+0.09}_{-0.17}$	$0.86^{+0.27}_{-0.38}$
	$\log_{10}\xi_{\rm s}$	$3.74^{+0.55}_{-0.53}$	$3.48^{+0.10}_{-0.10}$	$3.49^{+0.12}_{-0.12}$	$3.30^{+0.09}_{-0.22}$
	$N_{\rm s}$	0.18	2.57	3.47	1.70
	$F_{\rm s,inc}$ [10^{-8} erg cm^{-2} s]	0.23	4.1	5.9	1.5
Hard Comptonization and reflection	$y_{\rm h}$	$1.78^{+0.01}_{-0.02}$	$1.71^{+0.04}_{-0.06}$	$1.89^{+0.07}_{-0.09}$	$1.41^{+0.04}_{-0.07}$
	ΔR [$R_{\rm g}$]	230^{+120}_{-220}	170^{+60}_{-50}	$\leqslant 110$	57^{+35}_{-19}
	$R_{\rm tr}$ [$R_{\rm g}$]		$= R_{\rm in} + \Delta R$		
	$R_{\rm out}$ [$R_{\rm g}$]		10^3f		
	$\mathcal{R}_{\rm h}$	$0.32^{+0.02}_{-0.01}$	$0.62^{+0.21}_{-0.06}$	$0.62^{+0.38}_{-0.15}$	$0.48^{+0.38}_{-0.03}$
	$\log_{10}\xi_{\rm h}$	$0.30^{+0.02}_{-0.06}$	$0.53^{+1.39}_{-0.53}$	$0.10^{+1.60}_{-0.10}$	$0.46^{+1.54}_{-0.46}$
	$N_{\rm h}$	0.80	1.60	0.97	3.30
	$F_{\rm h,inc}$ [10^{-8} erg cm^{-2} s]	3.8	6.0	4.1	9.2
	χ^2_ν	818/744	1040/879	704/699	703/543
		Overlapping Reflection Regions			
Joint constraints	i [°]	63^{+2}_{-2}	66^{+1}_{-1}	63^{+3}_{-3}	71^{+1}_{-9}
	$Z_{\rm Fe}$	$1.4^{+0.2}_{-0.1}$	$1.1^{+0.2}_{-0.1}$	$1.3^{+0.3}_{-0.2}$	$1.2^{+0.3}_{-0.2}$
	$kT_{\rm e}$ [keV]	44^{+3}_{-6}	26^{+1}_{-2}	24^{+1}_{-1}	31^{+4}_{-3}
Soft Comptonization and reflection	$y_{\rm s}$	$0.98^{-0.10}_{+0.05}$	$1.04^{+0.03}_{-0.02}$	$1.13^{+0.02}_{-0.02}$	$0.81^{+0.09}_{-0.07}$
	$R_{\rm in,s}$ [$R_{\rm g}$]	60^{+870}_{-52}	14^{+6}_{-5}	95^{+105}_{-56}	$9.6^{+4.7}_{-2.5}$
	$R_{\rm out,s}$ [$R_{\rm g}$]		10^3f		
	$\mathcal{R}_{\rm s}$	$0.56^{-0.15}_{+0.19}$	$0.75^{+0.61}_{-0.09}$	$0.44^{+0.15}_{-0.11}$	$0.82^{+26}_{-0.30}$
	$\log_{10}\xi_{\rm s}$	$3.74^{+0.30}_{-0.56}$	$3.46^{+0.07}_{-0.07}$	$3.44^{+0.26}_{-0.05}$	$3.28^{+0.10}_{-0.19}$
	$N_{\rm s}$	0.18	2.02	3.27	1.78
	$F_{\rm s,inc}$ [10^{-8} erg cm^{-2} s]	0.23	2.8	5.2	1.6
Hard Comptonization and reflection	$y_{\rm h}$	$1.78^{+0.03}_{-0.01}$	$1.65^{+0.05}_{-0.14}$	$1.86^{+0.06}_{-0.09}$	$1.43^{+0.05}_{-0.08}$
	$R_{\rm in,h}$ [$R_{\rm g}$]	290^{+110}_{-80}	170^{+100}_{-40}	130^{+100}_{-40}	66^{+23}_{-17}
	$R_{\rm out,h}$ [$R_{\rm g}$]		10^3f		
	$\mathcal{R}_{\rm h}$	$0.32^{+0.01}_{-0.01}$	$0.50^{+0.09}_{-0.05}$	$0.56^{+1.22}_{-0.03}$	$0.47^{+0.43}_{-0.06}$
	$\log_{10}\xi_{\rm h}$	$0.30^{+0.02}_{-0.03}$	$0.43^{+1.46}_{-0.05}$	$0.10^{+1.68}_{-0.09}$	$0.42^{+1.42}_{-0.42}$
	$N_{\rm h}$	0.80	2.12	1.19	3.20
	$F_{\rm h,inc}$ [10^{-8} erg cm^{-2} s]	3.8	7.5	5.1	8.9
	χ^2_ν	818/744	1041/879	704/699	703/543
	$F_{\rm bol}$ [10^{-8} erg cm^{-2} s]	5.0	15	15	14
	$L/L_{\rm E}$	0.046	0.14	0.14	0.13

Note. See Section 3 for details. $kT_{\rm e}$ and $kT_{\rm bb} = 0.2$ keV are assumed to be the same for both Comptonizing coronae, N is the flux density at 1 keV in the observer's frame, and "f" denotes a fixed parameter. $F_{\rm (s,h),inc}$ give the (unabsorbed) bolometric Comptonization fluxes of the respective component, $F_{\rm bol}$ is an estimate of the total bolometric flux based on both the NICER and NuSTAR data (normalized to the NuSTAR FPMA), and $L/L_{\rm E}$ is the Eddington ratio for $d = 3$ kpc, $M = 8M_\odot$ and $X = 0.7$ [$L_{\rm E} = 1.47(M/M_\odot) \times 10^{38}$ erg s^{-1}].

taken as $kT_{\rm bb} = 0.2$ keV (compatible with the NICER data; Wang et al. 2020b; Dziełak et al. 2021). The slope of each Comptonization component is parametrized by the Compton parameter, $y \equiv 4\tau_{\rm T} kT_{\rm e}/m_{\rm e}c^2$, where $\tau_{\rm T}$ is the Thomson optical depth of the plasma. We note, however, that the reported values of y are somewhat overestimated due the Comptonization model being based on iterative scattering (Poutanen & Svensson 1996). The reflection fraction, $\mathcal{R}$, is defined in `reflkerr` as the ratio of the flux irradiating the disk to that emitted outside in a local frame.

We find that both options of this model yield $\chi^2_\nu \approx 818/744$ and the parameters given in Table 2. The two sets of the parameters differ only slightly. In the option with overlapping reflection regions, the inner radius of the soft component is lower than that for the hard component at the best fits for all four data sets, confirming the assumption of $R_{\rm tr} > R_{\rm in}$ done in the option with separate reflection regions (Figure 4). In the latter, the value of $\Delta R \equiv R_{\rm tr} - R_{\rm in}$ is primarily driven by the hard reflection, as it determines $R_{\rm tr}$, while the soft reflection is relatively insensitive to its outer radius given the used irradiation profile $\propto R^{-3}$. The unfolded spectra and data/model ratios for the case of separate reflection regions are shown in Figure 5. Both cases have the inclination within the observational constraints and the Fe abundance very close to solar. As expected if these fits indeed correspond to the geometry close to that shown in Figure 4, the harder component dominates the bolometric flux, and the reflector of the softer component is much more ionized than that of the harder one.

We have also tested a number of other models and found the truncation radius to be large and the reflection features are only weakly relativistic for all of those satisfying the observational constraints on the inclination. Thus, we have a robust conclusion that, at least in this BH XRB, the truncation radius at the luminosity of $\sim 5\% L_{\rm E}$ is $\sim 10^2 R_{\rm g}$.

We then study the data for epochs 2–4. We fit the NuSTAR spectra with the two versions of the double-corona `reflkerr` model. We find good fits at high inclinations, as shown in Table 2 and Figure 5. The shapes of the four spectra are compared in Figure 6. The disk truncation radius is relatively small for epoch 2, $R_{\rm in} \sim 20 R_{\rm g}$ and even lower for 4, $R_{\rm in} \sim 10 R_{\rm g}$, while $R_{\rm in}$ during epoch 3 is similar to that of the epoch 1. In all cases, $R_{\rm in}$ is significantly larger than $R_{\rm ISCO}$. In epoch 3, we also find a high relative amplitude of the softer Comptonization component. We have no explanation for this feature of epoch 3; it may be due some fluctuation of the source parameters. We see a monotonous decrease of $R_{\rm tr}$ over all four epochs. Our values of $R_{\rm in}$ can be compared with those obtained by Wang et al. (2020b) by modeling the NICER data by a disk blackbody and a power law. They obtained the disk inner radii of $\approx (4.5\text{–}6.5) \times 10^7$ cm during the period analyzed here. At $8 M_\odot$, this corresponds to $\sim 40\text{–}50 R_{\rm g}$, in an overall agreement with our values, and independently ruling out solutions with $R_{\rm in}$ close to the ISCO.

While the fits show variability of the characteristic disk radii, the fitted i and $Z_{\rm Fe}$ are compatible with constant, as expected. In fact, we may expect some variability of i due to precession or warping. Also, the viewing angle of the disk below and above $R_{\rm tr}$ may be different, as shown in Figure 4. We neglect this complication as not to overfit the data. The values of our fitted inclination agree with the jet and binary observations, unlike those of B19 and Chakraborty et al. (2020). The Fe abundance is compatible with $Z_{\rm Fe} \approx 1.2\text{–}1.3$. Such a closeness to unity is likely for this XRB, which has a low-mass donor (Torres et al. 2020), in which substantial Fe synthesis is not expected during the evolution. On the other hand, the values of $Z_{\rm Fe}$ found by B19 and Chakraborty et al. (2020) were within the range of 4–10 at their best fits.

We then briefly consider the NICER data. We fit them at the range 3–10 keV, to test their consistency with the NuSTAR data. We find a generally good agreement, even in the relative normalization, which values are close to unity, and joint fits

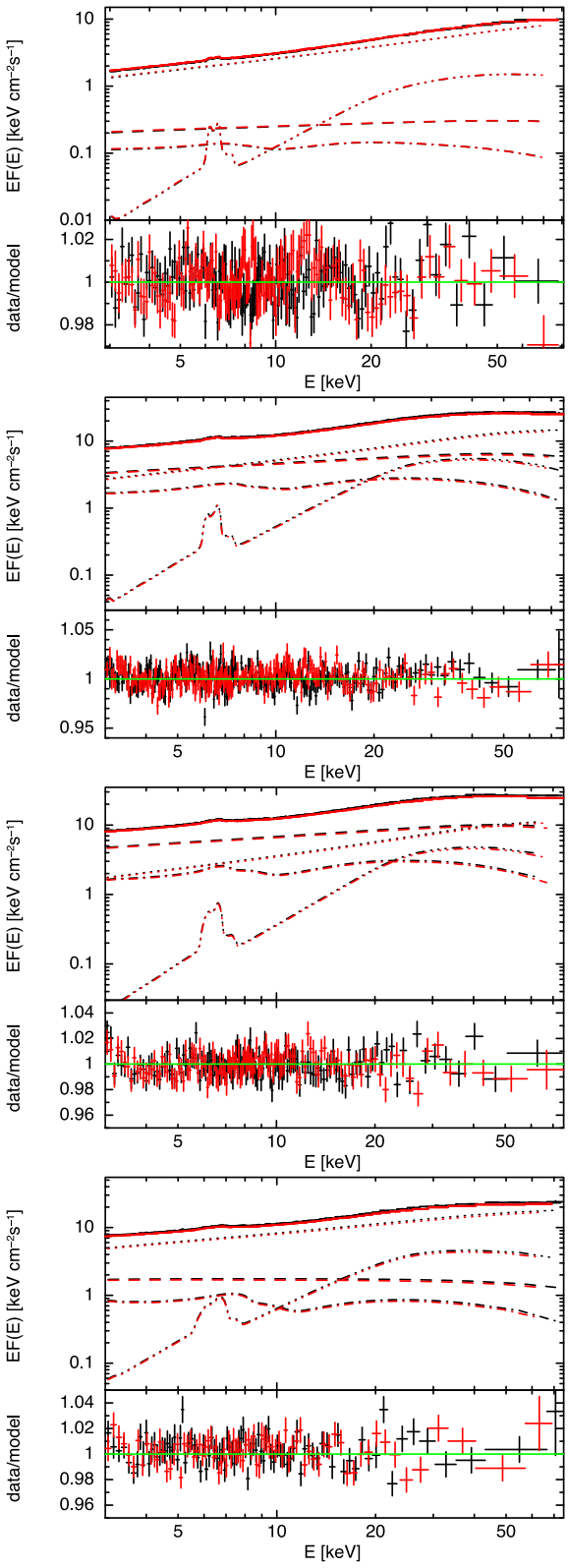

Figure 5. NuSTAR unfolded spectra and data-to-model ratios of the epochs 1–4 (from top to bottom) fitted in the 3–78 keV range with the two-component coronal model (Table 2). The dotted and dashed curves on the top panel correspond to the direct emission of the harder and softer corona, respectively, and the triple-dotted–dashed and dotted–dashed curves correspond to the reflection of harder and softer direct emission, respectively. Hereafter, the black and red symbols correspond to the FPMA and FPMB, respectively, and the plotted spectra are rebinned to $S/N \geqslant 100$.

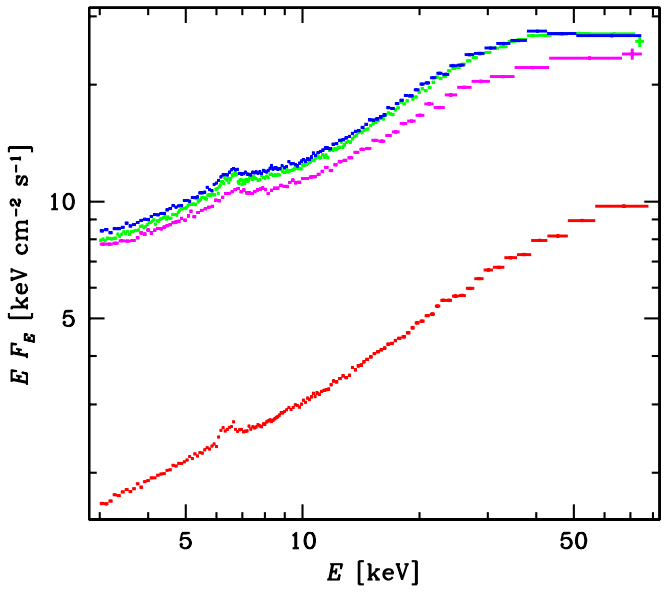

Figure 6. Spectra of the four studied observations unfolded with the two-component coronal model with separate reflection regions (Table 2). For clarity, only the spectra from the FPMA detector are shown. The spectra of the epochs 1, 2, 3, 4 are shown in the red, green, blue, and magenta color, respectively.

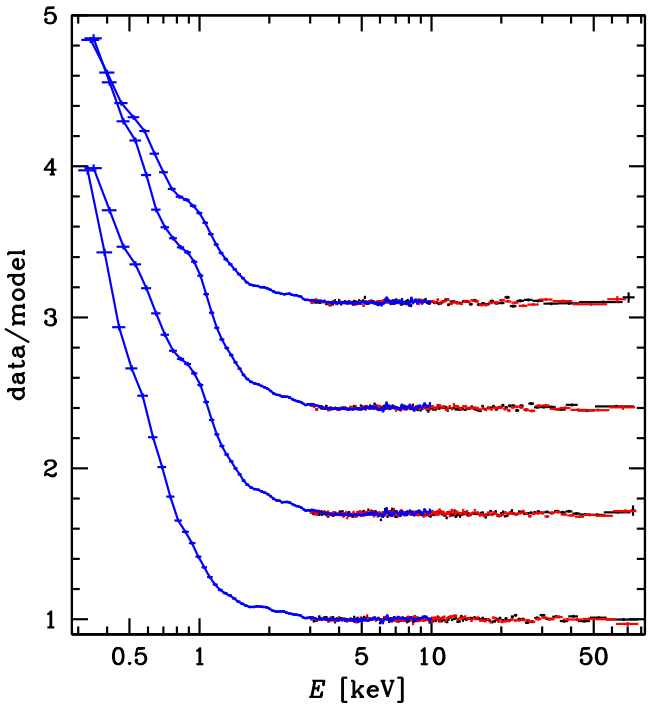

Figure 7. Data/model ratios for the two-component coronal model with separate reflection regions fitted to the NuSTAR (black and red symbols) and NICER (blue symbols) 3–10 keV data for epochs 1–4 (from bottom to top). For clarity of display, the profiles for epochs 2, 3, and 4 have been offset by +0.7, +1.4, and +2.1, respectively. We also show the NICER data at <3 keV, which show strong and complex soft excesses.

with the double-corona model give parameters similar to those in Table 2. However, the NICER data at <3 keV show strong soft excesses, as shown in Figure 7. These excesses are not compatible with the presence of a disk blackbody alone, and imply a further complexity of the accretion flow (see Dziełak et al. 2021). The joint data will be studied in a forthcoming paper, including the effect of quasi-thermal re-radiation of a fraction the incident flux (Zdziarski & De Marco 2020; Zdziarski et al. 2021). Now, we use them only to estimate the bolometric fluxes of the observations. We utilize a phenomenological Comptonization/reprocessing model to describe the overall shape of the broad band spectra and to estimate the fluxes below 3 keV, while we use our double-corona fits to get the fluxes above 3 keV. The resulting values are given in Table 2.

4. Discussion

We have found that the hard-state spectra above 3 keV are well described by a structured accretion flow with the geometry shown in Figure 4. The energetically dominant component is the hardest one (except for epoch 3, where the two components have comparable fluxes), but its emission is reflected from remote parts of the disk, $R \gtrsim R_{\rm tr} \sim 10^2 R_{\rm g}$. However, the plasma location at $R \gtrsim R_{\rm tr}$ would disagree with a number of arguments. First, the relative similarity in the bolometric flux between the plateau hard state and the soft state (Shidatsu et al. 2019) argues against a radiative inefficiency of the hard state. Then, the most luminous component should originate close to the BH, but not at $\gtrsim 10^2 R_{\rm g}$. Second, low-frequency variability of the observed flux at higher energies lags behind that at a lower energies, which phenomenon is called "hard lags." This has been observed in MAXI J1820+070 (K19; Wang et al. 2020b; De Marco et al. 2021) as well as in other BH XRBs, and it has been interpreted as propagation of fluctuations in the accretion flow (Kotov et al. 2001). In this framework, a plasma emitting a harder spectrum should be located downstream that with a softer spectrum. Third, a hard Comptonization spectrum requires a low flux of incident seed soft photons (e.g., Poutanen et al. 2018), implying a plasma location away from the disk, at $R < R_{\rm in}$, as shown in Figure 4. Its scale height has to be large, as implied by the typical fractional reflection of $\mathcal{R}_{\rm h} \sim 0.5$; see Table 2. Also, the outer disk is likely to be flared, which increases the solid angle subtended by it as seen from the central hot plasma.

Then, the source of the softer X-ray component appears to be at $R > R_{\rm in}$. We propose it forms a corona above the disk. Its softness, with the photon index of $\Gamma \sim 2$, is explained by the re-emission of its flux incident on the disk (Haardt & Maraschi 1991; Poutanen et al. 2018). The underlying disk is strongly ionized by the coronal radiation. The reflection features are mildly relativistic and attenuated by the scattering in the corona. The corona extends out to $R_{\rm tr}$.

Our preferred geometry of the inner accretion flow is similar to that of Mahmoud et al. (2019), shown in their Figure 2, inferred from a study of the BH XRB GX 339–4. The main difference in our picture is that we propose the outer hot plasma to form a corona above a disk, while the soft-emitting plasma in Mahmoud et al. (2019) is placed downstream of the truncation radius. Alternatively, the reflection of the soft emission can be from cold clumps within the hot plasma, as in the model for Cyg X-1 of Mahmoud & Done (2018). In fact, the viscous dissipation within a full disk between $R_{\rm in}$ and $R_{\rm tr}$ is likely to lead, via cooling of the coronal plasma, to spectra softer than those we see in the data. The presence of the underlying cold clumps covering only a fraction of the midplane instead of a full disk would then reduce the cooling; see, e.g., Poutanen et al. (2018). Also, our finding of the spectral complexity, requiring at least two Comptonization components in order to

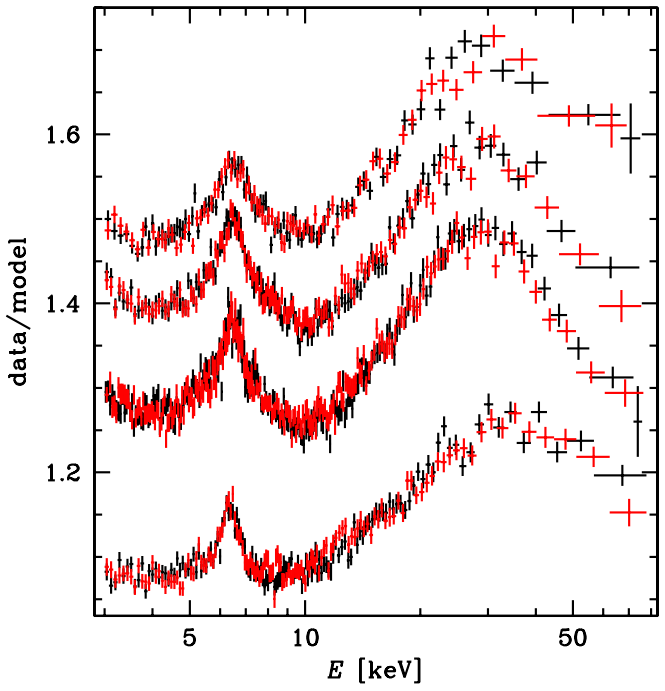

Figure 8. Reflection profiles in the NuSTAR spectra for epochs 1–4 (from bottom to top) presented as the data/model ratios after removing the two reflection components in the model with separate reflection regions. For clarity of display, the profiles for epochs 3 and 4 have been offset by + 0.15 and + 0.35, respectively. We see that the profiles look remarkably similar. Still, the data are fitted with the best-fit values of $R_{\rm in}$ ranging from ≈10 (epoch 4) to >100 (epoch 3), see Table 2.

explain the spectra at >3 keV, agrees with those of Chakraborty et al. (2020) and Wang et al. (2020b) for this source and that of Zdziarski et al. (2021) for XTE J1752–223, another transient BH XRB.

Our finding that the reflection features in the hard state are only mildly relativistically smeared (provided that the fitted inclinations agree with the observational constraints) can explain the fact, pointed out by K19 for the NICER data and by B19 for the NuSTAR data, that the Fe–K range profiles appear similar over the hard state. This is because the relativistic distortion of the rest-frame Fe K spectra is modest. We show the reflection profiles obtained in our fits in Figure 8, with respect to the sum of the two Comptonization components. While the profile for epoch 1 looks relatively narrow, those for 2, 3, and 4 look similarly broad. Still, we have found that the inner radii for reflection of the hard and soft spectral components do vary a lot across the studied data set. In particular, $R_{\rm in} > 100R_{\rm g}$ for epoch 3 while $R_{\rm in} \approx 10R_{\rm g}$ for the best fit to the data for epoch 4. The variability of the characteristic disk radii can readily explain the findings by K19 and B19 that the reverberation and power-spectrum timescales decrease with the increasing softness in spite of the Fe K profiles looking relatively similar.

Therefore, the statements of K19 and B19 that the varying characteristic timescales accompanied by the Fe K complexes looking similar imply strong variations of the coronal scale height above a disk of a constant inner radius (see Figure 4 in K19) appear not certain. The dominant trend found by our spectral fitting is that $R_{\rm tr}$ decreases with the increasing softness of the spectra. Thus, the reverberation timescales will correspond to the distance between the dominant hard-emitting plasma and outer parts of the disk, beyond $R_{\rm tr}$. A contraction/expansion of the corona is still allowed, but it is not required. Given our spectral results, it is unlikely to be the dominant cause of the variable reverberation timescales.

Still, details of the source geometry and its changes with the spectral evolution in the hard state remain unclear. The solid angle subtended by the reflector as seen by the inner hot plasma is large, $\sim 0.5 \times 2\pi$. This requires either a large scale height of that plasma and/or the disk beyond $R_{\rm tr}$ to be flared (see Figure 4) but the latter may cause an obscuration of the central hot plasma. A large scale height can be achieved if the accreting flow is outflowing, as in the model of Beloborodov (1999); Malzac et al. (2001). This may form a slow sheath of the jet (e.g., Reig & Kylafis 2021). Arguments for a part of the X-ray emission of MAXI J1820+070 to be from the jet are presented by Wang et al. (2020b) and Ma et al. (2021). We also note that Dubus et al. (1999) pointed out that while the irradiation of the outer disk is required by the observed light curves of transient BH XRBs, it cannot be achieved in the standard disk model because of self-screening. This requires a geometry in which the solid angle subtended by outer parts of the disk as seen by the central source is large, similar to our finding. Our proposed geometrical model is also incomplete because it does not account for the spectra below 3 keV; see Figure 7. Those data indeed imply the presence of additional components in the accretion flow (Dziełak et al. 2021; De Marco et al. 2021).

5. Conclusions

We have confirmed the findings of a number of previous works that the geometry in the hard state of BH XRBs features a significantly truncated disk, and the dominant trend is a decrease of the characteristic disk radii with the decreasing hardness, i.e., during the evolution toward the soft state. The changes of $R_{\rm in}$ occur in spite the visual appearance of a constancy of the Fe K profile (see Figure 8). For $L \sim 5\% L_{\rm E}$ during the rise of MAXI J1820+070, the truncation radius was $\sim 10^2 R_{\rm g}$, as found with a number of different models.

Then, we find the accretion flow is structured, with at least two primary Comptonization components, the hard (usually dominant) and soft (see Figure 5). The reflection features are dominated by reflection of the hard components far away in the disk. The soft component is responsible for the broader reflection component, also seen in the data. A possible geometry accounting for that is shown in Figure 4.

Our findings imply that the evolutionary changes of the reverberation and power-spectrum timescales can be explained by changes of $R_{\rm in}$ and $R_{\rm tr}$, without the need for invoking a corona contraction.

We have also found another family of spectral solutions with the disk extending to an immediate vicinity of the ISCO, confirming B19 and Chakraborty et al. (2020). However, those solutions require a low inclination, $i \sim 30°$, while the inclinations of the binary and the jet have been found to be in the 60–81° range.

The data at <3 keV from NICER, not modeled in this work, show strong and complex soft X-ray excesses (Figure 7), implying the presence of at least one more Comptonization component, in addition to a disk blackbody.

We thank J. Casares, C. Done, J. Kajava, N. Kylafis, M. Torres, A. Veledina, and Y. Wang for valuable comments and

discussions, and the referee for valuable comments. Special thanks are due to D. Buisson for his finding the low-radius lamppost solution for the current data of epoch 1. We have benefited from discussions during Team Meetings of the International Space Science Institute (Bern), whose support we acknowledge. We also acknowledge support from the Polish National Science Centre under the grants 2015/18/A/ST9/00746 and 2019/35/B/ST9/03944, and from Ramón y Cajal Fellowship RYC2018-025950-I.

ORCID iDs

Andrzej A. Zdziarski https://orcid.org/0000-0002-0333-2452
Marta A. Dziełak https://orcid.org/0000-0002-5801-5470
Barbara De Marco https://orcid.org/0000-0003-2743-6632
Michał Szanecki https://orcid.org/0000-0001-7606-5925
Andrzej Niedźwiecki https://orcid.org/0000-0002-8541-8849

References

Abramowicz, M. A., Chen, X., Kato, S., Lasota, J.-P., & Regev, O. 1995, ApJL, 438, L37
Anders, E., & Grevesse, N. 1989, Geochim. Cosmochim. Acta, 53, 197
Arnaud, K. A. 1996, in ASP Conf. Ser. 101, XSPEC: The First Ten Years, ed. G. H. Jacoby & J. Barnes (San Francisco, CA: ASP), 17
Atri, P., Miller-Jones, J. C. A., Bahramian, A., et al. 2020, MNRAS, 493, L81
Bailer-Jones, C. A. L., Rybizki, J., Fouesneau, M., Mantelet, G., & Andrae, R. 2018, AJ, 156, 58
Bambi, C., Brenneman, L. W., Dauser, T., et al. 2021, SSRv, arXiv:2011.04792
Beloborodov, A. M. 1999, ApJL, 510, L123
Bisnovatyi-Kogan, G. S., & Ruzmaikin, A. A. 1974, Ap&SS, 28, 45
Blandford, R. D., & Payne, D. G. 1982, MNRAS, 199, 883
Blandford, R. D., & Znajek, R. L. 1977, MNRAS, 179, 433
Buisson, D. J. K., Fabian, A. C., Barret, D., et al. 2019, MNRAS, 490, 1350
Cao, X., & Spruit, H. C. 2013, ApJ, 765, 149
Chakraborty, S., Navale, N., Ratheesh, A., & Bhattacharyya, S. 2020, MNRAS, 498, 5873
Dauser, T., García, J., Walton, D. J., et al. 2016, A&A, 590, A76
Davis, S. W., Blaes, O. M., Hubeny, I., & Turner, N. J. 2005, ApJ, 621, 372
De Marco, B., Zdziarski, A. A., Ponti, G., et al. 2021, A&A, submitted
Done, C., Gierliński, M., & Kubota, A. 2007, A&ARv, 15, 1
Dubus, G., Lasota, J.-P., Hameury, J.-M., & Charles, P. 1999, MNRAS, 303, 139
Dziełak, M. A., De Marco, B., & Zdziarski, A. A. 2021, MNRAS, submitted (arXiv:2102.11635)
Frank, J., King, A., & Raine, D. J. 2002, Accretion Power in Astrophysics (Cambridge: Cambridge Univ. Press)
Galeev, A. A., Rosner, R., & Vaiana, G. S. 1979, ApJ, 229, 318
Gandhi, P., Rao, A., Johnson, M. A. C., Paice, J. A., & Maccarone, T. J. 2019, MNRAS, 485, 2642
García, J., & Kallman, T. R. 2010, ApJ, 718, 695
Gendreau, K. C., Arzoumanian, Z., Adkins, P. W., et al. 2016, Proc. SPIE, 9905, 99051H
Haardt, F., & Maraschi, L. 1991, ApJL, 380, L51
Harrison, F. A., Craig, W. W., Christensen, F. E., et al. 2013, ApJ, 770, 103
Kajava, J. J. E., Motta, S. E., Sanna, A., et al. 2019, MNRAS, 488, L18
Kara, E., Steiner, J. F., Fabian, A. C., et al. 2019, Natur, 565, 198
Kawamuro, T., Negoro, H., Yoneyama, T., et al. 2018, ATel, 11399, 1
Kotov, O., Churazov, E., & Gilfanov, M. 2001, MNRAS, 327, 799
Liska, M., Tchekhovskoy, A., & Quataert, E. 2020, MNRAS, 494, 3656
Ludlam, R. M., Miller, J. M., Arzoumanian, Z., et al. 2018, ApJL, 858, L5
Ma, X., Tao, L., Zhang, S.-N., et al. 2021, NatAs, 5, 94
Mahmoud, R. D., & Done, C. 2018, MNRAS, 480, 4040
Mahmoud, R. D., Done, C., & De Marco, B. 2019, MNRAS, 486, 2137
Malzac, J., Beloborodov, A. M., & Poutanen, J. 2001, MNRAS, 326, 417
Martocchia, A., & Matt, G. 1996, MNRAS, 282, L53
McKinney, J. C., Tchekhovskoy, A., & Blandford, R. D. 2012, MNRAS, 423, 3083
Narayan, R., Igumenshchev, I. V., & Abramowicz, M. A. 2003, PASJ, 55, L69
Narayan, R., & Yi, I. 1994, ApJL, 428, L13
Niedźwiecki, A., Szanecki, M., & Zdziarski, A. A. 2019, MNRAS, 485, 2942
Novikov, I. D., & Thorne, K. S. 1973, in Black Holes (Les Astres Occlus), ed. C. Dewitt & B. S. Dewitt (New York, NY: Gordon and Breach), 343
Poutanen, J., & Svensson, R. 1996, ApJ, 470, 249
Poutanen, J., Veledina, A., & Zdziarski, A. A. 2018, A&A, 614, A79
Pringle, J. E. 1997, MNRAS, 292, 136
Reig, P., & Kylafis, N. D. 2021, arXiv:2101.02437
Roques, J.-P., & Jourdain, E. 2019, ApJ, 870, 92
Salvesen, G., Armitage, P. J., Simon, J. B., & Begelman, M. C. 2016, MNRAS, 460, 3488
Shakura, N. I., & Sunyaev, R. A. 1973, A&A, 24, 337
Shapiro, S. L., Lightman, A. P., & Eardley, D. M. 1976, ApJ, 204, 187
Shidatsu, M., Nakahira, S., Murata, K. L., et al. 2019, ApJ, 874, 183
Steiner, J. F., McClintock, J. E., Remillard, R. A., et al. 2010, ApJL, 718, L117
Stevens, A. L., Uttley, P., Altamirano, D., et al. 2018, ApJL, 865, L15
Svensson, R., & Zdziarski, A. A. 1994, ApJ, 436, 599
Torres, M. A. P., Casares, J., Jiménez-Ibarra, F., et al. 2019, ApJL, 882, L21
Torres, M. A. P., Casares, J., Jiménez-Ibarra, F., et al. 2020, ApJL, 893, L37
Tucker, M. A., Shappee, B. J., Holoien, T. W. S., et al. 2018, ApJL, 867, L9
Wang, J., Kara, E., Steiner, J. F., et al. 2020a, ApJ, 899, 44
Wang, Y., Ji, L., Zhang, S. N., et al. 2020b, ApJ, 896, 33
Wilms, J., Allen, A., & McCray, R. 2000, ApJ, 542, 914
Yuan, F., & Narayan, R. 2014, ARA&A, 52, 529
Yuan, Y., Blandford, R. D., & Wilkins, D. R. 2019a, MNRAS, 484, 4920
Yuan, Y., Spitkovsky, A., Blandford, R. D., & Wilkins, D. R. 2019b, MNRAS, 487, 4114
Zdziarski, A. A., & De Marco, B. 2020, ApJL, 896, L36
Zdziarski, A. A., De Marco, B., Szanecki, M., Niedźwiecki, A., & Markowitz, A. 2021, ApJ, 906, 69

Chapter 5

Paper III

Monthly Notices of the ROYAL ASTRONOMICAL SOCIETY

MNRAS **506,** 2020–2029 (2021) https://doi.org/10.1093/mnras/stab1700
Advance Access publication 2021 June 14

A spectrally stratified hot accretion flow in the hard state of MAXI J1820+070

Marta A. Dziełak [1]★ Barbara De Marco[1,2] and Andrzej A. Zdziarski [1]

[1]*Nicolaus Copernicus Astronomical Center, Polish Academy of Sciences, Bartycka 18, PL-00-716 Warszawa, Poland*
[2]*Departament de Física, EEBE, Universitat Politècnica de Catalunya, Av. Eduard Maristany 16, E-08019 Barcelona, Spain*

Accepted 2021 June 10. Received 2021 May 16; in original form 2021 February 23

ABSTRACT

We study the structure of the accretion flow in the hard state of the black hole X-ray binary MAXI J1820+070 with *NICER* data. The power spectra show broad-band variability which can be fit with four Lorentzian components peaking at different time-scales. Extracting power spectra as a function of energy enables the energy spectra of these different power spectral components to be reconstructed. We found significant spectral differences among Lorentzians, with the one corresponding to the shortest variability time-scales displaying the hardest spectrum. Both the variability spectra and the time-averaged spectrum are well-modelled by a disc blackbody and thermal Comptonization, but the presence of (at least) two Comptonization zones with different temperatures and optical depths is required. The disc blackbody component is highly variable, but only in the variability components peaking at the longest time-scales ($\gtrsim 1$ s). The seed photons for the spectrally harder zone come predominantly from the softer Comptonization zone. Our results require the accretion flow in this source to be structured, and cannot be described by a single Comptonization region upscattering disc blackbody photons, and reflection from the disc.

Key words: accretion, accretion discs – X-rays: binaries – X-rays: individual (MAXI J1820+070).

1 INTRODUCTION

The majority of known black hole (BH) X-ray binaries (XRBs) are transient (Coriat, Fender & Dubus 2012). They spend most of their time in a quiescent state, characterized by low/undetectable levels of the X-ray luminosity, $L_{\rm X}/L_{\rm Edd} \lesssim 10^{-5}$ (where $L_{\rm Edd}$ is the Eddington luminosity). After some years of quiescence, they go through X-ray brightening episodes, or outbursts, lasting from a few to tens of months. During an outburst the X-ray spectral and timing properties change dramatically (e.g. Belloni et al. 2005; Homan & Belloni 2005; Dunn et al. 2010; Muñoz-Darias, Motta & Belloni 2011; Heil, Uttley & Klein-Wolt 2015), and the source goes through a sequence of different accretion states. At the beginning and at the end of an outburst the source is observed in a hard state, spectrally dominated by a hard X-ray thermal Comptonization component (e.g. a review by Done, Gierliński & Kubota 2007). During the hard state the source becomes increasingly brighter at almost constant spectral hardness, typically over periods of weeks to a few months. Apart from the dominant hard X-ray Comptonization component, broad-band X-ray data show spectral complexity, requiring additional components. Many hard state spectra show a soft component, which can be ascribed, at least partly, to the hardest part of the disc thermal emission (due to intrinsic dissipation and/or hard X-ray irradiation, e.g. Zdziarski & De Marco 2020), with a typical inner temperature of $kT_{\rm in} \sim 0.1$–0.3 keV. At higher energies, signatures of disc reflection are clearly observed. Fits with relativistic models have yielded controversial results (see Bambi et al. 2020 for a review). Some of these studies support the presence of a disc reaching the immediate vicinity of the innermost stable circular orbit (ISCO) already at relatively low luminosities in the hard state (e.g. Miller et al. 2006, 2008; Reis et al. 2008; Tomsick et al. 2008; Reis, Fabian & Miller 2010; Petrucci et al. 2014; García et al. 2015; Wang-Ji et al. 2018). Other studies are instead in agreement with a disc truncated at large radii (a few tens of $R_{\rm g}$, where $R_{\rm g} = GM/c^2$ is the gravitational radius and M is the BH mass) from low to high hard-state luminosities (e.g. Esin et al. 2001; McClintock et al. 2001; Done & Diaz Trigo 2010; Kolehmainen, Done & Díaz Trigo 2014; Plant et al. 2015; Basak & Zdziarski 2016; Dziełak et al. 2019). The latter results are in line with theoretical models which predict evaporation of the inner disc (Meyer, Liu & Meyer-Hofmeister 2000; Petrucci et al. 2008; Begelman & Armitage 2014; Kylafis & Belloni 2015; Cao 2016).

One way to understand the origin of these discrepancies is to consider more complexity in the underlying Comptonization continuum. The continuum is usually assumed to result from scattering of disc photons in a homogeneous region near the BH, which in most cases results in a flat or convex spectral shape. On the other hand, inhomogeneity of the Comptonization region is able to produce additional curvature, resulting in a concave underlying continuum, as often required by the data (Di Salvo et al. 2001; Frontera et al. 2001; Ibragimov et al. 2005; Makishima et al. 2008; Nowak et al. 2011; Yamada et al. 2013; Basak et al. 2017; Zdziarski et al. 2021a). Such conditions can account for both a part of the Fe K line red wing and a part of the reflection hump at $\gtrsim$10 keV, which allow the need for extreme relativistic reflection parameters, as well as a super-solar Fe abundance (often found in the fits, Fürst et al. 2015; García et al. 2015; Parker et al. 2015, 2016; Walton et al. 2016, 2017; Tomsick et al. 2018) to be relaxed. The presence of

★ E-mail: mdzielak@camk.edu.pl

a radially stratified and spectrally inhomogeneous Comptonization region is independently supported by X-ray variability studies. In particular, the common detection of frequency-dependent hard X-ray lags (hard X-ray variations lagging soft X-ray variations) in energy bands dominated by the primary hard X-ray continuum can be explained by mass accretion rate fluctuations propagating inward (Lyubarskii 1997; Arévalo & Uttley 2006). However, in order to detect a net hard lag, the zone these perturbations propagate through must have a radially dependent emissivity profile, with the inner regions emitting a harder spectrum (Kotov, Churazov & Gilfanov 2001). Spectral-timing techniques, which allow resolving the spectral components contributing to variability on different timescales (frequency-resolved spectroscopy) have been applied to BH XRBs, showing that those spectra generally harden with decreasing timescale. This also provides evidence for the differences in the observed spectral shape to be related to their different distances from the BH; see, e.g. Revnivtsev, Gilfanov & Churazov (1999) a nd Axelsson & Done (2018). Following these findings, Mahmoud & Done (2018) and Mahmoud, Done & De Marco (2019) created theoretical models reproducing those observations by multizone models coupled with propagation mass accretion rate fluctuations.

We study the BH XRB system MAXI J1820+070, focusing on two *Neutron star Interior Composition ExploreR* (*NICER*; Gendreau et al. 2016) observations taken during the rise of its 2018 outburst (see De Marco et al. 2021, for a systematic analysis of all the first part of the outburst). We perform frequency-resolved spectroscopy method in the formulation outlined by Axelsson & Done (2018). We fit frequency-resolved energy spectra using Comptonization models, with the goal to constrain the structure of the hot flow, and verify the possible presence of multiple Comptonization zones.

MAXI J1820+070 was first detected in the optical wavelengths by the All-Sky Automated Search for SuperNovae on 2018-03-06 (ASASSN-18ey, Tucker et al. 2018). It was detected in X-rays 5 d later by the Monitor of All-sky X-ray Image (MAXI; Matsuoka et al. 2009) on board of *International Space Station* (Kawamuro et al. 2018). The two detections were connected to the same source by Denisenko (2018). It was then identified as a BH candidate (Kawamuro et al. 2018; Shidatsu et al. 2019). Torres et al. (2019) confirmed the presence of a BH by dynamical studies of the system in the optical band, and Torres et al. (2020) measured in detail the parameters of the system. The donor is a low-mass K star and the orbital period is 0.68549 ± 0.00001 d (Torres et al. 2019).

The BH mass is $M \approx (5.95 \pm 0.22) \mathrm{M}_{\odot}/\sin^3 i$ (Torres et al. 2020), anticorrelated with the binary inclination, i. Those authors estimated the latter as $66^\circ < i < 81^\circ$. On the other hand, Atri et al. (2020) estimated the inclination of the jet[1] as $i \approx 63 \pm 3^\circ$. Based on their radio parallax, Atri et al. (2020) determined the distance to MAXI J1820+070 as $d \approx 3.0 \pm 0.3$ kpc, consistent with the *Gaia* Data Release 2 parallax, yielding $d \approx 3.5^{+2.2}_{-1.0}$ kpc (Bailer-Jones et al. 2018; Gandhi et al. 2019; Atri et al. 2020). MAXI J1820+070 is a relatively bright source, with the peak 1–100 keV flux estimated by Shidatsu et al. (2019) as $\approx 1.4 \times 10^{-7}$ erg cm^{-2} s^{-1}, which corresponds to the isotropic luminosity of $\approx 1.5 (d/3\,\mathrm{kpc})^2 \times 10^{38}$ erg s^{-1}. Assuming an inclination $i = 66^\circ$ this corresponds to $\sim$15 per cent L/L_{Edd}. The value of Galactic hydrogen column density toward the source has been estimated in the range of $(0.5–2) \times 10^{21}$ cm^{-2} (Uttley et al. 2018; Kajava et al. 2019; Fabian et al. 2020; Xu et al. 2020).

[1]We note that the two inclinations can be different, and, in fact, are significantly different in some BH XRBs, e.g. GRO 1655–40, (Hjellming & Rupen 1995; Beer & Podsiadlowski 2002).

Table 1. The log of the *NICER* observations used for the analysis. Exposures correspond to the effective on-source time after data cleaning.

Obs. ID	Start time (yyyy-mm-dd hh:mm:ss)	Exposure (s)
1200120**103**	2018-03-13 23:56:12	9474
1200120**104**	2018-03-15 00:36:04	6231

2 DATA REDUCTION

For our analysis, we choose two relatively long observations of MAXI J1820+070 carried out by *NICER*, see Table 1. Hereafter, we refer to the studied observations using only the last three digits of their identification number (ID), i.e. 103 and 104. They correspond to the initial phases of the 2018 outburst, when the source was in the rising hard state (see fig. 1 in De Marco et al. 2021). We estimate[2] their energy fluxes to be $\approx$6.5 and $\approx 9.5 \times 10^{-9}$ erg cm^{-2} s^{-1}, respectively, in the 0.3–10 keV energy band.

The data were reduced using the `NICERDAS` tools in `HEASOFT` v.6.25, starting from the unfiltered, calibrated, all Measurement/Power Unit (MPU) merged files, `ufa`. We applied the standard screening criteria (e.g. Stevens et al. 2018) through the `NIMAKETIME` and `NICERCLEAN` tools. We check for periods of high particle background, i.e. with rate >2 count s^{-1}, by inspecting light curves extracted in the energy range of 13–15 keV, in which the contribution from the source is negligible because of the drop in the effective area (Ludlam et al. 2018).

Of the 56 focal plane modules (FPMs) of the *NICER* X-ray Timing Instrument (XTI), four (FPMs 11, 20, 22, and 60) are not operational. Additionally, we filter out FPMs 14 and 34, since they are found to occasionally display increased detector noise.[3] Thus, the number of FPMs used for our analysis is 50. In order to correct for the corresponding reduction of effective area, the reported source fluxes were rescaled by the number of used FPMs.

The shortest good time intervals, with the length <10 s, were removed from the analysis, resulting in the net, on-source, exposure times reported in Table 1. Filtered event lists were barycentre-corrected and used to extract the light curves and spectra using `XSELECT` v.2.4e. We used publicly distributed ancillary response and redistribution matrix files[4] as of 2020-02-12 and 2018-04-04, respectively. Fits were performed using the X-Ray Spectral Fitting Package (XSPEC v.12.10.1; Arnaud). Hereafter uncertainties are reported at the 90 per cent confidence level for a single parameter.

3 ANALYSIS

3.1 Power spectral density

We first compute and fit the power spectral density (PSD) for each of the observations in two broad energy bands, 0.3–2 and 2–10 keV, in order to identify components contributing to the observed variability on different time-scales. We extract light curves with a time bin of 0.4 ms in these energy bands. The light curves were split into

[2]We have used a model including a disc blackbody plus a power law, both absorbed by the cold gas in the interstellar medium; `TBabs(diskbb+powerlaw)` in XSPEC.

[3]https://heasarc.gsfc.nasa.gov/docs/nicer/data_analysis/nicer_analysis_tips.html

[4]https://heasarc.gsfc.nasa.gov/docs/heasarc/caldb/data/nicer/xti/index.html

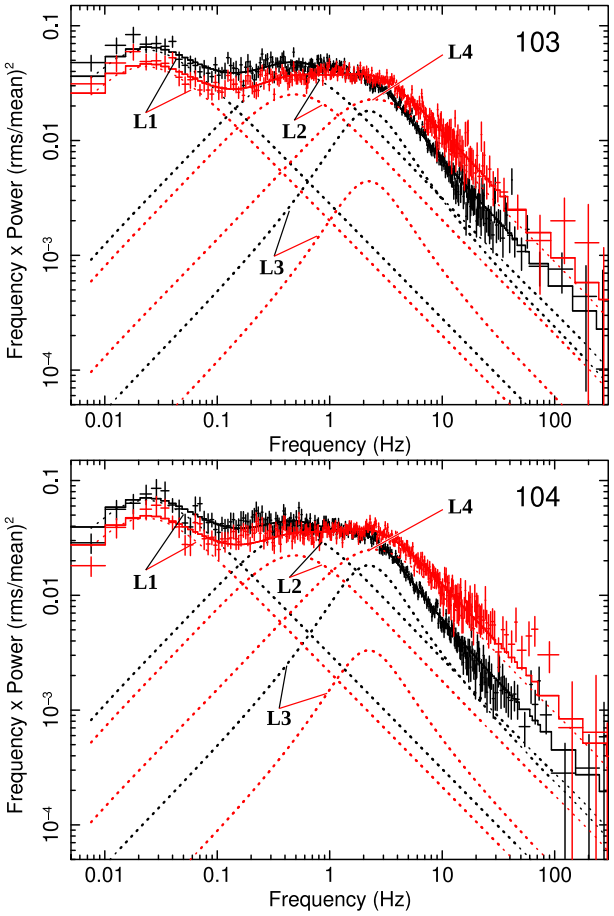

Figure 1. The Poisson noise subtracted PSDs of the two analysed observations in the two energy bands, 0.3–2 keV (black symbols) and 2–10 keV (red symbols). The total best-fitting models (solid lines) and the Lorentzian components of the model (dotted curves) are also shown.

segments of 200 s length. We calculate the PSD of each segment and average them, in order to obtain more accurate estimates of the PSD of each single observations. The chosen time bin and the segment length allow us to cover the range of frequencies of 0.005–1250 Hz. This range well samples both the broad-band noise intrinsic to the source and the Poisson noise level. The latter was fit at frequencies of $\nu > 300$ Hz and subtracted from the PSDs at all frequencies. We adopt a logarithmic rebinning in order to improve the statistics at high frequencies.

We normalize the PSDs using the fractional squared root-mean-square units [(*rms*/mean rate)^{2}Hz^{-1}, Belloni & Hasinger 1990; Miyamoto et al. 1992]. The PSDs are shown in Fig. 1. Their complex structure hints at the presence of several variability components. As commonly done in the literature (Belloni et al. 1997; Nowak 2000), we fit each PSD with a sum of Lorentzian components, for which we use XSPEC. A Lorentzian is described by

$$P(\nu) = K\frac{\sigma}{2\pi}\frac{1}{(\nu-\nu_0)^2+(\sigma/2)^2}, \quad (1)$$

where K is the normalization, σ is the full width at half-maximum, and ν_0 is the centroid frequency. However, the maximum power (i.e. the peak of $\nu P(\nu)$) is observed at the frequency $\nu_{\rm max} > \nu_0$ (Belloni et al. 1997):

$$\nu_{\rm max} = \sqrt{\nu_0^2 + \left(\frac{\sigma}{2}\right)^2}. \quad (2)$$

Table 2. The results of the joint fits of the PSDs of the observations 103 and 104 in the 0.3–2 and 2–10 keV energy bands with the model consisting of four Lorentzians, see equation (1). We also give the resulting peak frequency of $\nu P(\nu)$, equation (2), and the resulting reduced χ^2.

	L1	L2	L3	L4
ν_0 (Hz)	$0^{+0.006}$	$0.095^{+0.038}_{-0.039}$	$1.59^{+0.16}_{-0.18}$	$0.65^{+0.27}_{-0.65}$
σ (Hz)	$0.045^{+0.004}_{-0.003}$	$0.96^{+0.09}_{-0.08}$	$3.07^{+0.11}_{-0.09}$	$4.80^{+1.01}_{-0.35}$
$\nu_{\rm max}$ (Hz)	$0.023^{+0.002}_{-0.002}$	$0.489^{+0.045}_{-0.039}$	$2.21^{+0.12}_{-0.13}$	$2.49^{+0.49}_{-0.24}$
χ^2_ν		0.993		

We jointly fit the resulting four PSDs, we tie ν_0 and σ parameters, but allow for different normalization. We start with fitting a single Lorentzian, and add a new one if significant residuals remained. We find that the hard band is well described by four Lorentzian components, but an addition of the highest-frequency, fourth, Lorentzian in the soft band PSD yields a normalization consistent with zero. We also find that letting ν_0 and σ vary independently for each PSD does not lead to significant fit improvements. Therefore, our final joint model consists of four Lorentzians (hereafter L1, L2, L3, and L4), with the parameters given in Table 2. The Poisson noise subtracted PSDs with the best-fit models are shown in Fig. 1.

We check that the PSDs of the two observations have compatible shape and consistent fractional normalization in each of the two energy bands (≈32 and ≈27 per cent in the soft and hard bands, respectively). This means that there is no significant deviation from stationarity between the two observations. Therefore, we decide to combine the two observations in order to obtain a higher signal to noise for the remainder of our analysis.

3.2 Extraction of frequency-resolved spectra

We extract the fractional *rms* and absolute *rms* energy spectra using the Lorentzian fits presented in Section 3.1. The fractional *rms* spectrum shows the distribution of fractional variability power as a function of energy (e.g. Vaughan et al. 2003) and can be used to readily assess the presence of spectral variability (e.g. presence of multiple variable spectral components, spectral pivoting). On the other hand, the absolute *rms* spectrum shows the spectral shape of the components that contribute to variability, and can be used to directly fit spectral models. However, this comes with some caveats that will be discussed in Section 4. We use the technique proposed by Axelsson, Hjalmarsdotter & Done (2013). We create a logarithmic energy grid with 47 bins in the 0.3–9.9 keV energy range. We then calculate the PSD in fractional (*rms*/mean rate)^{2}Hz^{-1} and absolute units ((count s^{-1})^{2}Hz^{-1}, Vaughan et al. 2003) for each of the bins. We then fit the PSD in each band with the same Lorentzian components as the best-fit model to the PSD of the broad energy bands (Table 2), keeping the values of ν_0 and σ fixed, and allowing only the normalization of each Lorentzian to vary. The best-fit PSD models for each narrow energy band are then used to extract the fractional and absolute *rms* variability amplitude spectrum of each Lorentzian. To this aim we analytically integrate the best-fit Lorentzians within the frequency range 0.001–1000 Hz, such that:

$$rms = \sqrt{\left(\frac{K}{\pi}\right)\arctan\left(\frac{(\nu-\nu_0)}{\sigma/2}\right)\Bigg|_{\nu=0.001}^{\nu=1000}}. \quad (3)$$

We plot these values as a function of energy to obtain the fractional and absolute *rms* spectra. Results are reported in Fig. 2. We note that

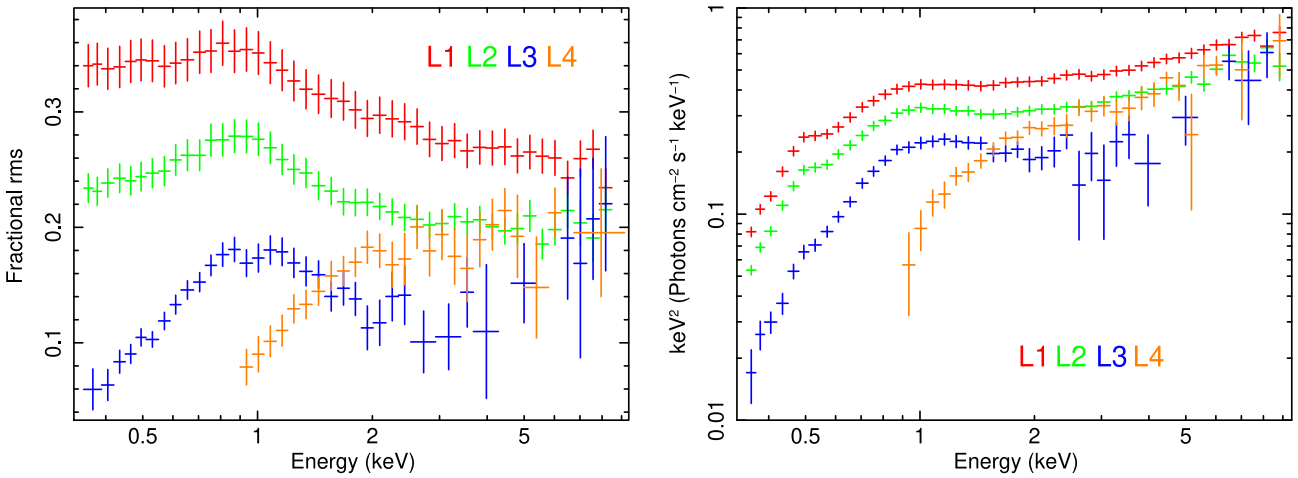

Figure 2. The fractional *rms* spectra (left-hand panel) and absolute *rms* spectra (right-hand panel) of each of the four Lorentzian components, unfolded to a constant model.

since these four components were obtained from the power spectrum, which gives rms^2, they were assumed to be completely uncorrelated, and, in order to obtain the total *rms* spectrum, the single *rms* spectra have to be summed in quadrature. We note that the *rms* spectra have the redistribution matrix obtained by rebinning the matrix for the average spectrum.

The errors on the *rms* spectra were calculated based on the 1σ deviation of the normalization of the best-fit Lorentzians. To this aim, for each Lorentzian and in each energy band, we draw two random numbers distributed according to a Gaussian distribution with the mean equal to the best-fit value of the normalization, K, and the standard deviation equal to its 1σ lower/upper error of K. This procedure was repeated 100 times for each Lorentzian component, resulting in two sets of 100 simulations each. We use each set to estimate the upper and lower limits on the *rms* in every energy channel. In order to have symmetric errors (as required in XSPEC) we take the average of the obtained upper and lower errors. The unconstrained points, i.e. those resulting in upper limits on the *rms* (e.g. as in the case of the normalization of L4 in the softest energy bands) were omitted in the fits and are not presented in the plots.

The fractional *rms* spectra of each Lorentzian show significant spectral variability (Fig. 2, left). In particular, in the low-frequency components (L1, L2, and L3) a local peak of variability is observed at around 1 keV (at the peak the fractional *rms* decreases from ∼36 to ∼18 per cent from low to high frequencies). Then, on either side of the peak the fractional rms tends to decrease. While for L1 and L2 the decrease is steady up to the highest sampled energies, for L3 a reversal of this trend is observed above ∼3 keV. L4 does not show any low energy peak, and the variability at around ∼1 keV results suppressed. In L1, L2, and L4, the fractional variability appears to flatten out at energies $\gtrsim$3 keV (to a level of ∼26 per cent for L1, and ∼20 per cent for L2 and L4). This suggests that high energy spectral components predominantly vary in normalization only. We note that these results are in agreement with those reported by Axelsson & Veledina (2021).

3.3 Spectral fits of absolute *rms* and time-averaged spectra

We then proceed to fit absolute *rms* and time-averaged spectra, using standard XSPEC models. In our models, absorption due to the interstellar medium (ISM) is modelled using `tbabs` (Wilms, Allen & McCray 2000), with the elemental abundances from the same paper. We model thermal Comptonization using the model `ThComp` (Zdziarski et al. 2020). Since this is a convolution model, the covered energy range has to be extended beyond that of the *NICER* spectra in order to get a full range of energies for the seed photons; we use[5] the range of 0.01–2000 keV. Since at high energies the sensitivity of the instrument is limited to $E \lesssim 10$ keV, we are not able to fit the electron temperature, and we fix it at $kT_e = 50$ keV, which closely resembles the values found from simultaneous fits of *NuSTAR* data (Zdziarski et al. 2021b). In our modelization, we assume that all the parameters governing the shape of the spectral components are constant and that the variability associated within each Lorentzian is predominantly due to variations in normalization of the spectral components. In particular, our modelization discards spectral pivoting, as suggested by fractional *rms* spectra (Fig. 2, left; see also discussion in Section 4).

We first consider single Comptonization models, with the disc thermal emission (Mitsuda et al. 1984) being the source of seed photons. The ISM hydrogen column density is fixed at $N_H = 1.4 \times 10^{21}\mathrm{cm}^{-2}$ (which is the best-fit value obtained from our fit to the time-averaged spectrum, see Table 4 below). `ThComp` has the fraction of the seed photons incident on the Comptonization region, f, as a free parameter. However, we hereafter set $f = 1$ and include a separate disc blackbody component with the same parameters in order to separate the two components in the plots and tables. The XSPEC notation of the model is `TBabs(diskbb`$_1$`+ThComp(diskbb`$_2$`))`. We note that such additive form of the variability model spectrum assumes that the two spectral components are fully correlated. In our first case, Model A, we fit *rms* spectra of each Lorentzian (L1, L2, L3, and L4) with the same parameters except for the normalizations. The normalization of `thComp` is given by the normalization of the convolved `diskbb` model. The other free parameters are the inner disc temperature, kT_{in}, and the low-energy spectral index of the Comptonization spectrum, Γ (defined by the energy flux, $F(E) \propto E^{1-\Gamma}$). The obtained best-fit parameters are given in Table 3 and the ratios of the data to the model are shown in Fig. 3 (top panel). We find that this model provides a rather poor description of the data, $\chi^2_\nu \approx 318.8/160$.

[5]The XSPEC commands `energies extend low 0.001` and `energies extend high 2000` were used. This avoids modifying the energy grid of the data.

Table 3. The joint fit results for models with a single Comptonization zone for each of the Lorentzians (L1, L2, L3, and L4). The XSPEC notation is `TBabs(diskbb1+ThComp(diskbb2))`. The normalization of `thComp` is given by the normalization of the convolved `diskbb` model. In Model A, the Comptonization plasmas have the same parameters for all of the Lorentzians, and in Model B, they can differ in the optical depth, resulting in different spectral indices, Γ. Model C is a phenomenological one, in which the inner disc temperatures, $kT_{\rm in2}$, of the seed photons for Comptonization can also differ between the Lorentzians. Hereafter, the parameters assumed to be fixed are denoted by (F).

		A				B				C			
Component	Parameter	L1	L2	L3	L4	L1	L2	L3	L4	L1	L2	L3	L4
TBabs	$N_{\rm H}$ (10^{21} cm^{-2})	1.4 (F)				1.4 (F)				1.4 (F)			
diskbb$_1$	$kT_{\rm in1}$ (keV)	$0.24^{+0.01}_{-0.01}$				$0.23^{+0.01}_{-0.01}$				$0.21^{+0.01}_{-0.01}$			
	N_1 (10^3)	$15.8^{+2.4}_{-1.9}$	$8.1^{+0.5}_{-0.5}$	$3.2^{+0.5}_{-0.5}$	$0^{+0.1}$	$19.0^{+3.3}_{-2.6}$	$13.7^{+2.1}_{-1.8}$	$0^{+0.4}$	$0^{+0.4}$	$23.7^{+4.7}_{-3.7}$	$19.6^{+4.0}_{-3.6}$	$0^{+0.8}$	$0^{+0.8}$
ThComp	Γ	$1.56^{+0.03}_{-0.03}$				$1.64^{+0.04}_{-0.04}$	$1.63^{+0.05}_{-0.05}$	$1.91^{+0.06}_{-0.05}$	$1.32^{+0.06}_{-0.06}$	$1.67^{+0.04}_{-0.04}$	$1.64^{+0.05}_{-0.05}$	$2.20^{+0.18}_{-0.13}$	$1.48^{+0.27}_{-0.13}$
	$kT_{\rm e}$ (keV)	50 (F)				50 (F)				50 (F)			
diskbb$_2$	$kT_{\rm in2}$ (keV)	$= kT_{\rm in1}$				$= kT_{\rm in1}$				$= kT_{\rm in1}$	$0.34^{+0.11}_{-0.09}$	$0.32^{+0.03}_{-0.03}$	$0.83^{+0.39}_{-0.29}$
	N_2 (10^3)	$8.1^{+1.7}_{-1.3}$	$6.1^{+1.2}_{-0.9}$	$4.9^{+1.0}_{-0.8}$	$5.2^{+0.9}_{-0.7}$	$12.5^{+2.8}_{-2.2}$	$8.9^{+2.1}_{-1.6}$	$9.7^{+1.6}_{-1.3}$	$5.7^{+0.9}_{-0.7}$	$16.8^{+3.0}_{-3.3}$	$2.1^{+3.4}_{-1.4}$	$2.8^{+1.1}_{-0.8}$	$0.07^{+0.30}_{-0.05}$
	χ^2_ν	318.8/160				232.7/157				185.9/154			

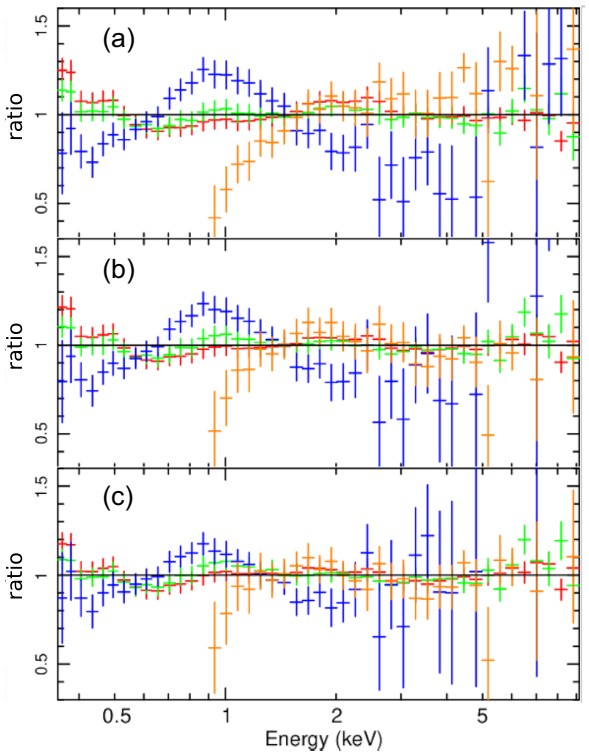

Figure 3. The data-to-model ratios of Models A, B, and C (from top to bottom; see Table 3). The same colour coding as in Fig. 2 is used: L1 – red, L2 – green, L3 – blue, and L4 – orange.

We thus check if a more complex spectral structure can improve the fits. In Model B, we allow for the photon index, Γ, to vary among different Lorentzians. This means that we assume the presence of four different Comptonization zones with different Thomson optical depths, $\tau_{\rm T}$, since the spectral index is a function of both $kT_{\rm e}$ and $\tau_{\rm T}$ [see equation 14 in Zdziarski et al. (2020) and Sunyaev & Titarchuk (1980) for a general discussion].

In Model C, we also allow for changes among $kT_{\rm in}$ of the seeds for Comptonization, and allow them to be different from the directly observed disc blackbody. However, we find the seed photons temperature of the *rms* spectrum of L1 to be unconstrained, so we keep it equal to $kT_{\rm in}$ of the directly observed disc. Model C assumes the presence of four different disc blackbodies. While it is unrealistic, we include it as a phenomenological description in order to highlight that the data do require the seed photons to have different characteristic energies for different components. The best-fit parameters of Models B and C are given in Table 3, while the ratios of the data to the corresponding best-fit models are shown in Fig. 3 (middle and bottom panel).

Comparing results from the spectral fits of Model A with those of B and C, we see significant evidence for changes of the spectral properties between the *rms* spectra of the different Lorentzians. In particular, the fit improves when letting an increasing number of parameters free to vary among the different variability components (from Model A to Model C, $\Delta\chi^2 \approx -133$). The data show that the two lowest frequency Lorentzians L1 and L2 have very similar spectra, L3 has the softest spectrum (we note that in this case, the poor signal-to-noise at high energies may be the reason for such softening), and L4 has the hardest spectrum. We also observe that the *rms* spectrum of the highest frequency Lorentzian (L4) is best fit by a much higher seed photons temperature ($kT_{\rm in2}$ in Table 3) than the lower frequency components. This hints at a different source of seed photons for L4, thus suggesting that the innermost parts of the accretion flow are fueled by photons with higher temperature than those fueling the outer parts.

Given the clear indications of changes in spectral properties among different Lorentzian components, we model now the *rms* spectra and the time-averaged spectrum simultaneously, with the aim of obtaining more robust and self-consistent constraints on the structure of the Comptonization region. For consistency with the *rms* spectra, the time-averaged spectra of observations 103 and 104 were averaged (using `MATHPHA` in FTOOLS). The resulting spectrum was rebinned so as to have a minimum of three original energy channels and signal-to-noise $\geq$50 in each new energy channel. To account for uncertainties in the current calibration, a systematic error of 1 per cent was added. (Note that this step is not required for the *rms* spectra, owing to their lower resolution.) Given the limited bandpass of *NICER*, we did not include complex reflection models in the fits, which would result in overfitting the *rms* spectra. Therefore, we model the fluorescent Fe K line with a simple Gaussian component.

Results obtained from our fits with Model C show that the overall spectrum cannot be fit by a single Comptonization component. We therefore test for a more complex model, assuming that the hot flow can be described by two Comptonization zones. The model, denoted as D, comprises a directly visible disc (zone I), which photons are upscattered in the outer Comptonization zone II, and those upscattered photons are partly directly observed and partly are

Table 4. The joint fit results for Model D with disc blackbody and two Comptonization zones for each of the *rms* components and the time-averaged spectrum, S_{av}. The XSPEC notation is `TBabs(diskbb1+ThComp1(diskbb2)+ThComp2(ThComp1(diskbb3))+Gaussian)`. The single `diskbb` emission is split between three parts with the same kT_{in} and different normalizations, N_1, N_2, and N_3. The Roman numbers correspond to the zones shown in Fig. 4. The component fluxes, F, are unabsorbed and bolometric (measured in the energy range 0.001–2000keV).

					D		
	Component	Parameter	L1	L2	L3	L4	S_{av}
	TBabs	N_H (10^{21} cm^{-2})			$1.4^{+0.1}_{-0.1}$		
I	diskbb$_1$	kT_{in} (keV)			$0.18^{+0.01}_{-0.01}$		
		N_1 (10^3)	$52.7^{+10.2}_{-9.8}$	$34.8^{+9.8}_{-6.4}$	$0^{+3.2}$	$0^{+1.4}$	$100.6^{+30.1}_{-18.8}$
		F (10^{-9} erg cm^{-2} s^{-1})	$1.21^{+0.23}_{-0.22}$	$0.79^{+0.23}_{-0.15}$	$0^{+0.07}$	$0^{+0.03}$	$2.31^{+0.69}_{-0.43}$
II	ThComp$_1$	Γ_1			$1.65^{+0.14}_{-0.13}$		
		kT_{e1} (keV)			$0.34^{+0.04}_{-0.03}$		
	diskbb$_2$	N_2 (10^3)	$8.9^{+3.8}_{-2.2}$	$7.1^{+2.9}_{-1.7}$	$10.6^{+1.8}_{-1.5}$	$0^{+0.5}$	$8.9^{+4.2}_{-2.4}$
		F (10^{-9} erg cm^{-2} s^{-1})	$0.47^{+0.21}_{-0.11}$	$0.38^{+0.19}_{-0.11}$	$0.57^{+0.12}_{-0.09}$	$0^{+0.03}$	$0.48^{+0.27}_{-0.16}$
III	ThComp$_2$	Γ_2			$1.49^{+0.01}_{-0.01}$		
		kT_{e2} (keV)			50 (F)		
	diskbb$_3$	N_3 (10^3)	$13.5^{+2.9}_{-1.8}$	$9.9^{+2.1}_{-1.3}$	$4.7^{+1.3}_{-0.8}$	$9.3^{+1.3}_{-1.1}$	$48.6^{+9.8}_{-6.1}$
		F (10^{-9} erg cm^{-2} s^{-1})	$14.61^{+3.16}_{-1.93}$	$10.75^{+8.48}_{-2.06}$	$5.08^{+1.28}_{-0.77}$	$10.06^{+1.23}_{-1.05}$	$52.64^{+9.56}_{-5.91}$
	Gaussian	E (keV)			$6.5^{+0.1}_{-0.1}$		
		σ (keV)			$0.39^{+0.04}_{-0.08}$		
		N (10^{-3} cm^{-2} s^{-1})	$0^{+1.06}$	$0^{+4.3}$	$0^{+4.3}$	$0^{+4.3}$	$4.3^{+0.8}_{-0.8}$
		χ^2_ν			157.793/150		213.571/255
					370.4/415		

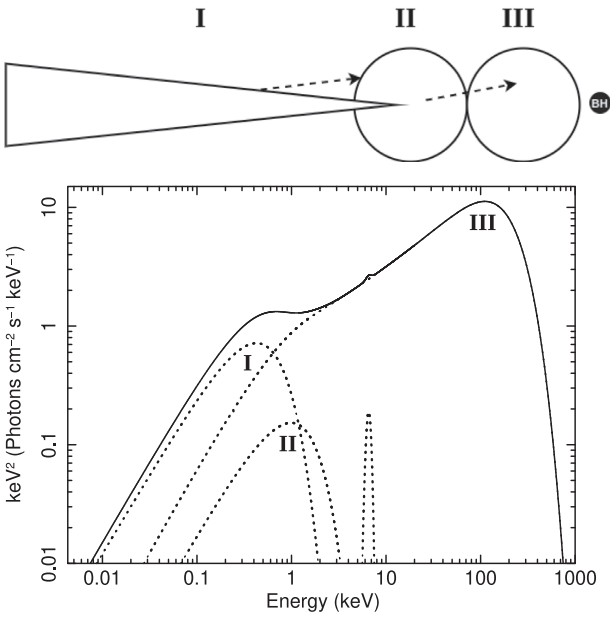

Figure 4. Top panel: a drawing of the geometry assumed in Model D. Bottom panel: the unabsorbed best fit to the time-averaged spectrum (solid curve) and its components (dotted curves) marked by the zones shown in the top panel and Table 4.

upscattered in the inner Comptonization zone III, as illustrated in the drawing in Fig. 4 (top panel). The XSPEC notation is given in the caption to Table 4. Again, the underlying assumption is that the three components are fully correlated. The unabsorbed best-fit model to the time-averaged spectrum with these components is presented in Fig. 4 (bottom panel). Since the Fe line is unconstrained in the *rms* spectra, we require their normalizations to be $\leq$ than that in the time-averaged spectrum. The best-fitting parameters are given in Table 4, and the best-fit model and the data-to-model ratios are shown in Fig. 5. We find that Model D can simultaneously describe the time-averaged and *rms* spectra well, with $\chi^2_\nu \approx 370.4/415$. These results can be summarized as follows.

3.3.1 *Low-frequency Lorentzians (L1 and L2)*

In Model D, the *rms* spectra of L1 and L2 show significant contributions from all of their spectral components (see normalizations in Table 4). Still, most of the photons related to the variability component piking at frequencies $\lesssim$1 Hz are associated with the direct disc emission, which variable components comprise $\approx$63 per cent of the total (time-average) disc blackbody flux at the best fit. In zone II, the variable components actually exceed the corresponding time-average, which implies an inaccuracy resulting from the assumed spectral model (see Section 4). Still, it indicates that most of the photons in this zone are variable.

3.3.2 *High-frequency Lorentzians (L3 and L4)*

These variability components show no direct emission from the disc at the best fit. This means that the disc gives low contribution to the variability components peaking at the time-scales $\gtrsim$1 Hz. Almost all blackbody photons are instead used as seeds for the Comptonization regions. For L3, $\approx$3/4 of those seed photons are Compton upscattered in the outer Comptonization region (zone II),

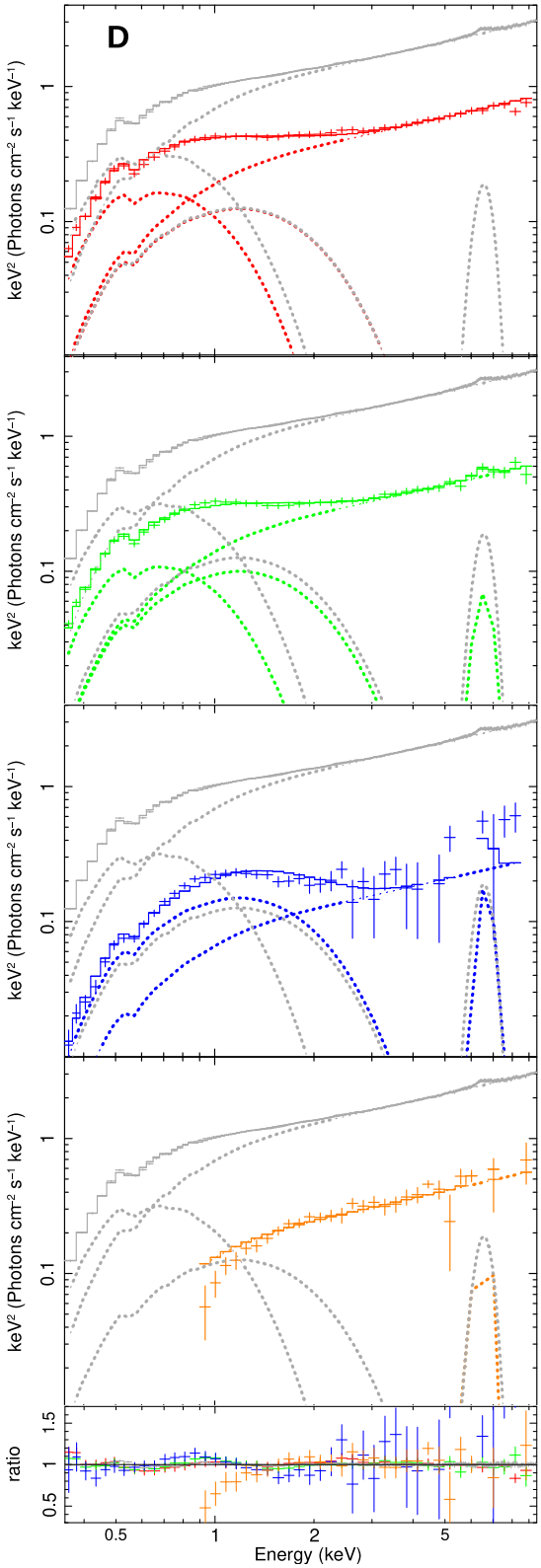

Figure 5. The best-fitting models and data of the Lorentzian spectral components (from top to bottom: L1, L2, L3, and L4), and the data-to-model ratios (bottom panel) of Model D. The colour code is the same as in Fig. 2, and the time-averaged spectrum and its residuals are shown in grey.

and ≈1/4 of them, in the inner Comptonization region (zone III). On the other hand, for L4, most of the disc photons upscattered in the outer Comptonization region (zone II) are used as seed photons for the inner Comptonization region (zone III).

In the model, emission from the inner Comptonization region dominates the bolometric X-ray flux. The outer Comptonization region is significantly softer than the inner one, i.e. $\Gamma_1 > \Gamma_2$. Overall, these results show that the structure for the accretion flow in the hard state is quite complex, with stratified Comptonization regions.

4 DISCUSSION

In our approach, spectral components derived from variability on different time-scales are thought to originate from regions of the accretion flow related to these time-scales. Generally, we expect the characteristic variability time-scale to decrease with the decreasing radial distance from the BH. However, connecting variability time-scales to radii is far from simple. Detailed spectro-timing models for Cyg X-1 and GX 339–4, in which such radii were identified, were performed by Mahmoud & Done (2018) and Mahmoud et al. (2019). In particular, the former work found evidence for the existence of discrete regions of enhanced turbulence corresponding to humps in the power spectra.

Here, we simply compare the characteristic Keplerian frequency, $\nu_{\rm K} \equiv (GM)^{1/2}/(2\pi R^{3/2})$ to the characteristic frequencies of our power spectrum, to identify the corresponding characteristic radii. Since this frequency corresponds to the fastest possible variability, it sets an upper limit on the actual emitting radii. This can be written as

$$\frac{R}{R_{\rm g}} \lesssim \frac{c^2}{(2\pi G M \nu)^{2/3}} \approx 250 \left(\frac{M}{8{\rm M}_\odot}\right)^{-2/3} \left(\frac{\nu}{1\,{\rm Hz}}\right)^{-2/3}. \quad (4)$$

For the highest peak frequency in the power spectrum, ≈2.5 Hz (L4 in Table 2), we have $R/R_{\rm g} \lesssim 140$. We can compare it with the radius based on the disc blackbody normalization, using its definition in XSPEC (stress free inner boundary condition is not included as defined in `diskbb`).We used the total normalization in the time-averaged spectrum in Model D, $(N_1 + N_2 + N_3)$. However, this might overestimate the real amount of seed photons from the disc if other sources of seed photons are present (e.g. with little overlap between the disc and the hot flow synchrotron emission might represent this additional source, e.g. Veledina, Poutanen & Vurm 2011; Poutanen, Veledina & Zdziarski 2018). Therefore, our fits allow us to put an upper limit on $R_{\rm in}$, that corresponds to the real value if the thermal photons from the disc are the only source of seed photons. We find,

$$R_{\rm in} \lesssim 5.3^{+0.5}_{-0.3} \left(\tfrac{\kappa}{1.7}\right)^2 \tfrac{d}{3\,{\rm kpc}} \left(\tfrac{\cos i}{\cos 65^\circ}\right)^{-1/2} 10^7\,{\rm cm} \approx \quad (5)$$

$$\approx 45^{+4}_{-3} \left(\frac{M}{8{\rm M}_\odot}\right)^{-1} \left(\tfrac{\kappa}{1.7}\right)^2 \tfrac{d}{3\,{\rm kpc}} \left(\tfrac{\cos i}{\cos 65^\circ}\right)^{-1/2} R_{\rm g}, \quad (6)$$

where $\kappa \approx 1.5$–1.9 is the disc blackbody colour correction (e.g. Davis et al. 2005). This satisfies the constraint (4), and shows the disc may be significantly truncated. Then, the hot accretion flow zones II and III can fit downstream of $R_{\rm in}$, showing the self-consistency of this aspect of Model D.

Our findings are valid under the assumption that that variability is only due to changes in the normalization of each spectral component. In reality the situation might be much more complex, e.g. as a consequence of spectral pivoting associated with each Comptonization zone. A more rigorous approach implies building appropriate models of the time-variable spectrum, e.g. by perturbing the parameters of

the time-averaged spectrum (Gierliński & Zdziarski 2005) or by solving the Kompaneets equation (Karpouzas et al. 2020; García et al. 2021). Nonetheless, we checked whether spectral pivoting may have a strong influence on our results, by calculating the fractional *rms* spectra of each Lorentzian (Fig. 2 – left panel). We observe that the fractional rms generally flattens out at energies $\gtrsim$3 keV. This suggests that high energy spectral components predominantly vary in normalization only, thus supporting our initial assumption. These caveats apply also when modelling disc blackbody emission. Indeed, the changes of the blackbody flux are connected to the changes of its temperature, so assuming only variations of normalization results in overestimating the real temperature in fits of *rms* spectra (van Paradijs & Lewin 1986).

The question our research directly addressed was the structure of the accretion flow. Detailed modelling of Comptonization in the accretion flow appears not unique. Clearly, this flow does not consist of a single uniform plasma cloud, as shown by the failure of our Model A to describe the *rms* spectra. Our Model B (Table 3) shows that a significant improvement is achieved when allowing the slopes of the *rms* spectra to differ between the components, in agreement with what is seen in Fig. 2. This can be due to the parameters of the Comptonizing cloud, namely the optical depth and electron temperature, evolving along the accretion flow, and forming distinct zones.

Our Model C points to the average energy of the seed photons for Comptonization to vary between the *rms* spectra of each Lorentzian component. The inner temperature for L1 is weakly constrained, but consistent with being the same as that of the directly observed disc blackbody; those for L2 and L3 are somewhat larger, and the seed photons for L4 have significantly higher temperature, $kT_{\rm in} \approx 0.5$–1.2 keV. This may suggest that photons upscattered in one zone serve as the seed photons for the subsequent zones (as in the models of Axelsson & Done 2018 and Mahmoud & Done 2018). Alternatively, there could be cold clumps formed by some instabilities in the inner parts of the hot flow (e.g. Wu et al. 2016; see Poutanen et al. 2018 for consequences for radiative cooling). Still, even this model leaves significant residuals after the fit, with the actual spectrum of L4 having a sharper low-energy cutoff than that in the fitted model, see Fig. 3. Disc blackbody emission is significant in the *rms* spectra of the two lower frequency Lorentzians (L1 and L2), meaning that the disc strongly varies on long time-scales ($\nu_{\rm max} \lesssim$1 Hz, Table 3, Models B and C). On the other hand, the direct disc blackbody emission is not observed in the *rms* spectra of L3 and L4, meaning that the disc does not contribute significantly to the high-frequency variability components ($\nu_{\rm max} >$1Hz). At the same time, Comptonization emission varies on all time-scales, but its fastest-varying component, L4, is also the hardest, with no detectable variability at energies $\lesssim$1 keV (Fig. 2, Table 3). However, the spectral evolution over Lorentzians with increasing peak frequency is relatively complex, with L1 and L2 having very similar shapes and L3 being the softest in the $\approx$1–2 keV range and then hardening. This appears to be a more complex behaviour than that found for Cyg X-1 (Axelsson & Done 2018; Mahmoud & Done 2018). However, those papers based their analysis on the data at photon energies at $\geq$3 keV, where indeed our *rms* spectra show more uniformity (Fig. 2).

In Model D, we explored an alternative scenario in which each of the *rms* spectra is fitted by two Comptonization zones. Following results from fits of Models B and C, we ascribe the disc blackbody emission to the outer disc zone I (Fig. 4). The electrons in the outer Comptonization zone (zone II in Fig. 4) upscatter the disc blackbody photons, while those in the inner Comptonization zone (zone III in Fig. 4) upscatter the photons created in the outer Comptonization zone. This follows the hints for such complexity from the results of the fitting of the previous Models B and C.

Model D can simultaneously describe the time-averaged and *rms* spectra quite well. The fractional variability of the directly observed disc blackbody emission is as high as $\gtrsim$60 per cent (Model D; Table 2). This value is consistent with estimates for GX 339-4 in the hard state (De Marco et al. 2015). The variability of the disc blackbody photons is almost entirely in the low-frequency components L1 and L2. Still, the components L1 and L2 also show variability in the Comptonization zones. The spectrum L3 has significant contributions from both the outer and inner Comptonization zones but none from the disc, while L4 is formed almost exclusively in the inner zone.

The behaviour described above strongly supports the picture of propagating fluctuations, with the dominant variability moving from the outer disc through the outer hot flow to the inner one while the dominant characteristic variability frequency increases. Our results agree with the detection of hard X-ray lags in this source (Kara et al. 2019; De Marco et al. 2021). Indeed, such lags are commonly ascribed to propagation of mass accretion rate fluctuations in the accretion flow (Lyubarskii 1997). In order to produce lags, the perturbations have to propagate through a spectrally inhomogeneous region, with the hardest spectrum produced at the smallest radii (Kotov et al. 2001), as we find from our fits.

Still, this model has a number of caveats. It shows significant residuals at the low-energy cutoff of the spectrum L4, similarly as in the previous models. Such residuals suggest that the emission from zone III may be underestimated in the spectrum of L1, L2, and L3. This would ultimately lead to overestimate emission from zone II, resulting in this component exceeding the corresponding time average contribution. A solution for this would be to include further stratification of the hot flow, but our data are statistically not sufficient for such complex models. Moreover, since we assumed that there are only two Comptonization zones, the *rms* spectrum of each Lorentzian is modelled assuming the same slope for each Comptonization zone, and only the relative normalizations vary. While this provides a good fit to the data at $\lesssim$10 keV, it fails to describe the hardening observed at $\gtrsim$10 keV in this source (Zdziarski et al. 2021b). Such hardenings are also observed in other BH XRBs, e.g. Cyg X-1 (Nowak et al. 2011) or XTE J1752–223 (Zdziarski et al. 2021a). We note that, if the variations of spectral shape are only in normalization then the outer Comptonization zone has a very low electron temperature, $kT_{\rm e} \approx 0.34^{+0.04}_{-0.03}$ keV. This means that this is likely to be a warm corona above the disc rather than a hot flow. The implied Thomson optical depth is $\tau_{\rm T} \approx 48$ (as follows for the used spectral model from equation (14) of Zdziarski et al. 2020), which is quite unrealistic. Looking at the spectral components in Fig. 4, we see that this component resembles quite well another blackbody component rather than a genuine Comptonization zone. While this points to a deficiency of our model, more model complexity could not be reasonably constrained by our data. Similar spectral decomposition was found for another X-ray binary Cyg X-1 (Di Salvo et al. 2001; Frontera et al. 2001; Makishima et al. 2008; Nowak et al. 2011; Yamada et al. 2013; Basak et al. 2017)

5 CONCLUSIONS

We studied the spectral structure of the Comptonization region in the hard state of MAXI J1820+070 using *NICER*data. To this aim we extracted the energy spectra of each Lorentzian describing the humped shape of the PSD of the source. The distribution over timescales of these variability components is thought to resemble

the spatial distribution of energy dissipation zones in the hot flow, with the highest frequency Lorentzians corresponding to variability produced in the innermost regions.

The main result of our analysis is the evidence of a spectral stratification of the hot flow, which can be clearly appreciated in a model-independent way by simply looking at the significant changes in the *rms* spectra of the different Lorentzians (Fig. 2). Going from the lowest to the highest frequency Lorentzian (L1 and L4 respectively) a net hardening of the hard X-ray spectrum is observed.

We modelled the *rms* spectra of each Lorentzian in order to characterize the spectral structure of the source. Our simple Models B and C (Section 3.3 and Table 3) show that the slope of the Comptonization component significantly changes among Lorentzians. This means that the physical properties of the Comptonization region change as a function of radius. In particular, we found that the highest frequency Lorentzian L4 has a significantly harder spectrum than L3 (Table 3). The two lowest frequency Lorentzians L1 and L2 do not show significant changes of spectral index and have a softer/harder spectrum than L4/L3 (Table 3). Also, our Model C provides evidence for hotter seed photons ($kT_{\rm in} = 0.85^{+0.41}_{-0.29}$ keV) in the fastest variability component L4 compared to the other components ($kT_{\rm in} \sim 0.3$ keV).

Consistent with the above findings, we then describe the hot flow in a self-consistent way by two Comptonization zones and applied this model simultaneously to the *rms* spectra of each Lorentzian and the time-averaged spectrum of the source. The model (D, Table 4) comprises an outer Comptonization region fueled by thermal photons from the cool disc, and an inner Comptonization region fueled by a fraction of the upscattered photons from the outer Comptonization region. We find that this model can describe data spectra well.

ACKNOWLEDGEMENTS

The authors acknowledge Mariano Mendez and the referee, Chris Done, for helpful discussions and suggestions which significantly improved the paper. We have benefited from discussions during Team Meetings of the International Space Science Institute in Bern, whose support we acknowledge. We also acknowledge support from the Polish National Science Centre under grants 2015/18/A/ST9/00746 and 2019/35/B/ST9/03944, the European Union's Horizon 2020 Framework Programme under the Marie Skłodowska-Curie grant agreement No. 798726, and from Ramón y Cajal Fellowship RYC2018-025950-I (https://euraxess.ec.europa.eu/jobs/funding/ramón-y-cajal-programme-ryc-2019-grants-postdoctoral-work-contracts).

DATA AVAILABILITY

The data underlying this article are available in HEASARC, at https://heasarc.gsfc.nasa.gov/docs/archive.html.

REFERENCES

Arévalo P., Uttley P., 2006, MNRAS, 367, 801
Arnaud K. A., 1996, in Jacoby G. H., Barnes J., eds, ASP Conf. Ser. Vol. 101, Astronomical Data Analysis Software and Systems V 1996, XSPEC: The First Ten Years, Astro. Soc. Pac., San Francisco, p. 12.
Atri P. et al., 2020, MNRAS, 493, L81
Axelsson M., Done C., 2018, MNRAS, 480, 751
Axelsson M., Hjalmarsdotter L., Done C., 2013, MNRAS, 431, 1987
Axelsson M., Veledina A., 2021, preprint (arXiv:2103.08795)
Bailer-Jones C. A. L., Rybizki J., Fouesneau M., Mantelet G., Andrae R., 2018, AJ, 156, 58
Bambi C. et al., 2020, preprint (arXiv:2011.04792)
Basak R., Zdziarski A. A., 2016, MNRAS, 458, 2199
Basak R., Zdziarski A. A., Parker M., Islam N., 2017, MNRAS, 472, 4220
Beer M. E., Podsiadlowski P., 2002, MNRAS, 331, 351
Begelman M. C., Armitage P. J., 2014, ApJ, 782, L18
Belloni T., Hasinger G., 1990, A&A, 227, L33
Belloni T., Homan J., Casella P., van der Klis M., Nespoli E., Lewin W. H. G., Miller J. M., Méndez M., 2005, A&A, 440, 207
Belloni T., van der Klis M., Lewin W. H. G., van Paradijs J., Dotani T., Mitsuda K., Miyamoto S., 1997, A&A, 322, 857
Cao X., 2016, ApJ, 817, 71
Coriat M., Fender R. P., Dubus G., 2012, MNRAS, 424, 1991
Davis S. W., Blaes O. M., Hubeny I., Turner N. J., 2005, ApJ, 621, 372
De Marco B., Ponti G., Muñoz-Darias T., Nandra K., 2015, MNRAS, 454, 2360
De Marco B., Zdziarski A. A., Ponti G., Migliori G., Belloni T. M., Segovia Otero A., Dziełak M., Lai E. V., 2021, preprint (arXiv:2102.07811)
Denisenko D., 2018, Astron. Telegram, 11400, 1
Di Salvo T., Done C., Życki P. T., Burderi L., Robba N. R., 2001, ApJ, 547, 1024
Done C., Diaz Trigo M., 2010, MNRAS, 407, 2287
Done C., Gierliński M., Kubota A., 2007, A&AR, 15, 1
Dunn R. J. H., Fender R. P., Körding E. G., Belloni T., Cabanac C., 2010, MNRAS, 403, 61
Dziełak M. A., Zdziarski A. A., Szanecki M., De Marco B., Niedźwiecki A., Markowitz A., 2019, MNRAS, 485, 3845
Esin A. A., McClintock J. E., Drake J. J., Garcia M. R., Haswell C. A., Hynes R. I., Muno M. P., 2001, ApJ, 555, 483
Fabian A. C. et al., 2020, MNRAS, 493, 5389
Frontera F. et al., 2001, ApJ, 546, 1027
Fürst F. et al., 2015, ApJ, 808, 122
Gandhi P., Rao A., Johnson M. A. C., Paice J. A., Maccarone T. J., 2019, MNRAS, 485, 2642
García F., Méndez M., Karpouzas K., Belloni T., Zhang L., Altamirano D., 2021, MNRAS, 501, 3173
García J. A., Steiner J. F., McClintock J. E., Remillard R. A., Grinberg V., Dauser T., 2015, ApJ, 813, 84
Gendreau K. C. et al., 2016, SPIE, 9905, 1H
Gierliński M., Zdziarski A. A., 2005, MNRAS, 363, 1349
Heil L. M., Uttley P., Klein-Wolt M., 2015, MNRAS, 448, 3339
Hjellming R. M., Rupen M. P., 1995, Nature, 375, 464
Homan J., Belloni T., 2005, Ap&SS, 300, 107
Ibragimov A., Poutanen J., Gilfanov M., Zdziarski A. A., Shrader C. R., 2005, MNRAS, 362, 1435
Kajava J. J. E., Motta S. E., Sanna A., Veledina A., Del Santo M., Segreto A., 2019, MNRAS, 488, L18
Kara E. et al., 2019, Nature, 565, 198
Karpouzas K., Méndez M., Ribeiro E. M., Altamirano D., Blaes O., García F., 2020, MNRAS, 492, 1399
Kawamuro T. et al., 2018, Astron. Telegram, 11399, 1
Kolehmainen M., Done C., Díaz Trigo M., 2014, MNRAS, 437, 316
Kotov O., Churazov E., Gilfanov M., 2001, MNRAS, 327, 799
Kylafis N. D., Belloni T. M., 2015, A&A, 574, A133
Ludlam R. M. et al., 2018, ApJ, 858, L5
Lyubarskii Y. E., 1997, MNRAS, 292, 679
Mahmoud R. D., Done C., 2018, MNRAS, 480, 4040
Mahmoud R. D., Done C., De Marco B., 2019, MNRAS, 486, 2137
Makishima K. et al., 2008, PASJ, 60, 585
Matsuoka M. et al., 2009, PASJ, 61, 999
McClintock J. E. et al., 2001, ApJ, 555, 477
Meyer F., Liu B. F., Meyer-Hofmeister E., 2000, A&A, 361, 175
Miller J. M. et al., 2008, ApJ, 679, L113
Miller J. M., Homan J., Steeghs D., Rupen M., Hunstead R. W., Wijnands R., Charles P. A., Fabian A. C., 2006, ApJ, 653, 525
Mitsuda K. et al., 1984, PASJ, 36, 741
Miyamoto S., Kitamoto S., Iga S., Negoro H., Terada K., 1992, ApJ, 391, L21
Muñoz-Darias T., Motta S., Belloni T. M., 2011, MNRAS, 410, 679
Nowak M. A. et al., 2011, ApJ, 728, 13

Nowak M. A., 2000, MNRAS, 318, 361
Parker M. L. et al., 2015, ApJ, 808, 9
Parker M. L. et al., 2016, ApJ, 821, L6
Petrucci P. O., Cabanac C., Corbel S., Koerding E., Fender R., 2014, A&A, 564, A37
Petrucci P.-O., Ferreira J., Henri G., Pelletier G., 2008, MNRAS, 385, L88
Plant D. S., Fender R. P., Ponti G., Muñoz-Darias T., Coriat M., 2015, A&A, 573, A120
Poutanen J., Veledina A., Zdziarski A. A., 2018, A&A, 614, A79
Reis R. C., Fabian A. C., Miller J. M., 2010, MNRAS, 402, 836
Reis R. C., Fabian A. C., Ross R. R., Miniutti G., Miller J. M., Reynolds C., 2008, MNRAS, 387, 1489
Revnivtsev M., Gilfanov M., Churazov E., 1999, A&A, 347, L23
Shidatsu M., Nakahira S., Murata K. L., Adachi R., Kawai N., Ueda Y., Negoro H., 2019, ApJ, 874, 183
Stevens A. L. et al., 2018, ApJ, 865, L15
Sunyaev R. A., Titarchuk L. G., 1980, A&A, 500, 167
Tomsick J. A. et al., 2008, ApJ, 680, 593
Tomsick J. A. et al., 2018, ApJ, 855, 3
Torres M. A. P., Casares J., Jiménez-Ibarra F., Álvarez-Hernández A., Muñoz-Darias T., Padilla M. A., Jonker P. G., Heida M., 2020, ApJ, 893, L37
Torres M. A. P., Casares J., Jiménez-Ibarra F., Muñoz-Darias T., Armas Padilla M., Jonker P. G., Heida M., 2019, ApJ, 882, L21
Tucker M. A. et al., 2018, ApJ, 867, L9
Uttley P. et al., 2018, Astron. Telegram, 11423, 1
van Paradijs J., Lewin H. G., 1986, A&A, 157, L10
Vaughan S., Edelson R., Warwick R. S., Uttley P., 2003, MNRAS, 345, 1271
Veledina A., Poutanen J., Vurm I., 2011, ApJ, 737, L17
Walton D. J. et al., 2016, ApJ, 826, 87
Walton D. J. et al., 2017, ApJ, 839, 110
Wang-Ji J. et al., 2018, ApJ, 855, 61
Wilms J., Allen A., McCray R., 2000, ApJ, 542, 914
Wu M.-C., Xie F.-G., Yuan Y.-F., Gan Z., 2016, MNRAS, 459, 1543
Xu Y., Harrison F. A., Tomsick J. A., Hare J., Fabian A. C., Walton D. J., 2020, ApJ, 893, 42
Yamada S., Makishima K., Done C., Torii S., Noda H., Sakurai S., 2013, PASJ, 65, 80
Zdziarski A. A., De Marco B., 2020, ApJ, 896, L36
Zdziarski A. A., De Marco B., Szanecki M., Niedźwiecki A., Markowitz A., 2021a, ApJ, 906, 69
Zdziarski A. A., Dziełak M. A., De Marco B., Szanecki M., Niedźwiecki A., 2021b, ApJ, 909, L9
Zdziarski A. A., Szanecki M., Poutanen J., Gierliński M., Biernacki P., 2020, MNRAS, 492, 5234

This paper has been typeset from a TEX/LATEX file prepared by the author.